Reconfigurable Dielectric Resonator Antennas

Jason Desjardins

A thesis submitted to the
Faculty of Graduate and Postdoctoral Studies
in partial fulfillment of the requirements for the degree of

Master of Applied Science
in Electrical and Computer Engineering

Ottawa-Carleton Institute for Electrical and Computer Engineering
School of Information Technology and Engineering
University of Ottawa

Abstract

With the increasing demand for high performance communication networks and the proliferation of mobile devices, significant advances in antenna design are essential. In recent years the rising demands of the mobile wireless communication industry have forced antennas to have increased performance while being limited to an ever decreasing footprint. Such design constraints have forced antenna designers to consider frequency agile antennas so that their behavior can adapt with changing system requirements or environmental conditions. Frequency agile antennas used for mobile handset applications must also be inexpensive, robust, and make use of electronic switching with reasonable DC power consumption.

Previous works have addressed a number of these requirements but relatively little work has been performed on frequency agile dielectric resonator antennas (DRAs). The objective of this thesis is to investigate the use of DRAs for frequency reconfigurability. DRAs are an attractive option due to their compactness, very low losses leading to high radiation efficiencies (better than 95%) and fairly wide bandwidths compared to alternatives. DRA's are also well suited for mobile communications since they can be placed on a ground plane and are by nature low gain antennas whose radiation patterns typically resemble those of short electric or magnetic dipoles.

One way to electronically reconfigure a DRA, in the sense of altering the frequency band over which the input reflection coefficient of the antenna is below some threshold, is to partially load one face of the DRA with a conducting surface. By altering the way in which this surface connects to the groundplane on which the DRA is mounted, the DRA can be reconfigured due to changes in its mode structure. This connection was first made using several conducting tabs which resulted in a tuning range of 69% while having poor cross polarization performance. In order to address the poor cross polarization performance a second conducting surface was placed on the opposing DRA wall. This technique significantly reduced the cross polarization levels while obtaining a tuning range of 83%. The dual-wall conductively loaded DRA was then extended to include a full electronic implementation using PIN diodes and varactor diodes in order to achieve discrete and continuous tuning respectively. The two techniques both achieved discrete tuning ranges of 95% while the varactor implementation also had a continuous tuning range of 59% while both maintaining an acceptable cross polarization level.

Acknowledgements

I am very grateful for the enthusiastic guidance and support of my supervisors Dr. Derek McNamara and Dr. Aldo Petosa throughout the course of this study. I have enjoyed working with them and their insights have been invaluable.

I would like to thank Mr. Michel Cuhaci and the Communications Research Centre (CRC) for the use of the CRC fabrication & measurement facilities, and partial funding of this work. Thanks to Mr. Soulideth Thirakoune for his help with the measurement process. And finally, I am thankful to my family, friends and fellow colleagues for their words of encouragement and support over the last two years.

Publications

J.Desjardins, D.A.McNamara, S.Thirakoune & A.Petosa, "A Comparison of the Electromagnetic Modelling of Metal-Loaded Dielectric Resonator Antennas Using Different Computational Techniques", Proc. *14th Int. Symposium on Antenna Technology & Applied Electromagnetics (ANTEM'2010)*, Ottawa, July 2010.

J.Desjardins, D.A.McNamara & A.Petosa, "A Reconfigurable Dielectric Resonator Antenna (DRA) with Switched Conductive Loading", *URSI Radio Science Meeting Digest*, Toronto, Canada, July 2010.

Table of Contents

List of Figures

List of Tables

Chapter 1 - Introduction

1.1 Introductory Remarks

With the increasing demand for high performance communication networks and the proliferation of mobile devices, significant advances in antenna design are essential in order to meet tomorrow's requirements. In recent years the rising demands of the wireless communication industry have forced antennas to have increased performance while being limited to an ever decreasing footprint. Such design constraints have forced antenna designers to consider reconfigurable antennas so that their behavior can adapt with changing system requirements or environmental conditions, thereby ameliorating the device performance while providing additional functionality to the system [1]. Additionally, such antennas are essential if software defined radio or cognitive radio are to be realized [2]. Such architectures would place further demands on the antenna while at the same time necessitating that the antenna be frequency agile. Therefore, electrically small antennas with narrow bandwidths can be used to cover large frequency ranges by making use of frequency reconfigurability [3]. This would result in a paradigm shift in mobile communications since rather than having multiple antennas that cover several operating bands or applications (GSM, GPS, WDCMA, m-WiMax, WiFi, WLAN, etc.) a single frequency agile antenna could be employed. This would reduce the antenna's volume while at the same time increasing performance. In order to make frequency agile antennas practical the switching must be achieved electrically by making use of active devices.

1.2 Thesis Overview

In addition to the compactness requirement, antennas used for mobile handset applications must also be inexpensive, robust, and make use of electronic switching with reasonable DC power consumption. One method to achieve compactness is to use dielectric resonator antennas (DRAs). Dielectric resonator antennas are fabricated from low-loss dielectric material. Their operating frequency is a function of the shape, dimension and permittivity of the dielectric material. These degrees of freedom allow a DRA to be designed to be quite compact. Additionally, the antennas are an attractive option due to their very low losses leading to high radiation efficiencies (better than 95%) and fairly wide bandwidths compared to alternatives. DRA's are also well suited for mobile communications since they can be placed on a ground plane and are by nature low gain antennas whose radiation patterns typically resemble those of

short electric or magnetic dipoles. Despite the aforementioned, relatively little work has been done on frequency agile DRAs. This possibility is investigated in the present thesis.

Chapter 2 provides a brief overview of the various categories of reconfigurable antennas before focusing on frequency agile antennas. A fairly complete survey of the techniques that have been described in the literature to achieve both discrete frequency tuning and continuous tuning will be presented. In addition to the review of frequency agile antennas a review of rectangular dielectric resonator antenna design is also given.

In Chapter 3 a method for achieving frequency agility using a slot coupled dielectric resonator antenna (by partially loading one or more faces of the DRA with a conductive wall) is presented, using ideal switches. First, a single-wall reconfigurable DRA is examined for various aspect ratios and a study is performed on all the possible switchable states. An optimum design is obtained and the results of simulation and measurement are discussed. A dual-wall reconfigurable DRA is then presented to address some of the shortcomings inherent in the single-wall design. Again simulation and measurement results are presented and discussed.

As the dual-wall frequency reconfigurable antenna from Chapter 3 showed excellent performance, in Chapter 4 the ideal switches are replaced with PIN diodes in order to achieve discrete tuning using electronic switching. Chapter 4 presents the selection process for the PIN diodes along with equivalent circuit models that represent the PIN diode states. The complete antenna design is then presented, along with simulation and measured data showing the frequency response and radiation pattern. In addition, the bias network design and DC power consumption are discussed.

Similar to Chapter 4, Chapter 5 again makes use of the dual-wall frequency reconfigurable antenna from Chapter 3 but rather than implementing electronic switching with PIN diodes, presents the results when varactor diode switches are implemented. The use of varactor diode switches allow continuous tuning to be achieved electronically. The selection process for the varactor diodes is outlined along with equivalent circuit models that represent the various varactor diode states. The antenna design is also presented, along with simulation and measured data showing the frequency response and radiation pattern. In addition, the bias network design and DC power consumption are again discussed.

Finally, Chapter 6 contains general conclusions drawn from the material in Chapters 3, 4 and 5 and contributions, therein described, will be summarized.

1.3 References for Chapter 1

[1] J.T. Bernhard, *Reconfigurable Antennas*. Chicago, IL: Morgan & Claypool Publishers, 2007.

[2] P.H. Rao, "Antenna Configurations for Software Defined Radio and Cognitive Radio Communication Architecture," in *Wireless Communication and Sensor Computing*, Chennai, 2010, pp. 1-4.

[3] A. Petosa, "Frequency agile antennas for wireless communications – A survey," in *Antenna Technology and Applied Electromagnetics & the American Electromagnetics Conference*, Ottawa, 2010, pp.1-4

Chapter 2 - Review

2.1 Introductory Remarks

In this chapter we will review the concept of reconfigurable antennas and define what it means to be reconfigurable. We will also briefly examine the various categories of reconfigurable antennas before focusing our interest on frequency agility. A survey of the techniques that have been used to achieve frequency agility will be presented and the core results will be outlined. In addition to the review of frequency agile antennas a brief overview of rectangular dielectric resonator antennas will be presented.

2.2 Overview of Reconfigurable Antennas

With the ever increasing demands of the modern wireless communication network and the proliferation of wireless devices and applications, novel advances in antenna design are essential. In recent years the demands of the wireless communication industry have forced antennas to be increasingly adaptable due to various constraints, such as antenna size, geometry, polarization and spatial diversity, radiation pattern, impedance bandwidth and operating frequency. Such design constraints have forced antenna designers to consider reconfigurable antennas so that their behavior can adapt with changing system requirements or environmental conditions, thereby ameliorating the device performance and eliminating some restrictions while providing additional functionality to the system [1]. Additionally, such an antenna is essential if cognitive radio or its predecessor, software defined radio, are to be realized [2]. Software defined radio is essentially a communication system that makes use of software protocols in lieu of fixed hardware components such as mixers, amplifiers, modulators/demodulators, etc. Since the traditionally fixed hardware components that handle the signal processing would now be implemented by software, the system can transmit and receive on widely different communication protocols simply by reconfiguring their software [3]. Cognitive radio shares the same fundamentals with software defined radio but extends software defined radio in that it adds environmental awareness [4]. Clearly such architectures would place further demands on the antenna while at the same time necessitating the antenna to be reconfigurable.

Since we have established the need for such an antenna the next question is to define what constitutes a reconfigurable antenna. When referring to an antenna's ability to be reconfigured

one is referring to the ability to change an individual radiating elements fundamental operating characteristics by some means. The fundamental operating characteristics that may be reconfigured include the elements operating frequency, polarization, radiation pattern, and impedance bandwidth. Therefore, a phased array is not in itself a reconfigurable antenna since the individual elements remain unchanged and the phase shift is responsible for beam steering [1]. However, if a phased array antenna included elements whose radiation pattern can be reconfigured by some means than the antenna array would be viewed as a reconfigurable antenna array under the aforementioned definition.

As previously mentioned there are three primary methods with which to reconfigure an antenna. Since we are primarily interested in frequency reconfigurable antennas we will only briefly touch on the other two methods.

Antenna Radiation Pattern Reconfigurability

As the name implies this method involves reconfiguring a radiating element's radiation pattern while not altering the other fundamental operating characteristics to a large extent. The ability to reconfigure an antenna's pattern would be invaluable within a cognitive radio architecture as the main beam can be reshaped in order to maximize efficiency and conserve battery power. Since the radiation pattern is a function of the arrangement of currents on an antenna structure it would appear as though rearranging the currents while maintaining a constant frequency response and polarization would be quite challenging [1]. However, techniques have been developed that include a hybrid high impedance surface along with multiple feeds in order to achieve a beam steerable loop capable of steering to 4 quadrants [5]. Another technique used by Sarrazin *et al.,* involves using a single feed that is used to excite a metallic cubic cavity which radiates through rectangular slots, as shown in Figure 1. The pattern reconfiguration is achieved with PIN diode switches by short-circuiting slots in their center. The designed antenna can switch between three different radiation patterns which radiate in a 4π steradian range [6]. Many other techniques exist in addition to the two listed but most make use of either symmetry in the feeding mechanism in order to maintain the frequency response or employ a coupling element so that the feed mechanism is electrically isolated from the radiating structure.

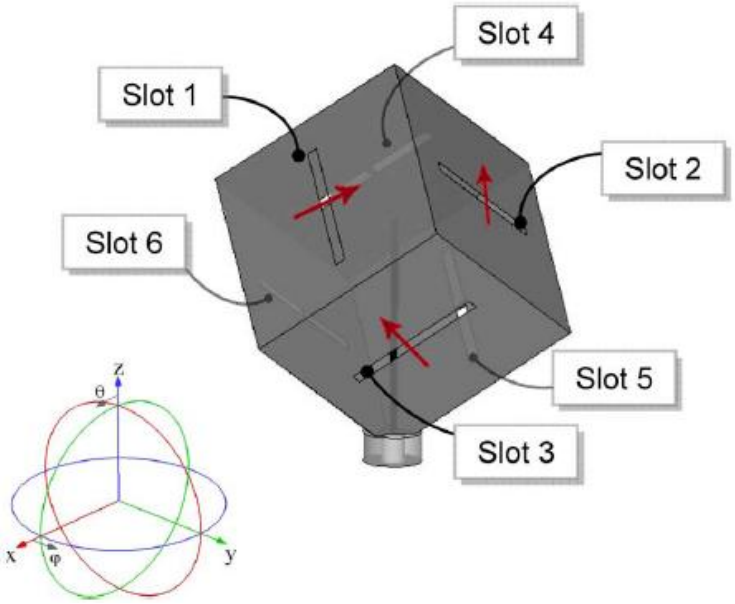

Figure 1: Pattern Reconfigurable Cubic Antenna (After [6])

Antenna Polarization Reconfigurability

The second main antenna reconfiguration technique involves the ability to alter the antenna's radiating polarization by some means. An antenna with such ability would grant some immunity from interfering signals as well as provide an additional degree of freedom to improve link quality as a form of switched antenna diversity [7]. Since the polarization of an antenna's radiated field is dependent on the current flow on the element's surface, the techniques used to alter the polarization usually involve altering the antenna structure, material properties or feed configuration so that the current flow is altered [1]. One method that makes use of varying the amplitude of orthogonal feeds to a patch antenna was demonstrated by Ferrero *et al* [8]. The antenna is fed by a quasi-lumped coupler that is able to tune the magnitude ratio between its two outputs from -30 dB to 15 dB by modifying the bias of two varactor diodes. This enabled the patch antenna to have continuous linear polarization tilt control over a range of 90 degrees. In other words, the antenna by Ferrero *et al.* operated on the principle of varying the magnitude of orthogonal currents on a microstrip patch. An example that illustrates the symmetry approach is demonstrated by Khaleghi *et al.*[9]. Their design of a single feed circular patch antenna with polarization reconfigurability made use of a circular patch printed on a thin substrate, that is supported by non conductive posts on a conducting ground plane, and excited with a capacitively coupled feed. The polarization of the circular patch is altered by switching on one of

two parasitic pins (SC1 and SC2) that connect the outer rim of the circular patch to the ground plane through the use of PIN diodes as shown in Figure 2. The switching of the parasitic shorting pins enables two orthogonal patterns with right-hand circular polarization (RHCP) and left-hand circular polarization (LHCP), while maintaining a constant frequency response and radiation pattern shape. Several additional techniques exist but the two just listed demonstrate the main techniques whereby either the feeding mechanism is altered in order to rearrange the current distribution or techniques are used to alter the current distribution while maintain symmetry.

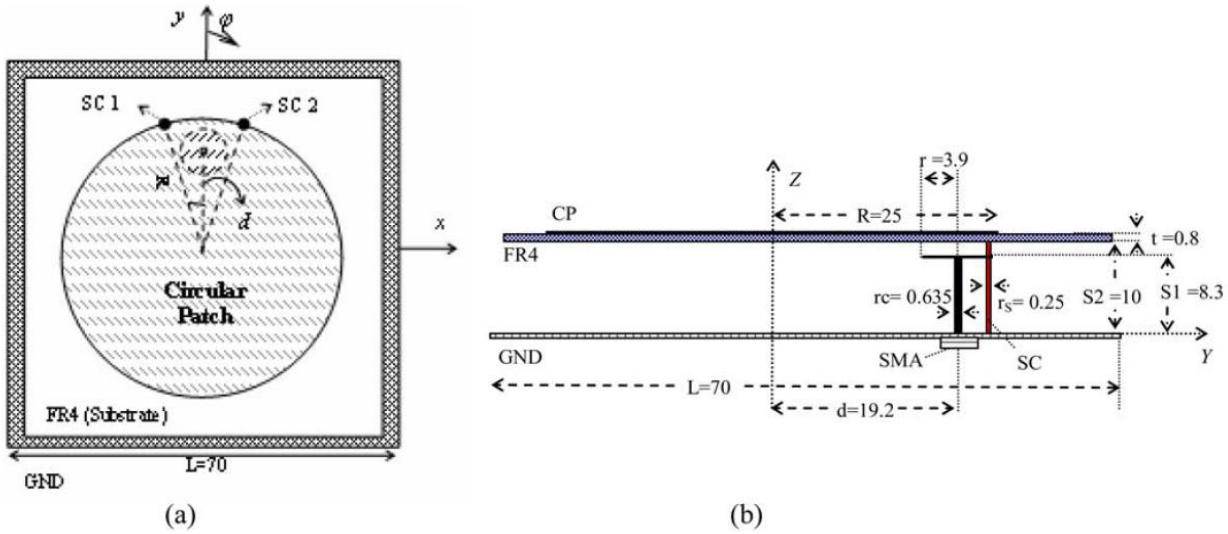

Figure 2: Polarization Reconfigurable Circular Patch Antenna a) Top View b) Side View (After [9])

2.3 Frequency Reconfigurable Antennas

The needs for frequency agile antennas are becoming ever more widespread as the rising demand for bandwidth will lead to saturation of the available frequency spectrum. As previously mentioned, novel communication architectures are being developed (software defined radio, MIMO and cognitive radio) that will alleviate the stress on the wireless networks and open new opportunities for drastic improvements in bandwidth and efficiency of the wireless network. However, in order for such architectures to be implemented, antennas capable of wideband operation are required. The austere antenna constraints on hand-held or portable devices make it difficult, if not impossible, to achieve wideband operation on such a small footprint. By designing antennas with frequency agility, small antennas with narrow instantaneous bandwidths can be tuned to operate over a larger range of frequencies, thus effectively enhancing bandwidth performance [10]. Since portable wireless communication devices

emphasize a compact antenna with omni-directional coverage, typical candidates include dipole antennas, monopole antennas, microstrip antennas, planar inverted F-antennas (PIFAs), slot antennas, chassis antennas and dielectric resonator antennas (DRAs).

Frequency agile antennas capable of tuning their frequency of operation can be classified into two distinct categories. The first category is known as discrete tuning, whereby the antenna is capable of a finite number of states or operating bands. The second category is continuous tuning, whereby the antenna is capable of achieving any frequency of operation within its tuning range. Tuning range (TR) is defined as

$$TR = \frac{2(f_{high} - f_{low})}{(f_{high} + f_{low})} \times 100\% \quad (2.3.1)$$

where f_{high} and f_{low} refer to the upper and lower frequency bounds of operation. Therefore, as one can easily deduce the tuning range of a frequency reconfigurable antenna is a very important figure of merit. Some other important figures of merit when it comes to frequency agile antennas include the antenna size, radiation efficiency, radiation pattern, cross polarization levels, power consumption to achieve reconfigurability and complexity of the bias network, among others. In the coming subsections a survey of the various mechanisms used to achieve frequency agility, along with the results achieved by the designs, will be reviewed.

2.3.1 Discrete Tuning

In order to achieve discrete tuning a frequency reconfigurable antenna usually employs some sort of switching mechanism. The switching mechanisms most commonly used to achieve discrete tuning include microelectromechanical systems (MEMS), field effect transistors (FETs) and PIN diodes. One advantage of a discretely tuned antenna over a continuous tuned antenna is the ability to design for specific bands of operation. For example an antenna by Mak *et al.* [11] was designed to operate in the GSM, DCS, PCS, UMTS, Bluetooth and 2.4 GHz LAN bands using an electrical switching mechanism for a planar inverted F-antenna (PIFA). Another benefit of discrete tuning involves larger tuning ranges on average, as sections of antennas or parasitic elements can be switched on or off, rendering them electrically absent. Additionally, switching mechanisms used in discrete tuning antennas typically require lesser DC bias levels and have lower switching device losses than their continuous tuning counterpart, although this may not always be the case.

A. MEMS Switching

In recent years MEMS switches have become a viable option for frequency agile antennas. Some notable advantages of MEMS switches are that they are very low loss, have a very wide operating frequency range, low power consumption and can handle high power. But they are currently rather expensive, and require a large DC voltage to perform switching [11]. Nonetheless, as advances are made in the fabrication process the cost of MEMS switches will surely come down. MEMS have successfully been integrated into many frequency agile antennas for the purpose of achieving specific tuning bands, such as the design by Sunan *et al.* [12]. The design involved a dual frequency reconfigurable microstrip patch antenna with integrated MEMS in order to achieve dual band operation. The ten switches are incorporated into the diagonally fed square patch (five along each side of the patch connecting to the addition) for controlling the operating frequency and a rectangular stub attached to the edge of the patch to act as the perturbation to produce the fixed circular polarization at 6.69 GHz and 7.06 GHz [12]. As shown in Figure 3 the design achieves dual band operation by either having the MEMS switched off so that the patch is of dimension L1 by L1 or switching the MEMS on so that the effective dimensions of the patch are L2 by L2 which results in a lower frequency of operation. The design achieved a tuning range of 5.38 % while requiring a DC bias of 30 volts with negligible current.

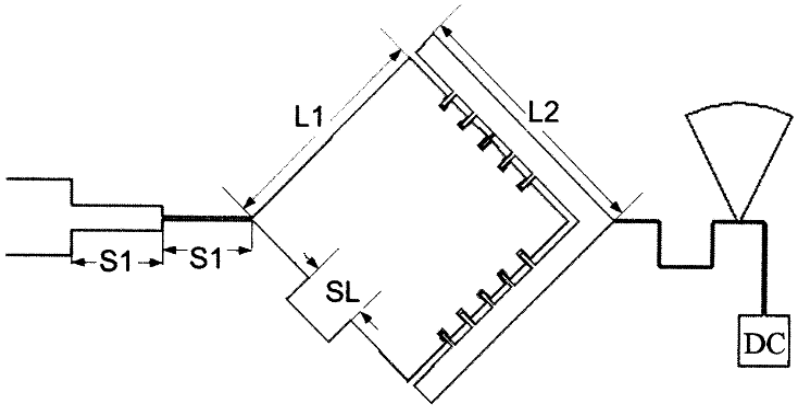

L1=9 mm, L2=10.3mm, S1=3.61mm, SL=2.4 mm

Figure 3: A Frequency-Reconfigurable Circularly Polarized Patch Antenna by Integrating MEMS Switches (Adapted from [12])

A second design that makes use of MEMS switches to achieve discrete tuning ranges involves an innovative nested patch antenna developed to cover the various GSM, GPS, DCS, PCS, Bluetooth and WLAN services [13]. The design by Chunna *et al.*[13] was achieved using U-slots for multi-band operation so that a set of appropriately chosen nested patches each operate at specific frequencies. Even and odd structure symmetry was then applied in order to reduce the size by 50%, as shown in Figure 4.

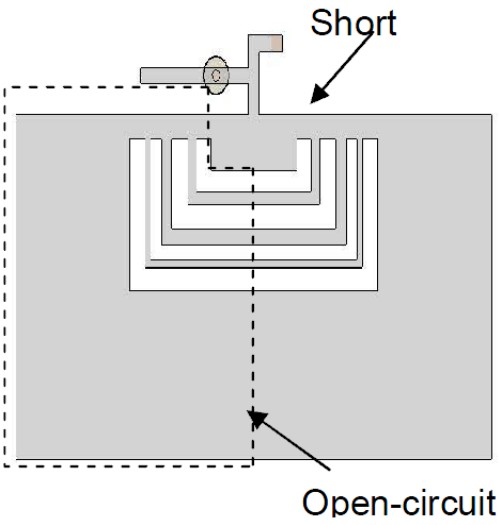

Figure 4: Design Methodology for Mini-Nested Patch Antenna Using MEMS (After [13])

Since the nested patches are conductively coupled through the narrow microstrip sections along the top of the antenna, MEMS switches were integrated in order to provide the reconfigurability feature as shown in Figure 5. The final design was able to achieve a tuning range of 141% with a gain of over 4 dBi while operating in the GSM, GPS, DCS, PCS, Bluetooth, WLAN 2.4GHz, and WLAN 5.2GHz frequency bands, as shown in Figure 6. While many other frequency agile antennas exist which employ MEMS switches as the switching component the aforementioned design achieved the greatest performance in terms of tuning range, antenna footprint (size), gain and radiation pattern, although details on power consumption, efficiency or cross-polarization levels were not given in [13]. MEMS have also been used for PIFA antennas [14], capacitive coupling element antennas [15], printed fractal antennas [16, 17], slot antennas [18-20], printed dipoles [21] and microstrip antennas [22].

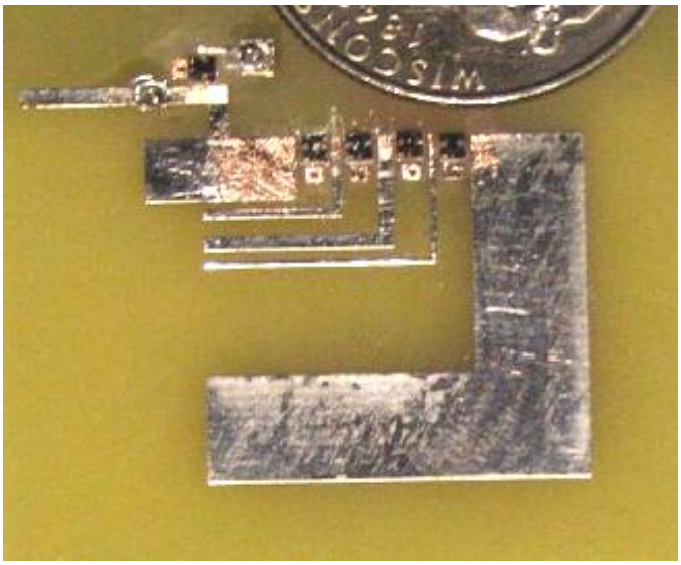

Figure 5: Mini-Nested Patch Antenna with Integrated MEMS Switches (After [13])

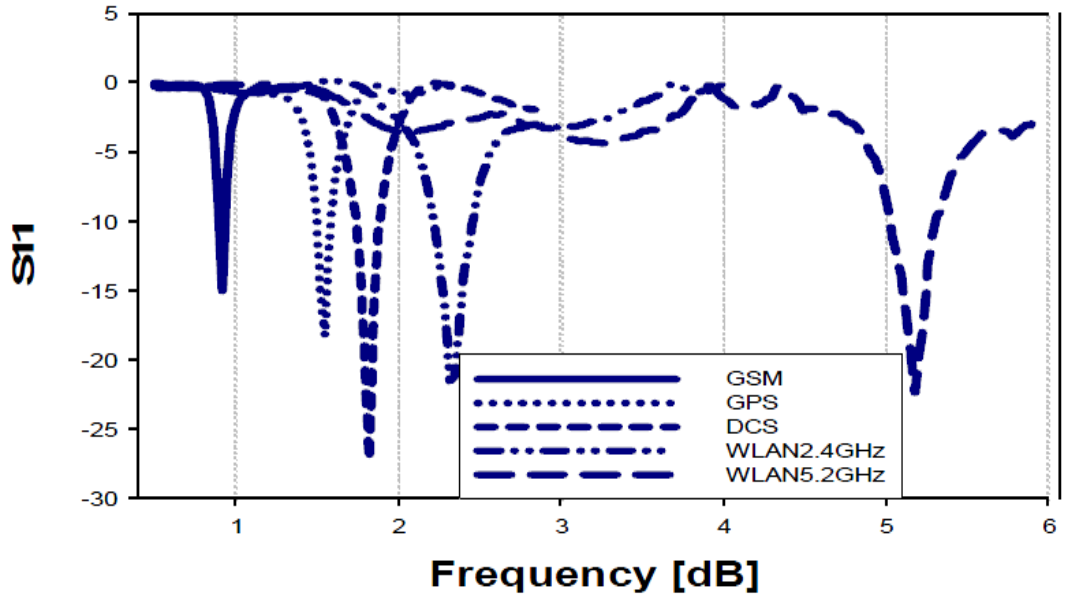

Figure 6: Frequency Response for Mini-Nested Patch Antenna with Integrated MEMS Switches (After [13])

B. FET Switching

Field effect transistors (FETs) have also been used to achieve frequency reconfigurable antennas. FETs can be an attractive switching element as it is a voltage-controlled device which saves on power consumption while at the same time being very low cost. Although FETs typically involve a more complex bias network, and result in lower antenna radiating efficiency, they are still viable options in some cases with tuning ranges of 10 % being achieved using a slot

antenna with a layered structure loaded with FET's [23]. Mak *et al.* [11] incorporated a GaAS FET to operate in the GSM, DCS, PCS, UMTS, Bluetooth and 2.4 GHz LAN bands with a PIFA resulting in a tuning range of 84%. However, it was found that the GaAS FET had a substantial reactive loading effect resulting in a diminished tuning range as well as a reduction in radiation efficiency when compared to a MEMS switch and PIN diode [11]. GaAS FETs were also integrated into a frequency agile PIFA [24] that obtained a contiguous tuning range of 12.7%.

C. PIN Diode Switching

These are perhaps the most widely used electronic switch employed to achieve frequency agility due to their low cost, very low loss, good isolation and simplicity when modeling with lumped elements [25]. In [11] Mak *et al.* found that after experimentation with MEMS switches, GaAS FETs and PIN diodes, the PIN diode switched antenna had the greatest antenna radiation efficiency and was most similar to an ideal switch for their application. The PIN diode has also become an attractive element since it comes in many package sizes (which increase its functionality) and has a relatively simple DC bias network. However, since the PIN diode is a current device it may consume more power than MEMS and FETs. Nonetheless some of the highest tuning ranges and performance levels have been achieved with PIN diodes. A compact tunable rectangular patch antenna with slots etched in the patch in order to reduce its size and increase the tuning range was developed by Sheta *et al* [26]. It uses PIN diodes in order to achieve reconfigurability. As shown in Figure 7, the design places thin posts at selected positions near the edge and each can be short circuited to the ground plane through an electronically controlled PIN diode. Frequency agility is achieved by the appropriate selection of the posts to be shorted. The antenna is capable of tuning in operating bands from 620 to 1150 MHz, corresponding to a tuning range of 60%.

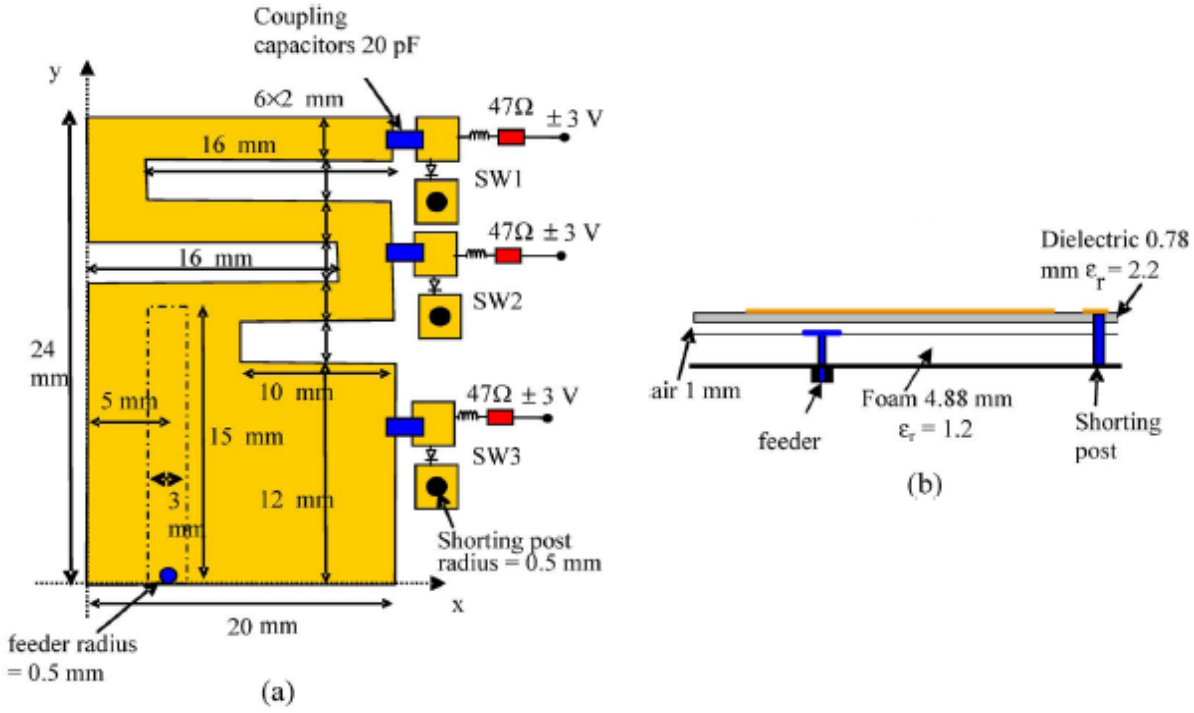

Figure 7: Frequency Agile Compact Tunable Rectangular Patch Antenna a) Top View b) Side View (After [26])

Another example designed by Laheurte *et al.*[27] involves a switchable CPW-fed slot antenna with eight PIN diodes integrated along the dipole arms used to obtain frequency reconfigurability, as shown in Figure 8. By switching on or off different combinations of diodes the effective length of the dipole is altered, thus changing the resonant frequency.

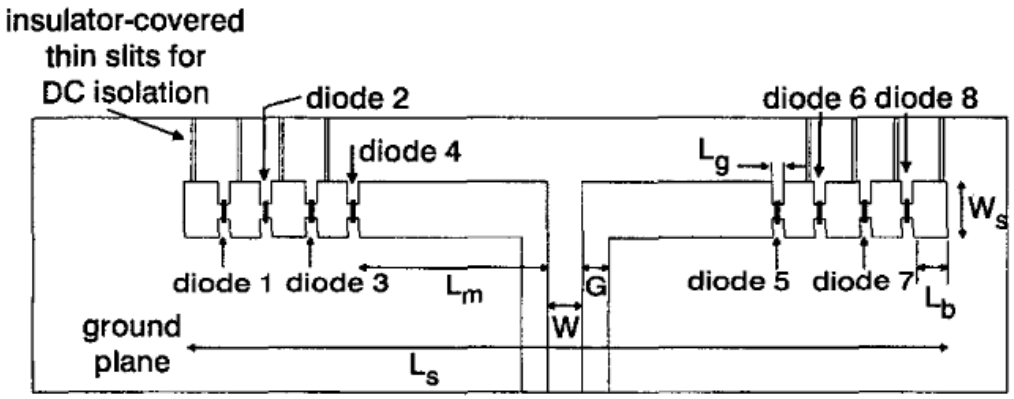

$L_g = 500\,\mu m$, $W_s = 3\,mm$, $L_s = 64.7\,mm$, $L_m = 10\,mm$, $L_b = 4.75\,mm$, $W = 2.7\,mm$, $G = 150\,\mu m$
Ground plane dimensions $170 \times 120\,mm$

Figure 8: Switchable CPW-Fed Slot Antenna Geometry (After [27])

Since four sets of diodes are used, five unique operating bands were obtained that are dependent on the relative length of the dipole arms. A tuning range of 92% was achieved, with very low cross polarization levels over the tuning range. PIN diodes have also been integrated into PIFAs [28, 29], microstrip antennas [30], printed dipoles [31], and various shaped slot antennas [32 -35].

2.3.2 Continuous Tuning

In order to achieve continuous tuning a frequency reconfigurable antenna usually employs structural changes, material changes or reactive loading. For frequency agility by means of altering material or structural properties, one likely uses ferrite materials, piezoelectrics or even mechanical actuators. Although material changes may provide large continuous tuning ranges, they often lead to very high DC power consumptions and can be impractical to implement. The switching mechanism most commonly used to achieve reactive loading is a varactor diode. Since varactors are voltage devices they have very low power consumption but sometimes requiring relatively high DC voltages.

A. Structural/Mechanical Changes

Although structural changes can deliver large continuous frequency shifts, they can often be impractical to implement or require complex bias networks. Such is the case for the

reconfigurable dielectric resonator antenna designed by Huff *et al.*[36]. Their design dispersed a colloidal barium strontium titanate in hydrotreated naphthenic oil into cylindrical polycarbonate tubing, as shown in Figure 9. By varying the vertical displacement of the liquid continuous frequency tuning was achieved from 2.5 GHz to 4.5 GHz corresponding to a tuning range of 57%. Although the design achieved a relatively large continuous tuning range the feasibility of implementing such a design and incorporating a mechanism to add, remove and store the fluid render it ineffective.

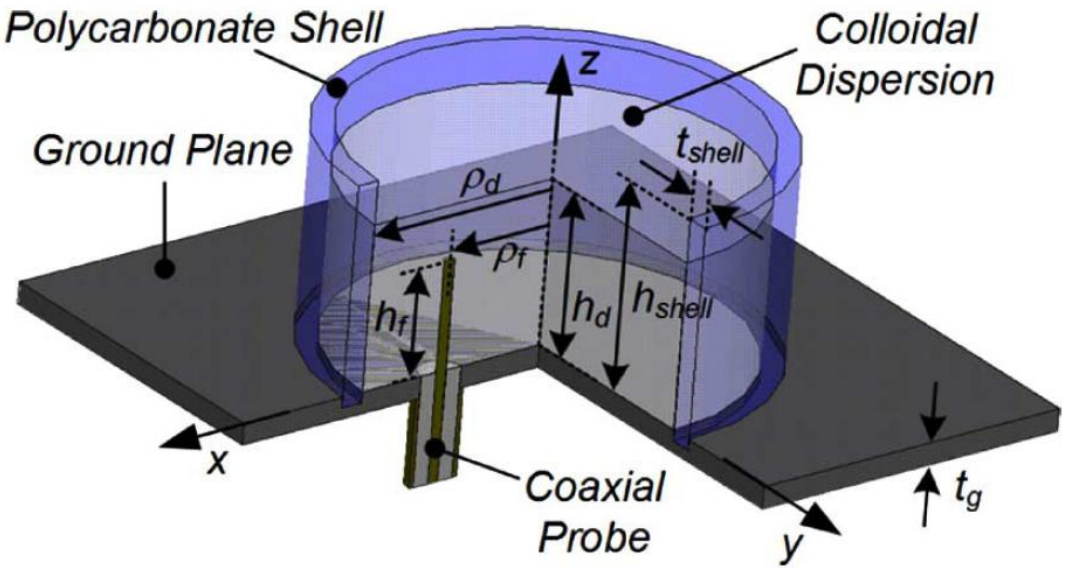

Figure 9: Diagram of the Coaxially Fed DRA using a Variable-Height Colloidal Dispersion (After [36])

A piezoelectric actuator system has also been used to vary the spacing between a microstrip antenna and parasitic radiator [37] which achieved a tuning range of 9% while still requiring considerable complexity. While structural changes may seem like an attractive option due to their inherent low losses, the slow switching time, limited tuning ranges and large DC bias power levels render them as poor candidates for mobile communications.

B. Material Changes

Since an element's frequency of operation is dependent on its material properties, having the ability to vary a material's permittivity or permeability will result in frequency of operation shifts. Since ferrite, ferroelectric and liquid crystal material properties can be altered by the presence of an electric or magnetic field they make good candidates for frequency agile

antennas. One of the first examples of using ferrite materials to achieve a continuous tuning range was presented in 1988 by Pozar *et al.*[38]. The design achieved a continuous tuning range of 40% by printing a microstrip antenna on a ferrite substrate and then subjecting it to a varying magnetic bias field perpendicular to the resonant dimension of the patch. Another example of a microstrip patch on a ferrite substrate [39], shown in Figure 10, achieved a tuning range of 133 % by varying the DC magnetic bias field. Although a continuous tuning range of 133 % was reported no analysis on the radiated pattern was performed and the return loss was not reported.

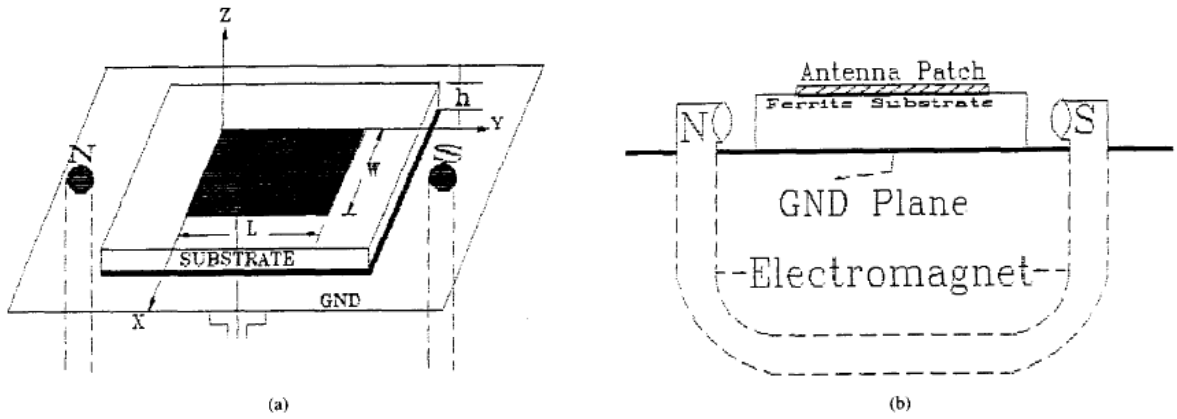

Figure 10: Frequency Agile Microstrip Patch Antenna on Ferrite Substrate a) Top View, b) Side View (After [39])

Dielectric resonator antennas fabricated from ferrite materials have also been used to achieve frequency reconfigurability [40] with a tuning range of 19% being reported. Ferroelectric materials have also been used in recent years; however they suffer from high losses at microwave frequencies and require large bias voltages. It's clear that although large tuning ranges can be obtained via material changes, the disadvantages far outweigh the benefits as they typically require high bias levels and standard ferroelectric materials have high conductivities relative to other substrates that degrade the efficiency of the antenna [1].

C. Variable Reactive Loading

In order to achieve variable reactive loading, a varactor diode is most commonly utilized. Since a varactor's capacitance can take on a continuous range of values by varying a DC bias voltage, they make excellent tuning components. One example of a continuously tuned frequency agile antenna is presented in [41]. The design consists of a driven dipole element with

a varactor in each of two arms, a director with an additional varactor, and a truncated ground plane as shown in Figure 11. The effective electrical length of the director element and that of the driven arms are adjusted together by changing the biasing voltages from 0 to 17 volts. A 35% continuously tuned bandwidth from 1.80 to 2.45 GHz was achieved.

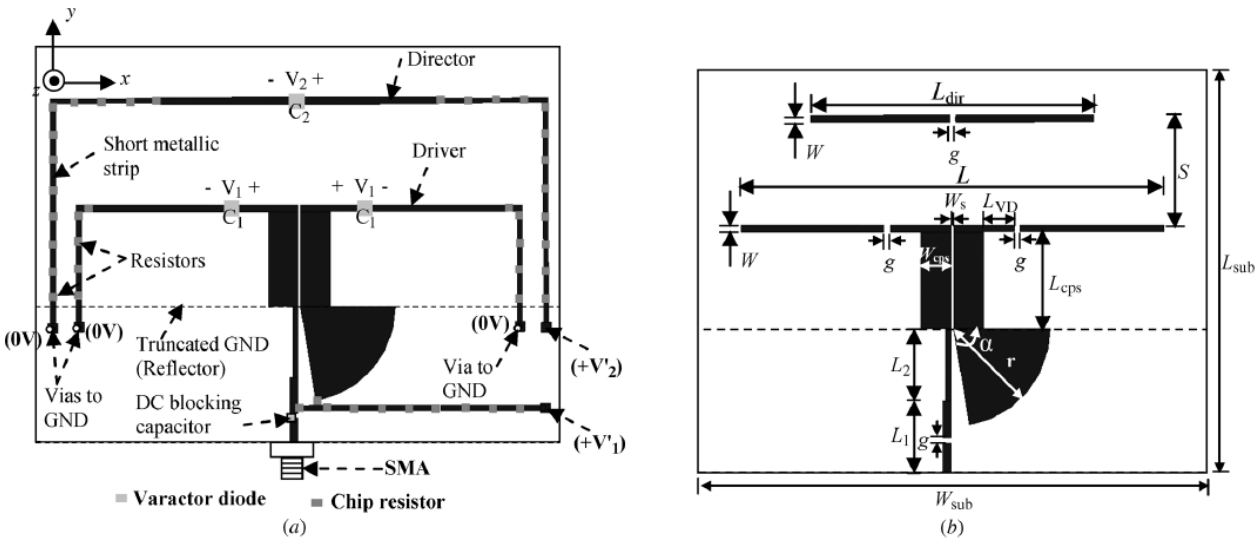

$L = 83.5, W = 1.5, L_{dir} = 56, S = 21.5, W_{cps} = 6, L_{cps} = 19, W_s = 0.5, L_{VD} = 6, r = 19, L_1 = 14, L_2 = 14, g = 1, W_{sub} = 102, L_{sub} = 87$ (all dimensions are in millimeters), and $\alpha = 76°$.

Figure 11: Frequency-Reconfigurable Quasi-Yagi Dipole Antenna a) Antenna Design Layout b) Antenna Without Biasing Lines (After [41])

Another example developed by Song *et al.*[42] incorporates two metal elements which are capacitively coupled to excite resonant modes within a handset chassis. The antenna elements are located in close proximity to each other, and are connected via independent ports. The frequency tuning is achieved via a matching circuit that incorporates a pair of varactors. The antenna is able to continuously tune from 800 MHz to 2900 MHz corresponding to a tuning range of 115%. However, the design has yet to be fabricated as only simulation results are quoted. Varactors have also been implemented in monopole antennas [43], PIFAs [44-46], slot dipoles [47], slot rings [48], and printed bowties [49]. More recently varactors have been combined with PIN diodes in order to achieve very large continuous tuning ranges. A design by Hui *et al.*[50] achieved a continuous tuning range of 112% by integrating a PIN diode and varactor diode into a slot. By switching the PIN diode placed at the open end of the slot, the slot antenna can resonate as a standard slot (when the switch is on) or a half slot (when the switch is off), as shown in Figure 12. Continuous tuning over a wide frequency range in those two modes

can be achieved by adjusting the reverse bias of the varactor diode loaded in the slot. Through good design, the tuning bands of the two modes are stitched together to form a very wide tuning range (0.42 GHz to 1.48 GHz) [50]. This technique was also used by Jong-Hyuk *et al.*[51] in their design of a reconfigurable PIFA antenna for achieving specific bands of operation relevant to the handset industry. It is clear that varactor diodes are a very adaptable component for achieving frequency agility. Although the varactors incur larger RF losses than PIN diodes they enjoy the benefit of being voltage controlled devices which do not require current to operate, although they may require DC bias voltages of over 30 volts.

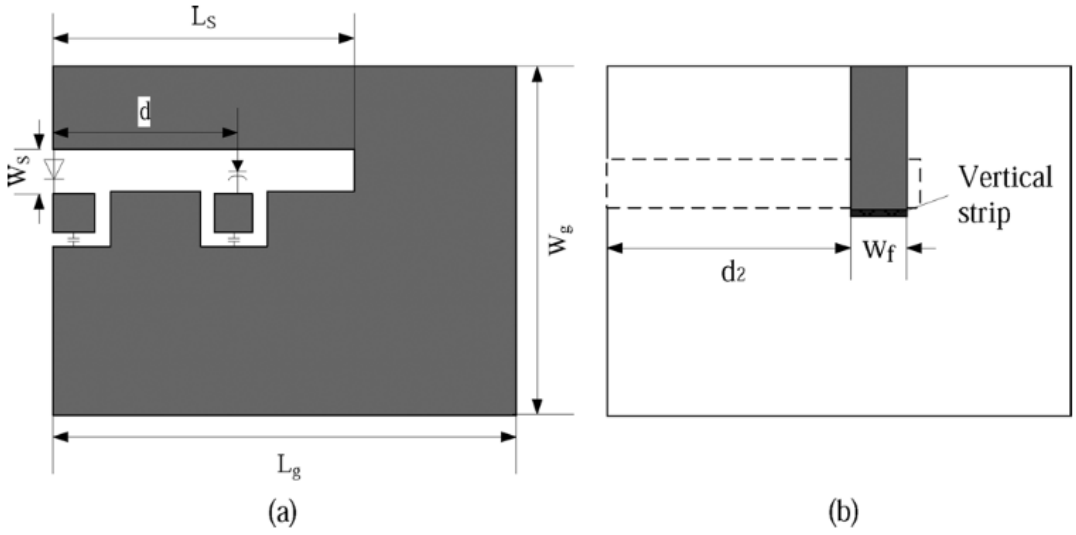

The dimensions are: $L_g = 35$ mm, $W_g = 20$ mm, $L_S = 25$ mm, $W_s = 1.5$ mm, $d = 15$ mm, $d_2 = 21.1$ mm, $W_f = 3.8$ mm.

Figure 12: Antenna Geometry of a Compact Reconfigurable Slot Antenna with a Very Wide Tuning Range a) Front, b) Back (After [50])

2.3.3 Summary

It is clear from the previous sections that many novel techniques have been presented in order to achieve frequency reconfigurability. The advantages and disadvantages of each approach were outlined along with some notable examples that represent the fundamentals of each method along with the highest performance levels to the author's knowledge. A recent publication by Petosa [10] surveyed many of the techniques mentioned in the previous sections and highlighted the key attributes of each technique, as is done similarly in Table 1.

Table 1: Summary of Frequency Reconfigurable Techniques

Frequency Agility Technique	Examples	Tuning Ability and Tuning Range	Attributes
Electronic Switches	- PIN Diodes - MEMS - FETs	Discrete Tuning • MEMS – 141 % • FETs – 84 % • PIN – 92 %	- Low loss - Low bias levels - Easily integrated
Structural/ Mechanical Changes	- Colloidal Dispersions - Mechanical and Piezoelectric Actuators	Continuous Tuning • Up to 57 %	- Low Loss - Slow response Time - High actuation voltages
Material Changes	- Ferrites - Ferroelectrics - Liquid Crystals	Continuous tuning • Ferrites – 133 %	- High loss - Temperature sensitive - Large bias levels
Variable Reactive Loading	- Varactors	Continuous tuning • Varactor - 63 % • Varactor – 115 % (Sim) • Varactor & PIN diode – 112 %	- Some losses - Low/medium bias levels - Easily integrated

2.4 Overview of Rectangular Dielectric Resonator Antennas

A dielectric resonator antenna (DRA) is a antenna, fabricated from low-loss dielectric material. Its resonant frequency is a function of shape, dimension and permittivity of the dielectric material. Although several shapes of DRAs exist (e.g. hemispherical, cylindrical, rectangular, conical) the rectangular DRA is the most widely used since it offers multiple degrees of freedom and is easily fabricated. The dimensions of DRAs are proportional to $\lambda_o/\sqrt{\varepsilon_r}$, where λ_o is the free space wavelength at the resonant frequency and ε_r is the dielectric constant of the material [53]. This further adds to the appeal of DRAs as they can be designed to be quite compact. Additionally, DRAs have become an attractive option in recent years due to their very

low losses leading to high radiation efficiencies (better than 95%) and their ability to operate over very large frequencies by simply varying the dimensions and dielectric constant. DRAs are also quite versatile as several different feeding mechanisms can be employed, such as probes, apertures, microstrip lines and dielectric image guides, among others. DRAs are also well suited for mobile communication handsets since they can be placed on a ground plane and are by nature low gain antennas whose radiation patterns typically resemble those of short electric or magnetic dipoles.

2.4.1 Rectangular DRA

As previously mentioned, the rectangular DRA is the most versatile since it is characterized by its height *h*, width *w*, depth *d* and dielectric constant ε_r, as shown in Figure 13. Therefore, a rectangular DRA can be designed to have various *w/h* and *w/d* ratios with different dielectric constants in order to meet a specified frequency of operation.

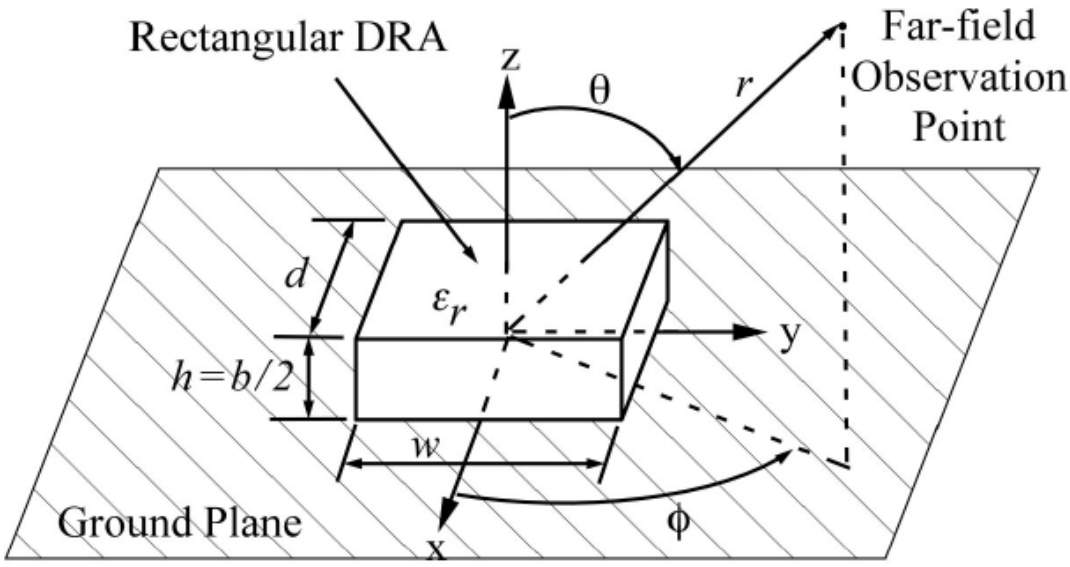

Figure 13: Geometry of the Rectangular DRA (After [53])

In order to analyze the fields of a rectangular DRA, the approximate dielectric waveguide model (DWM) can be employed [54]. According to the DWM method of analysis, the rectangular DRA is assumed to be a truncated section of an infinite dielectric waveguide of width *w* and height *b=2h* (due to the image effect of the ground plane). Although the modes in a dielectric waveguide are either TE or TM, because the DRA is placed over a ground plane the TE modes are most typically excited [52]. The rectangular DRA can thus support TE^x, TE^y and TE^z modes,

which are dependent on the dimensions of the DRA and the relationship between *w*, *d* and *h*. If $w > d > b$, then $f_x < f_y < f_z$ where f_x is the resonant frequency of the TE^x mode. Therefore, a rectangular DRA similar to the one shown in Figure 13 will have a resonant frequency f_{mn} of the $TE^x_{\delta mn}$ mode, which can be solved for by using the following transcendental equation:

$$k_x tan(k_x d/2) = \sqrt{\left((\varepsilon_r - 1)k_{mn}^2 - k_x^2\right)} \tag{2.4.1}$$

where,

$$k_{mn} = \frac{2\pi f_{mn}}{c} \qquad k_y = m\frac{\pi}{w} \quad k_z = n\frac{\pi}{b} \quad k_x^2 + k_y^2 + k_z^2 = \varepsilon_r k_{mn}^2 \tag{2.4.2}$$

and *m* and *n* are positive integers corresponding to the field variation within the y and z direction respectively. The E and H fields within the DRA for the various modes can be approximated by

$$E_x = 0 \tag{2.4.3}$$

$$E_y = k_z cos(k_x x)\left\{\frac{cos(k_y y)}{sin(k_y y)}\right\}\left\{\frac{sin(k_z z)}{cos(k_z z)}\right\} \tag{2.4.4}$$

$$E_z = -k_y cos(k_x x)\left\{\frac{sin(k_y y)}{cos(k_y y)}\right\}\left\{\frac{cos(k_z z)}{sin(k_z z)}\right\} \tag{2.4.5}$$

$$H_x = \frac{k_y^2 + k_z^2}{j2\pi\mu f_{mn}} cos(k_x x)\left\{\frac{cos(k_y y)}{sin(k_y y)}\right\}\left\{\frac{cos(k_z z)}{sin(k_z z)}\right\} \tag{2.4.6}$$

$$H_y = \frac{k_x k_y}{j2\pi\mu f_{mn}} sin(k_x x)\left\{\frac{sin(k_y y)}{cos(k_y y)}\right\}\left\{\frac{cos(k_z z)}{sin(k_z z)}\right\} \tag{2.4.7}$$

and

$$H_z = \frac{k_x k_z}{j2\pi\mu f_{mn}} sin(k_x x)\left\{\frac{cos(k_y y)}{sin(k_y y)}\right\}\left\{\frac{sin(k_z z)}{cos(k_z z)}\right\} \tag{2.4.8}$$

where the upper functions are chosen when the values of *m* or *n* are odd and the lower functions when *m* or *n* are even. The fields within a rectangular dielectric resonator are shown in Figure 14 for the lowest order mode, $TE^x_{\delta 11}$. As is evident in Figure 14 the field distribution resembles that of a horizontal short magnetic dipole oriented in the direction of the x-axis.

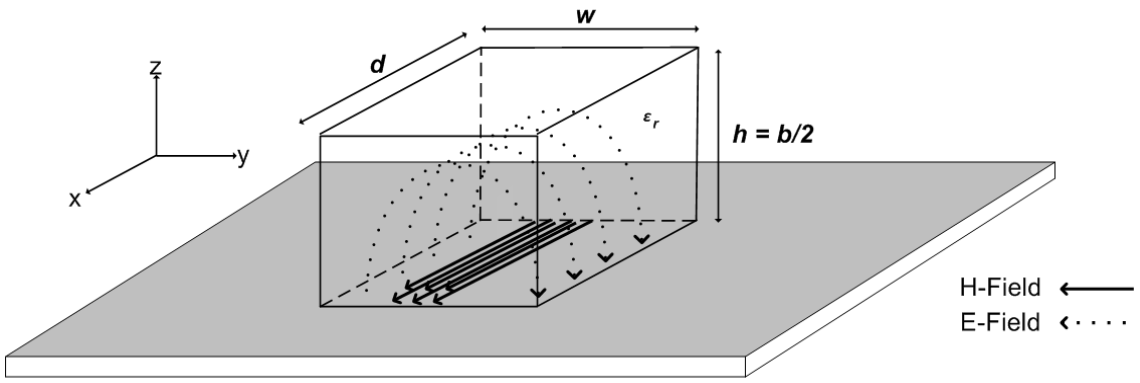

Figure 14: Electric and Magnetic Fields within a Rectangular DRA Operating in the $TE^x_{\delta 11}$ Mode

With the magnetic dipole in mind one could envision the $TE^x_{\delta 13}$ mode to be similar to that of Figure 14 except that there would be three short magnetic dipoles on top of one another separated by some distance in the z direction as is shown in Figure 15 (only two are shown due to the image effect of the ground plane). Since the rectangular DRA is analogous to a short magnetic dipole for the TE modes it follows that the radiation pattern obtained is very similar to that of the magnetic dipole as shown in Figure 16.

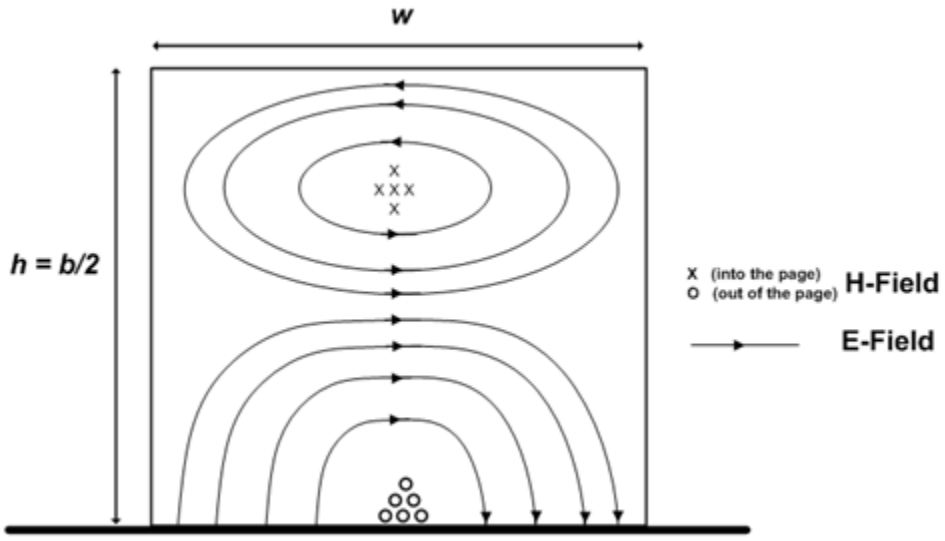

Figure 15: Electric and Magnetic Fields within a Rectangular DRA Operating in the $TE^x_{\delta 13}$ Mode

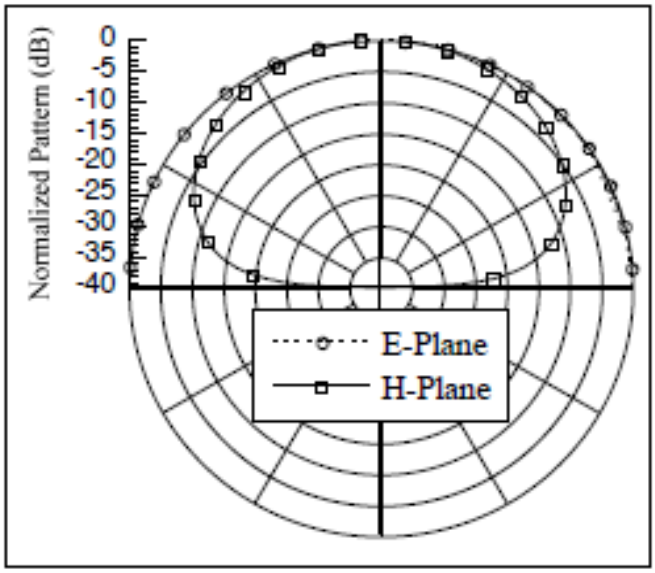

Figure 16: Ideal Radiation Pattern of Rectangular DRA Operating in the $TE^{x}_{\delta 11}$ Mode (After [53])

2.4.2 Coupling to Rectangular DRAs

Since a comprehensible depiction of the internal electric and magnetic fields of the rectangular DRA have been established a method to excite the DRA can be figured out. In most cases the $TE^{x}_{\delta 11}$ mode is desired, so in order to excite the DRA a mechanism whose fields correlate well with that of the desired mode will provide sufficient coupling. One effective method to excite a DRA is through an aperture in the ground plane. An added benefit to using this format of excitation is that the aperture itself can be fed by a transmission line whose feed network is located below the ground plane, isolating the radiating structure from any unwanted coupling or spurious radiation from the feed [53]. Since the electric fields within an aperture can be considered equivalent to a magnetic current parallel to the length of the slot, strong coupling can be achieved by positioning a rectangular DRA over the slot so that the length of the slot is perpendicular to the width of the rectangular DRA, as indicated in Figure 17.

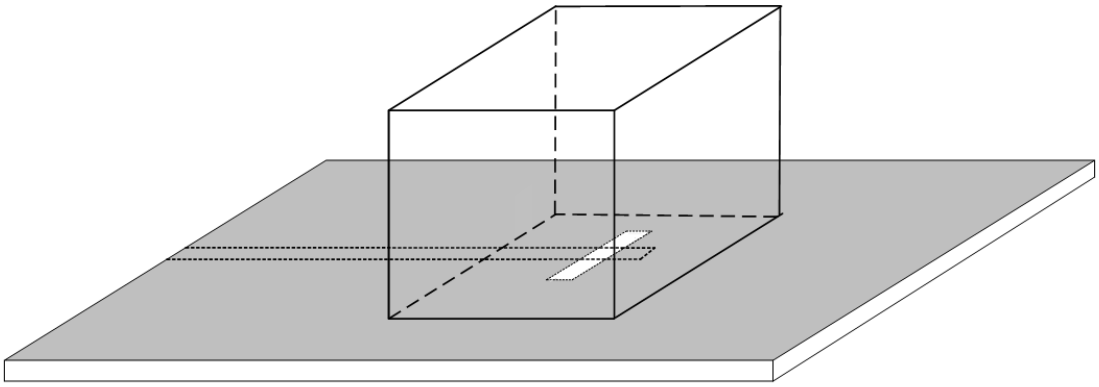

Figure 17: Microstrip Fed Aperture-Coupled Rectangular DRA for $TE^{x}_{\delta 11}$ Mode Operation

Other methods to excite a rectangular DRA include using a probe that protrudes through the ground plane [55], microstrip line coupling [56], coplanar line coupling [57] and dielectric image guide coupling [58].

2.5 References for Chapter 2

[1] J.T. Bernhard, *Reconfigurable Antennas*. Chicago, IL: Morgan & Claypool Publishers, 2007.

[2] P.H. Rao, "Antenna configurations for software defined radio and cognitive radio communication architecture," in *Wireless Communication and Sensor Computing*, Chennai, 2010, pp. 1-4.

[3] M. Dillinger et al., *Software Defined Radio: Architectures, Systems, and Functions*. West Sussex: John Wiley & Sons Ltd, 2003.

[4] Y. Hur et al., "A wideband analog multi-resolution spectrum sensing (MRSS) technique for cognitive radio (CR) systems," in *IEEE International Symposium On Circuits and Systems*, Island of Kos, 2006, pp.490-493.

[5] P. Deo, A. Mehta, D. Mirshekar-Syahkal, P.J. Massey, H. Nakano, "Beam steerable square loop antenna over hybrid high impedance surface," *Electronics Letters*, vol.45, no.19, pp.962-964, Sept. 2009.

[6] J. Sarrazin, Y. Mahe, S. Avrillon, S. Toutain, "Pattern reconfigurable cubic antenna," *IEEE Transactions on Antennas and Propagation,* vol.57, no.2, pp.310-317, Feb. 2009.

[7] M. Boti, L. Dussopt, M. Laheurte, "Circularly polarised antenna with switchable polarisation sense," *Electronics Letters*, vol.36, no.18, pp.1518-1519, Aug 2000.

[8] F. Ferrero, C. Luxey, R. Staraj, G. Jacquemod, M. Yedlin, V.F. Fusco, "Patch antenna with linear polarisation tilt control," *Electronics Letters* , vol.45, no.17, pp.870-872, Aug. 2009.

[9] A. Khaleghi, M. Kamyab, "Reconfigurable Single Port Antenna With Circular Polarization Diversity," *IEEE Transactions on Antennas and Propagation,* vol.57, no.2, pp.555-559, Feb. 2009.

[10] A. Petosa, "Frequency agile antennas for wireless communications – A survey," in *Antenna Technology and Applied Electromagnetics & the American Electromagnetics Conference (ANTEM-AMEREM),* Ottawa, 2010, pp.1-4.

[11] A.C.K Mak, C.R. Rowell, R.D. Murch, M. Chi-Lun, "Reconfigurable Multiband Antenna Designs for Wireless Communication Devices," *IEEE Transactions on Antennas and Propagation,* vol.55, no.7, pp.1919-1928, Jul. 2007

[12] S.Liu, M.J. Lee, C. Jung, G.P. Li, F. De Flaviis, "A frequency-reconfigurable circularly polarized patch antenna by integrating MEMS switches," in *IEEE Antennas and Propagation Society International Symposium,* Washington DC, 2005, pp. 413- 416.

[13] C.Zhang, S.Yaing, H.K. Pan, A.E. Fathy, S. El-Ghazaly, V. Nair, "Development of reconfigurable mini-nested patches antenna for universal wireless receiver using MEMS," in *IEEE Antennas and Propagation Society International Symposium,* Albuquerque, NM, 2006, pp.205-208.

[14] P. Panaia, C. Luxey, G. Jacquemod, R. Staraj, G. Kossiavas, L. Dussopt, F. Vacherand, C. Billard, "MEMS-based reconfigurable antennas," in *IEEE International Symposium on Industrial Electronics,* Ajaccio, 2004, pp. 175- 179

[15] R. Valkonen, C. Luxey, J. Holopainen, C. Icheln, P. Vainikainen, "Frequency-reconfigurable mobile terminal antenna with MEMS switches," in *Proceedings of the Fourth European Conference on Antennas and Propagation,* Barcelona, 2010, pp.1-5.

[16] D.E. Anagnostou, G. Zheng, T. Chryssomallis, J.C. Lyke, G.E.Ponchak, J. Papapolymerou, C.G. Christodoulou, "Design, Fabrication, and Measurements of an RF-MEMS-Based Self-Similar Reconfigurable Antenna," *IEEE Transactions on Antennas and Propagation*, Vol. 54, No. 2, pp. 422-432, Feb. 2006.

[17] N. Kingsley, D.E. Anagnostou, M. Tentzeris, J. Papapolymerou, "RFMEMS Sequentially Reconfigurable Sierpinski Antenna on a Flexible Organic Substrate With Novel DC-Biasing Technique," *Journal of Micromechanical Systems*, Vol. 16, No. 5, pp. 1185-1192, Oct. 2007.

[18] B. Cetiner, Q. Xu, and L. Jofre, "Frequency Reconfigurable Annular Slot Antenna" in *IEEE Antennas and Propagation Society International Symposium,* Honolulu HI, 2007, pp.5845-5848.

[19] R.K. Gupta, U.C. Sharma, P. Ayanu, and G. Kumar, "MEMS Based Reconfigurable Dual Band Antenna" *Microwave and Optical Technology Letters*, Vol. 50, No. 6, pp. 1570-1575, Jun. 2008.

[20] K. Topali, O.A. Civi, S. Demir, S. Koc, and T. Akin, "Dual-Frequency Reconfigurable Slot Dipole Array with a CPW-Based Feed Network using RF MEMS Technology for X- and Ka-Band

Applications," in *IEEE Antennas and Propagation Society International Symposium,*Honolulu HI, 2007, pp. 825-828.

[21] J. Kiriazi, H. Ghali H. Ragaie, and H. Haddara, "Reconfigurable Dual-Band Dipole Antenna on Silicon Using Series MEMS Switches," in *IEEE Antennas and Propagation Society International Symposium*, Columbus OH, 2003, pp. 403-406.

[22] C. Medeiros, J.R. Costa, and C.A. Fernandes, "MEMS Reconfigurable Stacked Antenna for WLAN Applications," in *IEEE Antennas and Propagation Society International Symposium*, San Diego CA, 2008.

[23] S. Kawasaki, T. Itoh, "A slot antenna with electronically tunable length," in *IEEE Antennas and Propagation Society International Symposium* London ON*,* 1991, pp.130-133.

[24] L.M. Feldner, C.T. Rodenbeck, C.G. Christodoulou, N. Kinzie, "Electrically Small Frequency-Agile PIFA-as-a-Package for Portable Wireless Devices," *IEEE Transactions on Antennas and Propagation,* vol.55, no.11, pp.3310-3319, Nov. 2007

[25] S. Nikolaou, K. Boyon, P. Vryonides, "Reconfiguring antenna characteristics using PIN diodes," in *Proceedings of the Third European Conference on Antennas and Propagation*, Berlin, 2009, pp.3748-3752

[26] A.F. Sheta, S.F. Mahmoud, "A Widely Tunable Compact Patch Antenna," *IEEE Antennas and Wireless Propagation Letters,* vol.7, pp.40-42, Mar. 2008

[27] J.M. Laheurte, "Switchable CPW-Fed Slot Antenna for Multifrequency Operation," *IEE Electronics Letters*, vol. 37, no. 25, pp.1498-1500, Dec. 2001.

[28] N.C. Karmakar, "Shorting Strap Tunable Stacked Patch PIFA," *IEEE Transactions on Antennas and Propagation*, Vol. 52, No. 11, pp. 2877-2884, Nov.2004.

[29] C.Y. Chiu and R.D. Murch, "Reconfigurable Multi-port Antennas for Handheld Devices," in *IEEE Antennas and Propagation Society International Symposium,* Charleston SC, 2009.

[30] S.B. Byun, J.A. Lee, J.H. Lim, T.Y. Yun, "Reconfigurable Ground-Slotted Patch Antenna using PIN Diode Switching," *Electronics and Telecommunications Research Institute Journal*, Vol. 29, No. 6, pp. 832-834, Dec. 2007.

[31] C. Luxey, L. Dussopt, J.L. Le Sonn, and J.M. Laheurte, "Dual-Frequency Operation of CPW-Fed Antenna Controlled by PIN Diodes," *IEEE Electronics Letters*, Vol. 36, No. 1, pp. 2-3, Jan. 2000.

[32] S. Nikolaou, R. Bairavasubramanian, C. Lugo, I. Carrasquillo, D.C.Thompson, G.E. Ponchak, J. Papapolymerou, and M.M. Tenzeris, "Pattern and Frequency Reconfigurable Annular Slot Antenna Using PIN Diodes," *IEEE Transactions on Antennas and Propagation*, vol.54, no. 2, pp. 439-448, Feb. 2006.

[33] W. Lee, H. Kim, and Y.J. Yoon, "Reconfigurable Slot Antenna with Wide Bandwidth," in *IEEE Antennas and Propagation Society International Symposium,* Honolulu HI, 2006, pp. 3063-3066.

[34] D. Peroulis, K. Sarabandi, and L.P.B. Katehi, "Design of Reconfigurable Slot Antennas," *IEEE Transactions on Antennas and Propagation*, vol. 53, no. 2, pp. 645-654, Feb. 2005.

[35] A.F. Sheta, and S.F. Mahmoud, "Widely Tunable Compact Patch Antenna," *IEEE Antennas and Wireless Propagation Letters*, vol. 7, pp. 40-42, 2008.

[36] G.H. Huff, D.L. Rolando, P. Walters, J. McDonald, "A Frequency Reconfigurable Dielectric Resonator Antenna Using Colloidal Dispersions," *IEEE Antennas and Wireless Propagation Letters,* vol.9, pp.288-290, 2010.

[37] J.T. Bernhard, E. Kiely, G. Washington, "A smart mechanically actuated two-layer electromagnetically coupled microstrip antenna with variable frequency, bandwidth, and antenna gain ," *IEEE Transactions on Antennas and Propagation,* vol.49, no.4, pp.597-601, Apr. 2001

[38] D.M. Pozar, V. Sanchez, "Magnetic tuning of a microstrip antenna on a ferrite substrate," *Electronics Letters*, vol.24, no.12, pp.729-731, Jun. 1988.

[39] R.K. Mishra, S.S. Pattnaik, N. Das, "Tuning of microstrip antenna on ferrite substrate," *IEEE Transactions on Antennas and Propagation,* vol.41, no.2, pp.230-233, Feb. 1993.

[40] A. Petosa, R.K. Mongia, M. Cuhaci, J.S. Wight, "Magnetically Tunable Ferrite Resonator Antenna," *IEEE Electronics Letters*, vol.30, no.13, pp.1021-1022, June 1994.

[41] C. Yong, Y.J. Guo, A.R. Weily, "A Frequency-Reconfigurable Quasi-Yagi Dipole Antenna," *IEEE Antennas and Wireless Propagation Letters,* vol.9, pp.883-886, 2010

[42] C.T.P. Song, Z.H. Hu, J. Kelly, P.S. Hall, P. Gardner, "Wide tunable dual-band reconfigurable antenna for future wireless devices," in *Loughborough Antennas & Propagation Conference,* Loughborough*, 2009,* pp.601-604.

[43] M. Abdallah, L. Le Coq, F. Colombel, G. Le Ray, M. Himdi, "Frequency tunable monopole coupled loop antenna with broadside radiation pattern," *Electronics Letters* , vol.45, no.23, pp.1149-1151, Nov. 2009

[44] S.K. Oh, Y.S. Shin, S.O. Park, "A Novel PIFA Type Varactor Tunable Antenna with U-Shaped Slot," in *International Symposium on Antennas, Propagation and EM Theory,* Guilin, 2006.

[45] M. Berg, M. Komulainen, V. Palukuru, H. Jantunen, and E. Salonen, "Frequency-Tunable DVB-H Antenna for Mobile Terminals," in *IEEE Antennas and Propagation Society International Symposium,* Honolulu HI, 2007, pp. 1072-1075.

[46] V.A. Nguyen, R.A. Bhatti, and S.O. Park, "A Simple PIFA-Based Tunable Internal Antenna for Personal Communication Handsets" *IEEE Antennas and Wireless Propagation Letters*, vol. 7, pp.130-133, 2008.

[47] N. Behdad and K. Sarabandi, "Dual-Band Reconfigurable Antenna With a Very Wide Tunability Range," *IEEE Transactions on Antennas and Propagation*, vol. 54, no. 2, pp. 409 – 416, Feb. 2006.

[48] I. Carrasquillo-Rivera, R.A. Rodgriguez Solis, J.G. Colom-Ustariz, "Tunable and Dual-Band Rectangular Slot-Ring Antenna," in *IEEE Antennas and Propagation Society International Symposium,* Monterey CA, 2004, pp. 4308-4311.

[49] F. Costa, A. Monorchio, S. Talrico, F.M. Valeri, "An Active High-Impedance Surface for Low-Profile Tunable and Steerable Antennas," *IEEE Antennas and Wireless Propagation Letters*, vol. 7, pp.676-680, 2008.

[50] H. Li, J. Xiong, Y. Yu, S. He, "A Simple Compact Reconfigurable Slot Antenna With a Very Wide Tuning Range," *IEEE Transactions on Antennas and Propagation,* vol.58, no.11, pp.3725-3728, Nov. 2010

[51] L. Jong-Hyuk, B. Gyu-Tae, K. Young-Il, S. Chang-Wook, Y. Tae-Yeoul, "A Reconfigurable PIFA Using a Switchable PIN-Diode and a Fine-Tuning Varactor for USPCS/WCDMA/m-WiMAX/WLAN," *IEEE Transactions on Antennas and Propagation*, vol.58, no.7, pp.2404-2411, Jul. 2010

[52] A. Petosa, *Dielectric Resonator Antennas Handbook*, Artech House Inc., 2007.

[53] A. Petosa, S. Thirakoune, A. Ittipiboon, "Higher-order modes in rectangular DRAs for gain enhancement," in *Antenna Technology and Applied Electromagnetics and the Canadian Radio Science Meeting,* Banff ,2009, pp.1-4.

[54] R.K. Mongia, "Theoretical and experimental resonant frequencies of rectangular dielectric resonators," *IEE Proceedings, Microwaves, Antennas and Propagation,* vol.139, no.1, pp.98-104, Feb. 1992

[55] M.W. McAllister, S.A. Long, G.L. Conway, "Rectangular dielectric resonator antenna," *Electronics Letters*, vol.19, no.6, pp.218-219, Mar. 1983.

[56] R.A. Kranenburg, S.A. Long, "Microstrip transmission line excitation of dielectric resonator antennas," *Electronics Letters* , vol.24, no.18, pp.1156-1157, Sept. 1988

[57] R.A. Kranenburg, S.A. Long, J.T. Williams, "Coplanar waveguide excitation of dielectric resonator antennas," *IEEE Transactions on Antennas and Propagation,* vol.39, no.1, pp.119-122, Jan. 1991.

[58] M.T. Birand, R.V. Gelsthorpe, "Experimental millimetric array using dielectric radiators fed by means of dielectric waveguide," *Electronics Letters*, vol.17, no.18, pp.633-635, Sept. 1981.

Chapter 3 - Reconfigurable DRA - Ideal Switching

3.1 Introductory Remarks

In this chapter a method for achieving frequency agility with a dielectric resonator antenna is presented using ideal switches. The theoretical tuning range performance of the single-wall reconfigurable DRA is examined for various aspect ratios and a study is performed on various switching geometries. An optimum design is then presented along with simulation and measured data showing the frequency response and radiation pattern followed by a discussion of the design. A dual-wall reconfigurable DRA is then presented to address some of the shortcomings inherent in the single-wall design. Again simulated and measured data showing frequency response and radiation pattern are presented and discussed.

3.2 Reconfigurable DRA with Single Shorting Wall

In order to achieve frequency agility the concept of an edge grounded rectangular DRA is applied [1]. An edge grounded DRA, as shown in Figure 18, consists of a metalized wall along one of the DRA faces that is connected to the ground plane. With the shorting wall in place the boundary conditions on the shorting wall-DRA interface force the electric fields to be normal to the conductor and the magnetic fields to be tangential. This necessitates the fields within the DRA to take the form shown in Figure 19 for the lowest order $TE^{x}_{\delta 11}$ mode. It is clear from Figure 19 that if a rectangular DRA of dimension *w*, d and h were altered to be w/2, d and h and an infinite PEC wall is placed in the x-z plane at one of the DRA-air interfaces the resonant frequency would be identical and the field configuration would not be altered, while the volume of the DRA would be halved. Therefore, if a shorting wall is placed in the x-z plane a similar result will be obtained.

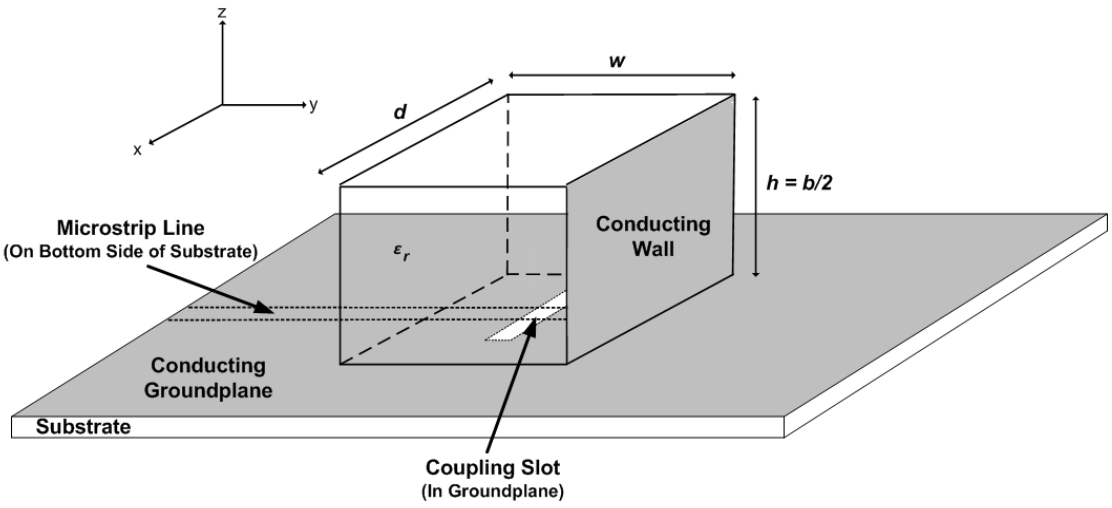

Figure 18: Edge Grounded Rectangular Dielectric Resonator Antenna

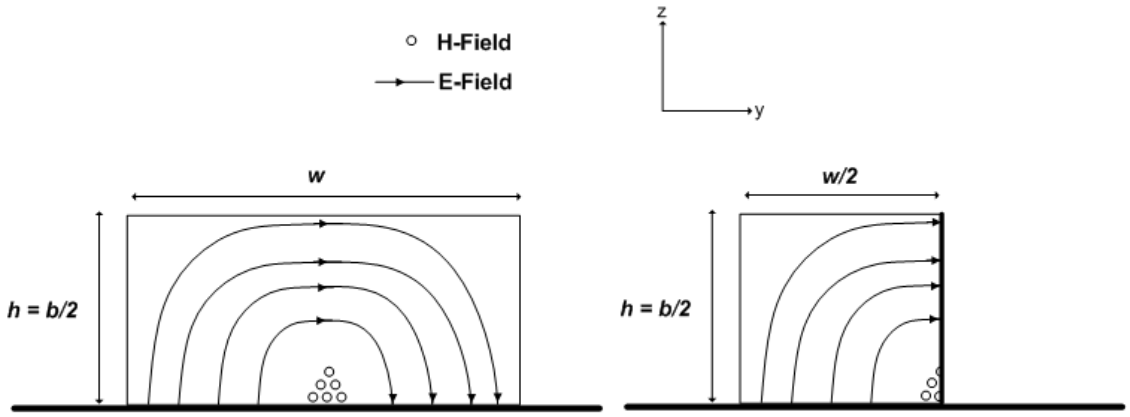

Figure 19: Field Configuration of Edge Grounded Rectangular Dielectric Resonator Antenna

It then follows that if a rectangular DRA of dimensions $w \times d \times h$ had an edge grounded shorting wall added to it, the resonant frequency would subsequently be decreased as the width, *w,* would effectively be doubled. As an example, solving for the transcendental equation (2.4.1) for a rectangular DRA of dimension 12.25mm × 12.25mm × 12.25mm and dielectric constant of 10 results in a resonant frequency of 5 GHz. If an edge grounded shorting wall is added the resonant frequency drops to 3.47 GHz. One can then achieve frequency agility by placing a conducting wall on a rectangular DRA and by inserting a small gap between the ground plane and the conducting wall. Switches are then added so that the conducting wall can be switched between shorted and non-shorted states (with respect to the groundplane), as shown

in Figure 20. This technique was first explored by Petosa *et al.* [2], which laid the foundation for the work performed in this thesis.

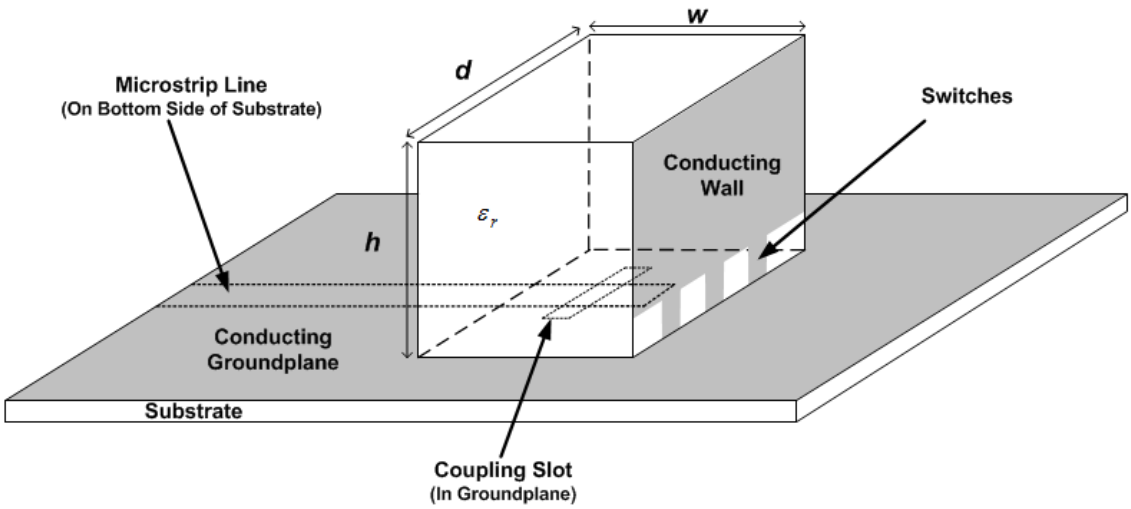

Figure 20: Geometry of Single Conducting Wall Reconfigurable Dielectric Resonator Antenna of Height *h*, depth *d* and width *w*.

3.2.1 Electromagnetic Simulation Validation

As a starting point for the research that was performed on frequency reconfigurable DRAs the results obtained by Petosa *et al.*[2] were first replicated using HFSS [3] (finite element method) and FEKO [4] (method of moments) and compared to simulation results obtained by the authors of [2] using the commercial code EMPIRE [5] (finite difference time domain method). The simulation was performed with three different commercial electromagnetic modeling codes based on different computational techniques, in particular the "big three": the finite element method, the method of moments and the finite-difference time-domain method. One can then compare predictions for the same device when it is modeled using two or more different methods. Good agreement between simulation results obtained using different techniques is a good indicator that the modeling process is sound. This would ensure that all future work performed with HFSS and FEKO, which the present author had at his disposal, can be regarded as accurate.

The particulars of the specific example to be used in the simulation comparisons are given in Figure 21 and Table 2.

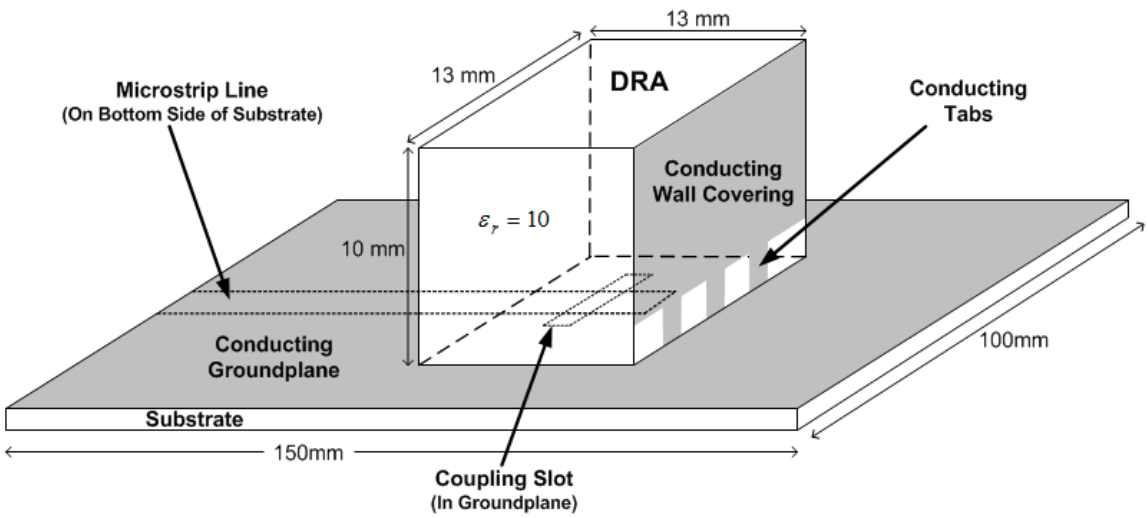

Figure 21: Slot-fed DRA with Conductor Loading

For convenience the tab configuration shown in Figure 21 will be designated as SSS (since each of the three tabs is "shorted" to the ground plane). If the outer tabs were to be removed (so that these tabs are "open", with the center tab still connected to the ground plane) we would call it the OSO tab configuration. In the modeling we "open" the tab by removing it completely. Therefore, since there are 3 tabs that can be "shorted" or left "open" we obtain 6 unique antenna configurations (OOO, OOS, OSO, SOS, OSS and SSS) that allow discrete tuning.

Table 2: Slot-fed DRA with Conductor Loading Model Parameter Values

Feature	Dimension (mm)	ε_r
Substrate Length	150	-
Substrate Width	100	-
Substrate Height	0.508	-
Substrate ε_r	-	3.38
Microstrip Width	1.18	-
Microstrip Length	81	-
Microstrip Stub Length	6	-
Aperture Length	10	-
Aperture Width	1	-
DRA Width	13	-
DRA Depth	13	-

DRA Height	10	-
DRA ε_r	-	10
Tab Width	2	-
Tab Separation	1.75	-
Tab Height	1	-

All three methods modeled the finite substrate and ground plane with the same dimensions as were used for the physical model. The only dissimilarity between the models that are not related to inherent differences between the methods is that the HFSS model is fed using a waveport [3], the FEKO model is fed using a small wire connecting the ground plane to the centre of the microstrip line a small distance away from the edge of the substrate [4], and the EMPIRE model uses an edge port [5] similar to HFSS. In spite of this we will see that the difference between predicted input impedances is relatively small. This serves to strengthen one's confidence in modern-day computational tools that are properly used.

As is evident in Figure 22 and Figure 23 there is very good agreement between the three computational techniques in terms of frequency response. More importantly, as far as this thesis work is concerned, is how close even the low values are for a quantity (namely the input reflection coefficient) that is far more sensitive to small solution errors than are the far-zone radiation patterns. Even before one proceeds to hardware testing, such agreement provides the assurance a designer needs to know that the modeling has been done properly (and assuredly within the limits of state-of-the-art simulation tools). Although only two cases are shown they are representative of what was found for all six tab configurations. It is also apparent in Figure 24 that good agreement was also obtained for the radiation patterns. Again this result was observed in all cases. Since the three simulation techniques were all in very good agreement, the author is confident that future simulations can be performed with the knowledge that when realized large discrepancies should not be expected.

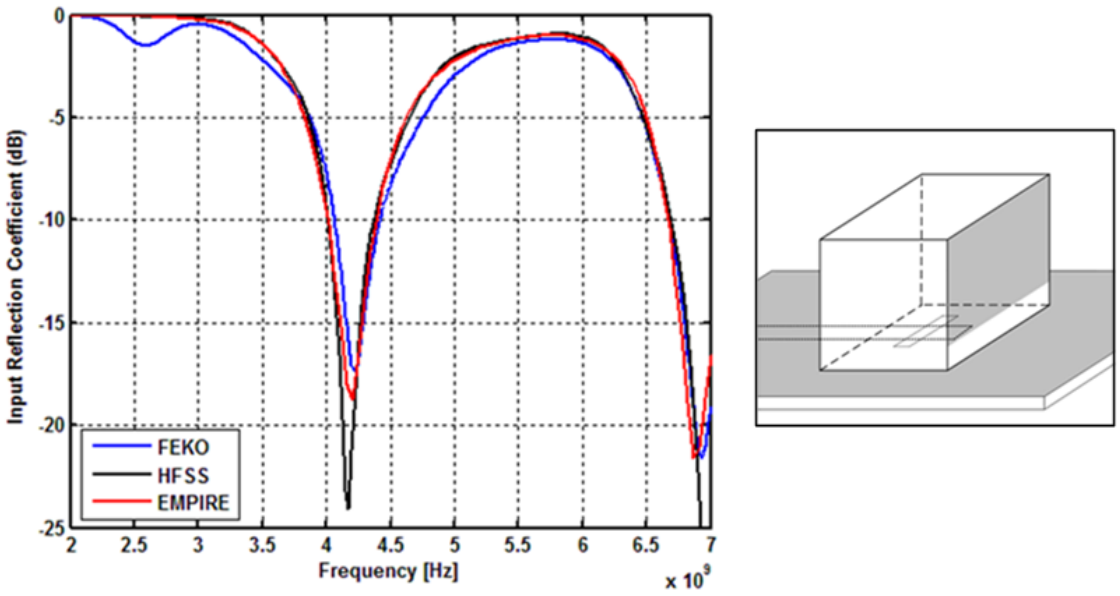

Figure 22: Comparison of Frequency Response for OOO Configuration using FEKO, HFSS and EMPIRE

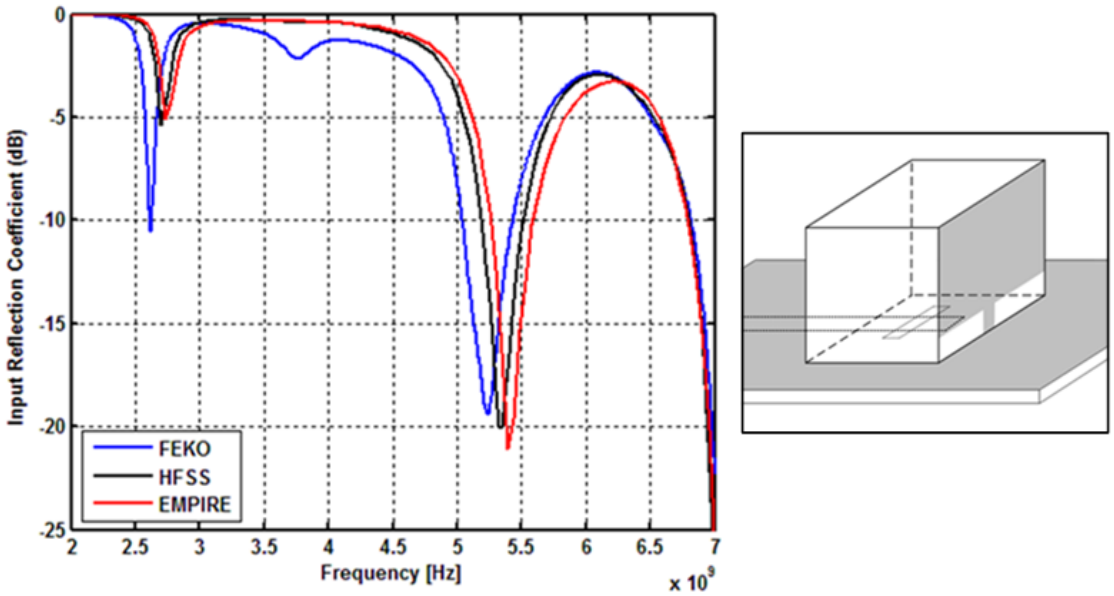

Figure 23: Comparison of Frequency Response for OSO Configuration using FEKO, HFSS and EMPIRE

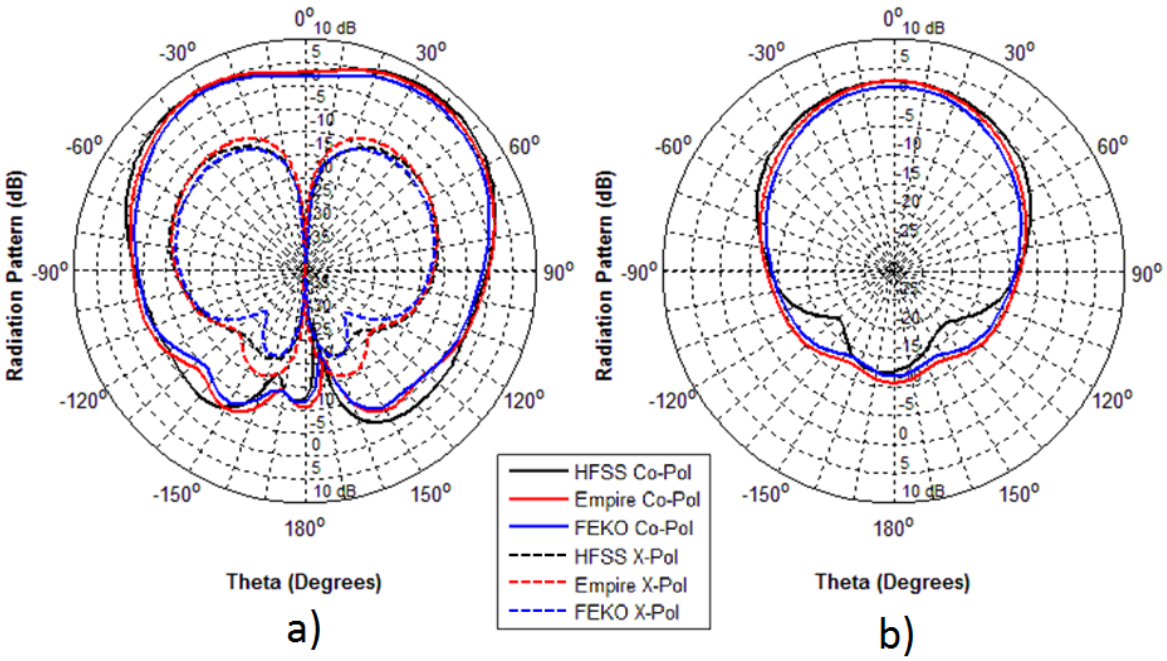

Figure 24: Comparison of Radiation Pattern for OOO Configuration using FEKO, HFSS and EMPIRE. a) H-Plane (xz-plane) b) E-Plane (yz-plane)

3.2.2 Aspect Ratio Study

In order to maximize the tuning range of the reconfigurable DRA, various aspect ratios were examined. Since the achievable tuning range is dependent on the difference in operating frequency with and without the shorting wall, the transcendental equation (2.4.1) was solved for various DRA geometries to predict tuning range. As shown in Figure 25, the predicted tuning range increases with increasing aspect ratio ($2h/d$) and with decreasing width to depth ratio (w/d). The result is intuitive as with increasing aspect ratio and with decreasing width to depth ratio the shorting wall occupies a greater percentage of total surface area. It is also clear from Figure 25 that although the tuning range increases with aspect ratio, it begins to level off and it is clear that a smaller width to depth ratio is preferred in order to maximize tuning range. The theoretical tuning range was also examined for various dielectric constants. As shown in Figure 26, the tuning range is more or less independent of the dielectric constant. However, this is not the case for dielectric constants less than 5, which are seldom used in DRAs. It is also shown that the predicted tuning range is purely a function of the relationship between the aspect ratio, width – depth ratio and dielectric constant since the overall size of the DRA has no impact on the tuning range as shown in Figure 27. This is an important conclusion as it demonstrates that the tuning range is not a function of operating frequency which means that a frequency

reconfigurable DRA can be scaled via dimension and dielectric constant to operate at various frequencies with only minor variations in the achievable tuning range.

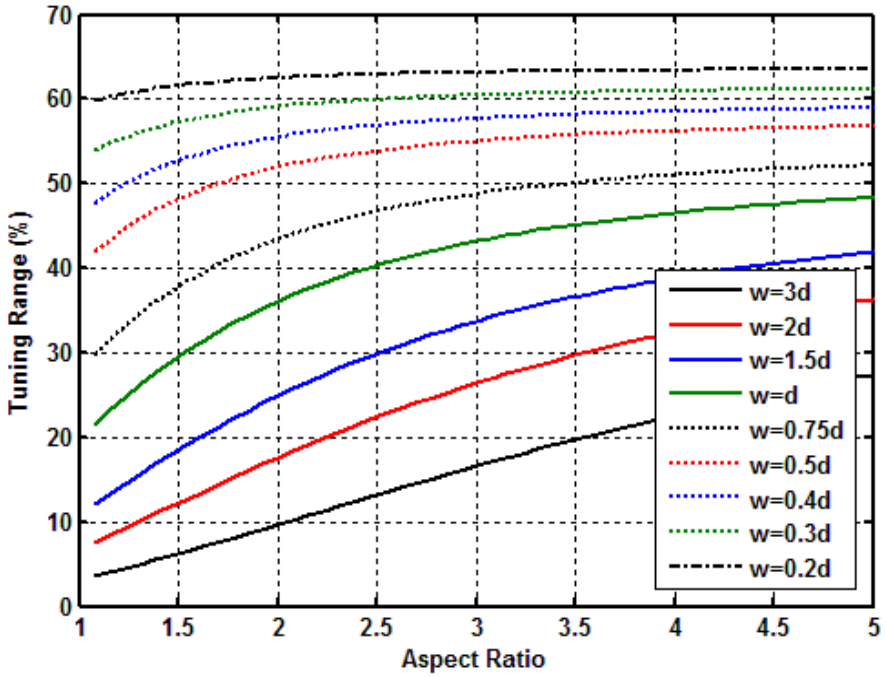

Figure 25: Theoretical Tuning Range as a Function of Aspect Ratio (2h/d) for Various Width – Depth Ratios(w/d) for a DRA with ε_r=10

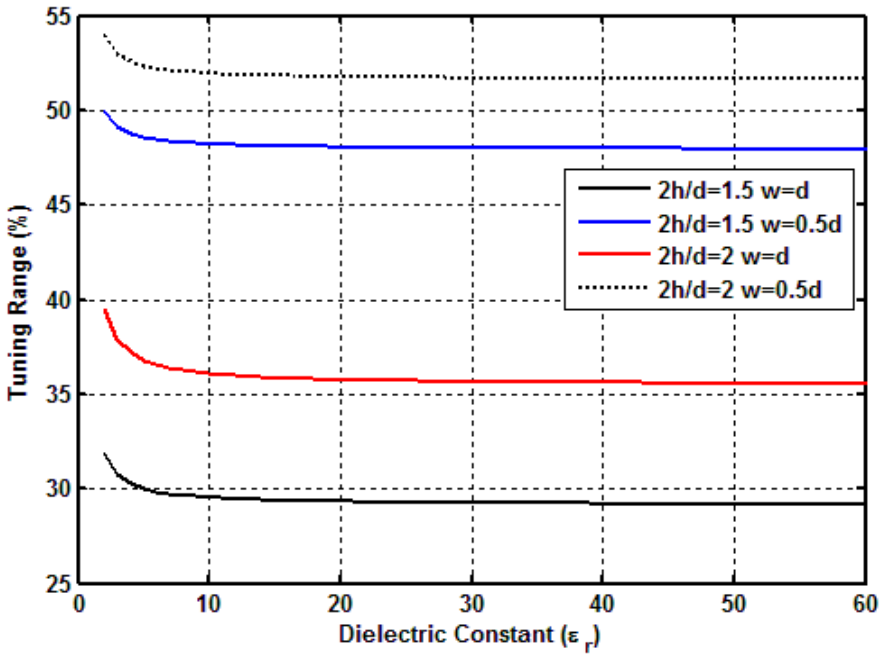

Figure 26: Theoretical Tuning Range as a Function of Dielectric Constant for Various Aspect Ratio (2h/d) and Width–Depth Ratio (w/d) Combinations

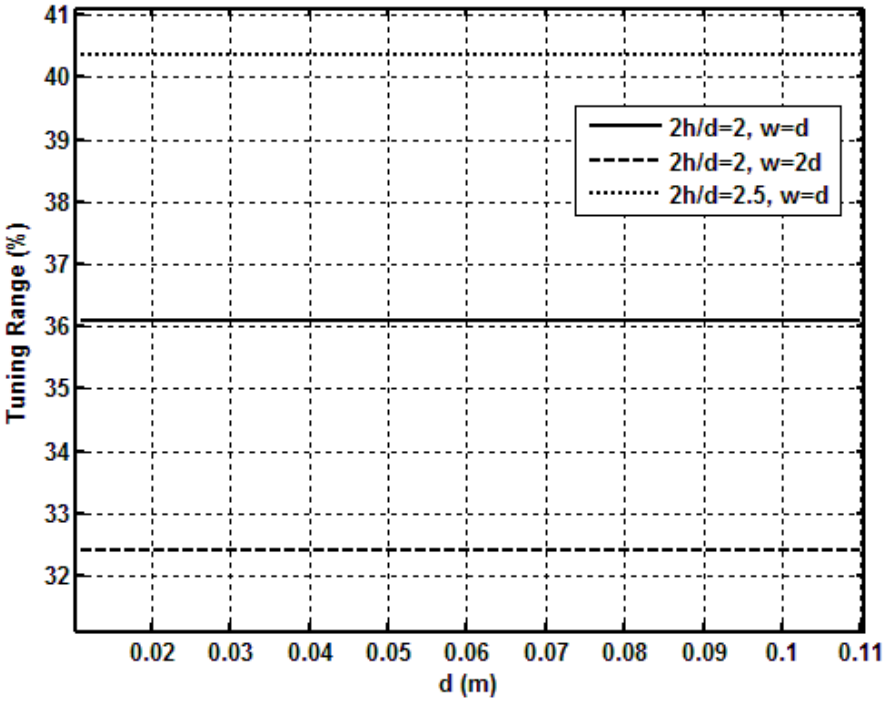

Figure 27: Theoretical Tuning Range as a Function of DRA Size for Various Aspect Ratio (2h/d) and Width – Depth Ratio (w/d) Combinations for a DRA with ε_r=10

In order to verify the theoretical results in Figure 25, several rectangular DRAs were simulated with and without a shorting wall using FEKO and HFSS. The resonant frequencies, tuning range, radiation pattern and input reflection coefficient were then compared in order to determine an optimum aspect ratio. The result of several simulations is shown in Figure 28. It is clear that the relationships observed in the theoretical tuning range predictions from (2.4.1) correspond well to that found from full electromagnetic simulation. Although it appears that as the aspect ratio increases the tuning range decreases, simulation data indicates that this is only because when the aspect ratio is greater than two there is very poor coupling and unintended modes begin to resonate. It is also clear that the DRA dimensions which lead to the greatest tuning range is 7.15 × 13 × 9.75 (all dimensions in mm and ε_r=10) which leads to a theoretical tuning range of 46% and a simulated tuning range of 66% for a fixed feed line and aperture. Therefore, since the microstrip feed and aperture were not optimized for each configuration, additional performance gains may be possible.

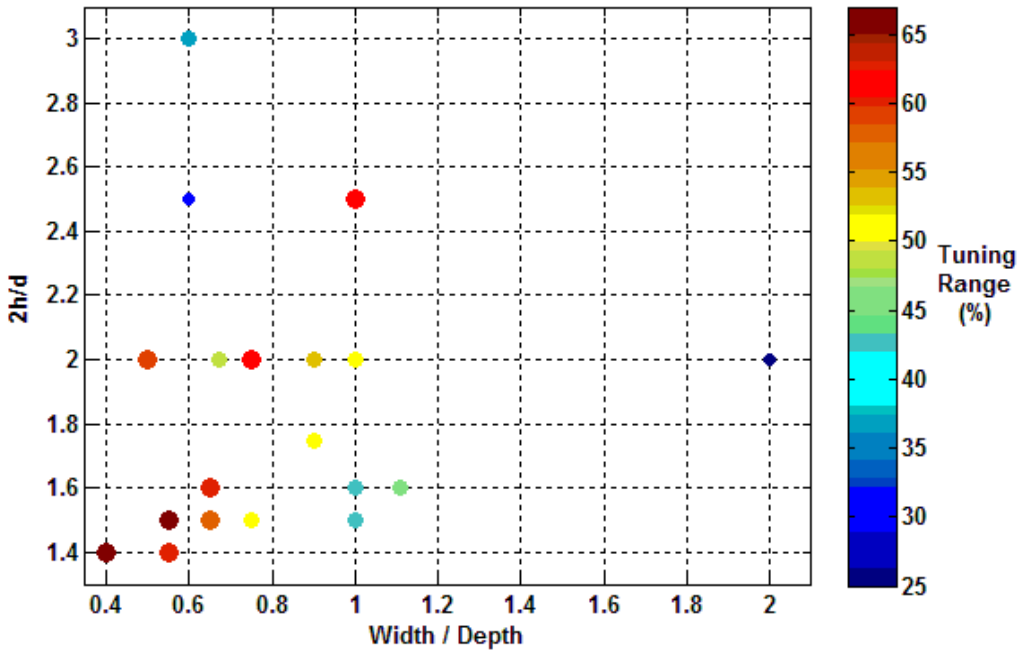

Figure 28: Simulated Tuning Range as a Function of Aspect Ratio (2h/d) and Width – Depth Ratio(w/d) for DRAs with ε_r=10

3.2.3 Tab Geometry

In order to determine the optimal method of switching a brief study was performed on different aspects of the ideal switches (tabs) for the DRA shown in Figure 21 using HFSS. The spacing between the tabs was varied along with the width and height of the tabs. However, these changes had very little impact on the operating bands of the antenna and only resulted in slight frequency shifts. This is to a certain extent encouraging as it demonstrates the robustness of the antenna as small changes in the tabs do not have much of an impact which adds to the design tolerance of the antenna.

In addition to the variations made to the tabs, numerical experimentation was performed with the number of tabs used. The performance of the 3-tab reconfigurable DRA was compared to both 4-tab and 5-tab versions that had identical DRA dimensions. A summary of the tab geometry is shown in Table 3.

Table 3: Tab Configuration and Geometry for the 3, 4 and 5 Tab Reconfigurable DRA (All Physical Dimension in mm)

# of Tabs	Tab width	Inter Tab Spacing	# of Permutations	# of Unique Permutations
3 Tabs	2	1.75	8	6
4 Tabs	1.5	1.4	16	10
5 Tabs	1.25	1.125	32	18

For the 4- and 5-tab configurations all unique permutations were simulated and the results were observed. It was clear that adding tabs does not enhance the tuning range of the antenna but rather provides a greater contiguous operating band as shown in Figure 29. In Figure 29, all data points pictured represent where there is a -10 dB input reflection or better. In other words it displays the tuning range of the antenna along with all tuning operating bands that meet the specification of a 10 dB return loss or better. It is clear that in the 5-tab case the antenna is capable of contiguous frequency tuning from 5.5 GHz to 6.5 GHz while the 3- and 4-tab configurations are not capable of satisfying a -10 dB match between 5.5 GHz and 6 GHz. Another attribute of having more tabs is that there is significant redundancy as several tab combinations lead to the same frequency response, albeit with minor shifts. It was also observed that adding tabs does not improve the radiation pattern in regards to gain or cross polarization levels.

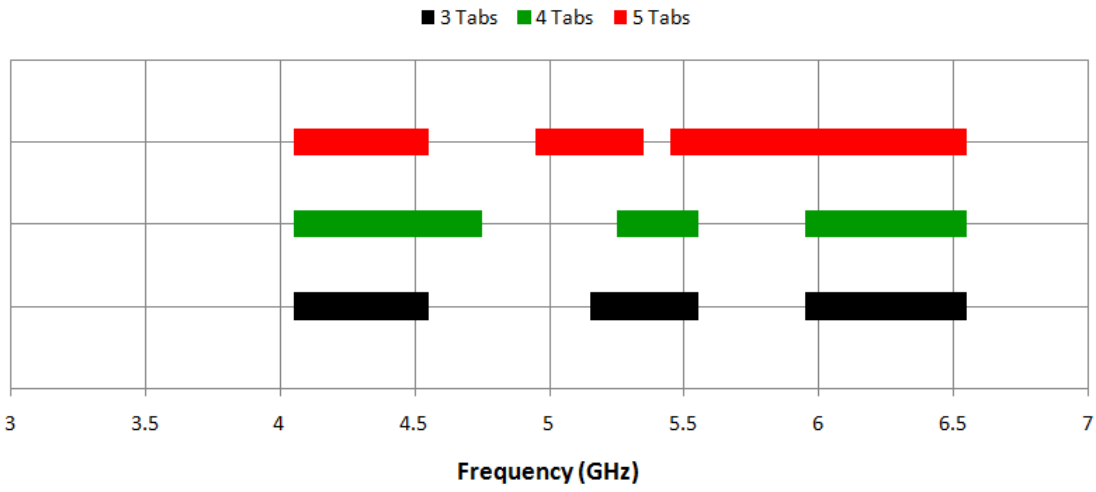

Figure 29: Tuning Range and Operating Bands Satisfying a 10 dB Return Loss or Better for the 3, 4 and 5 Tab Reconfigurable DRA

Although the additional tabs do in fact increase the performance level of the antenna, in regards to operating bands, the added complexity in contrast to the benefits of additional switches do not deem it worthwhile.

3.2.4 Optimum Design for Tuning Range

With the knowledge gained from the studies discussed in the previous sections, an optimal design was obtained based on the tradeoffs between tuning range, radiation pattern and return loss. As a starting point the rectangular DRA of dimension 7.15mm × 13mm × 9.75mm for *w, d, h* and a dielectric constant of 10 was chosen as it provides the greatest tuning range as determined by the aspect ratio study of Section 3.2.2. The dimensions correspond to an aspect ratio of 1.5 and a width – depth ratio of 0.55. The dimensions of the DRA gave a theoretical tuning range of 46% while simulation showed 66%, when a solid shorting wall is used. From the results of Section 3.2.3, a gap of 1 mm between the edge grounded shorting wall and ground plane was chosen along with tabs of width 0.5 mm. The tab width was selected to be 0.5 mm since this value best represents the package size of the active switching devices that will be used (PIN diode in Chapter 4 and varactor diode in Chapter 5). The shorting wall was also designed with 300 µm vertical gaps (which we will call "bias gaps") in order to facilitate the eventual need for the separation of bias voltages. The shorting wall and tab configuration was printed using an etching process on 25 mil Rogers 6010 substrate that had a relative dielectric constant of 10.2. Printing the shorting wall and tab configuration onto a thin substrate was required since it was not possible to deposit the shorting wall configuration directly onto the DRA. The shorting wall would then be cut to size and bonded to the DRA using a silicone bonding agent (Corning 732), as shown in Figure 30. Since the shorting wall substrate had a thickness of 25 mils (0.635 mm) the DRA was fabricated to have a width of only 6.515 mm so that the total width would be 7.15 mm. A ground plane of 150 mm by 100 mm is used with an aperture of length 10mm and width 1mm centered on the ground plane. The substrate which contains the ground plane had a thickness of 0.508mm and a relative dielectric constant of 3.38. The aperture is coupled via a microstrip line of width 1.18 mm and length 81 mm that has a characteristic impedance of 50Ω. The microstrip line extends 6 mm past the aperture and behaves like an open-circuit stub with respect to the center of the aperture. The length of the stub is selected so that the imaginary component of the slot admittance is reduced, resulting in an improved impedance match to the microstrip line. The DRA, complete with shorting wall, was then bonded to the ground plane and, depending on the particular configuration, the tabs were soldered to the ground plane in order to ensure a good electrical connection. The single-wall reconfigurable DRA is shown in Figure 30 with the applicable dimensions.

Since there are six different unique shorting wall configurations, six separate antennas had to be constructed. Once the antennas were fabricated the input reflection coefficient was measured and compared to simulation using HFSS. The results are shown in Figure 31 to Figure 36 with a summary in Figure 37. It is clear from the results that the simulation was fairly accurate as there is very good correlation between simulated and measured results. This also demonstrates that the fabrication technique is robust, as the following design aspects could easily have led to large errors:

- Positioning of the DRA
- Air gaps between the ground plane and DRA
- Air gaps between the DRA and shorting wall substrate
- Soldered tab to ground plane connection
- Shorting wall positioning on the DRA
- The material manufacturers' design tolerances

It is also evident that the fabricated antenna achieved a tuning range of 69% and 77% for a return loss specification of 10 dB and 6 dB respectively. This closely resembles simulation as a tuning range of 67% and 74% for a return loss specification of 10 dB and 6 dB respectively was predicted. The reconfigurable antenna also has two contiguous operating bands as shown in Figure 38. Note that the data points in Figure 38 represent operating frequencies where there is either a -6dB or -10 dB input reflection coefficient or better, as indicated. In other words it displays the tuning range of the antenna along with all operating bands that meet or exceed the specification of a 6 dB or 10 dB return loss. There are slight differences in the simulated and measured operating bands as shown in Figure 38 which can be due to any number of the reasons listed.

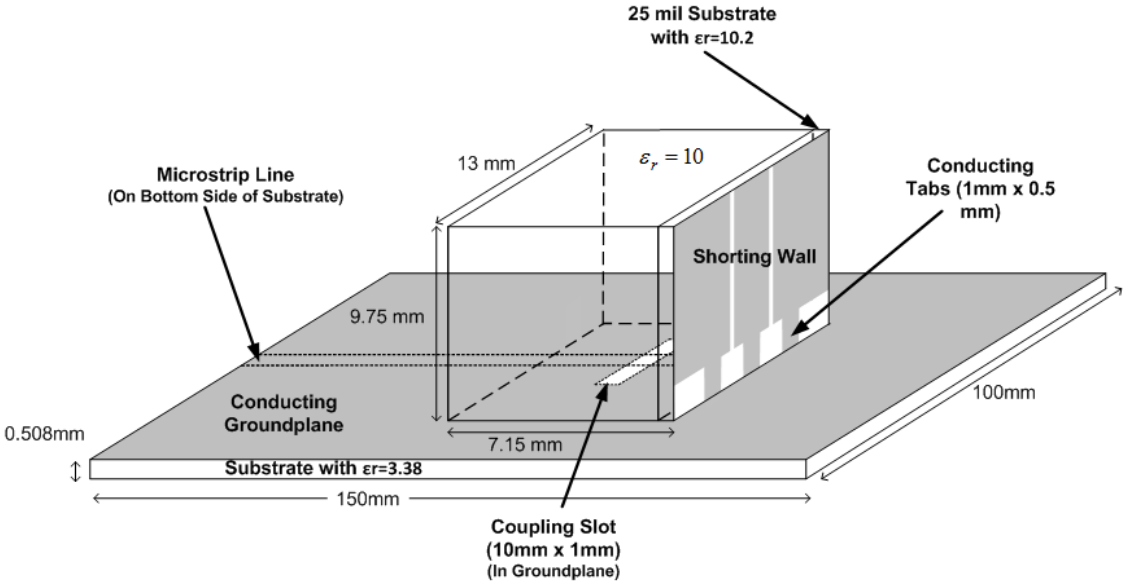

Figure 30: Single-wall Reconfigurable DRA Optimized for Tuning Range

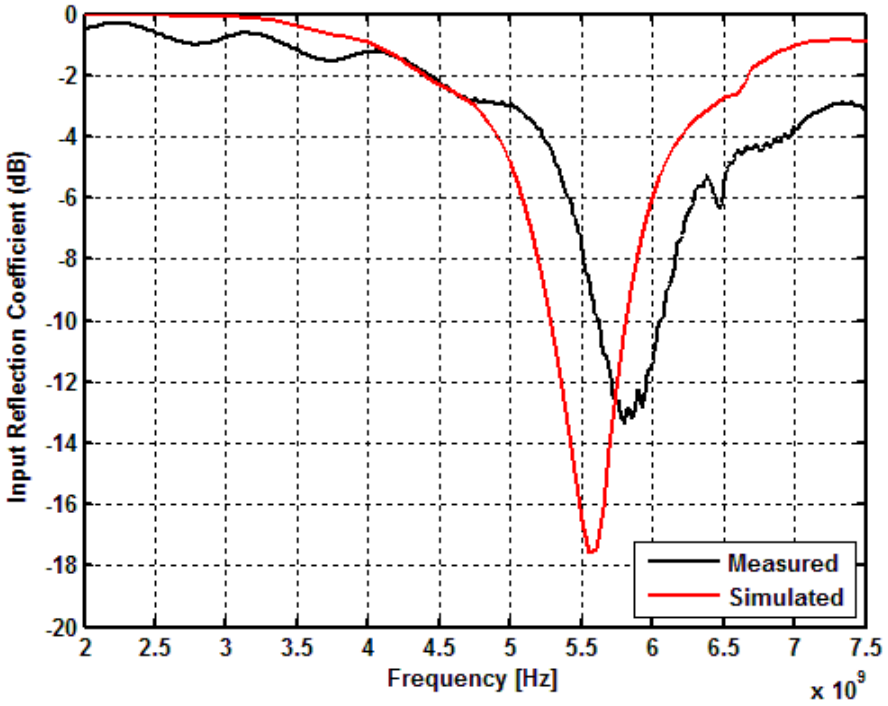

Figure 31: Frequency Response of Single-wall Reconfigurable DRA OOO Configuration

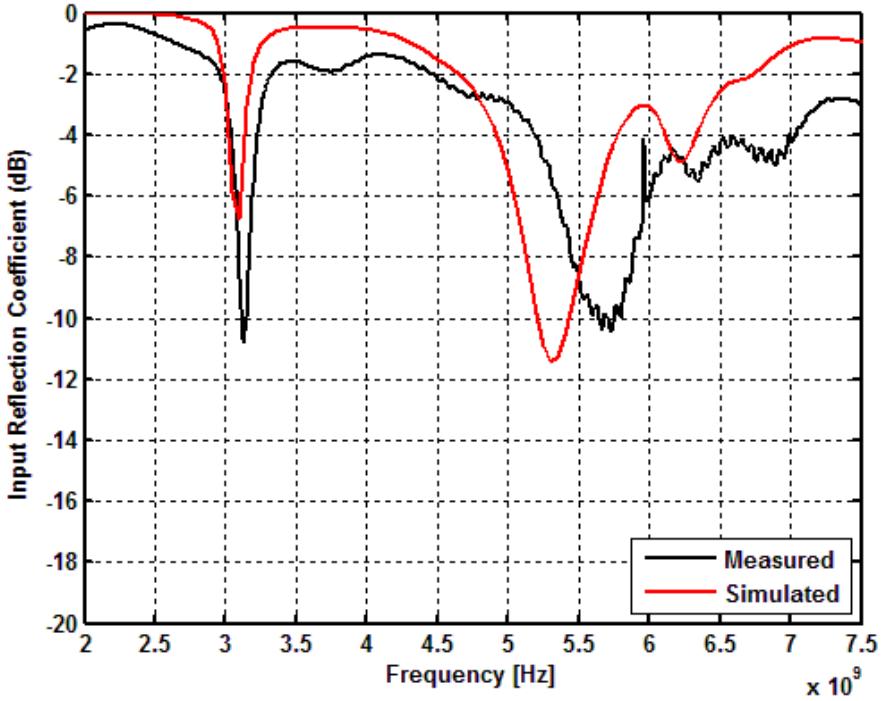

Figure 32: Frequency Response of Single-wall Reconfigurable DRA OOS Configuration

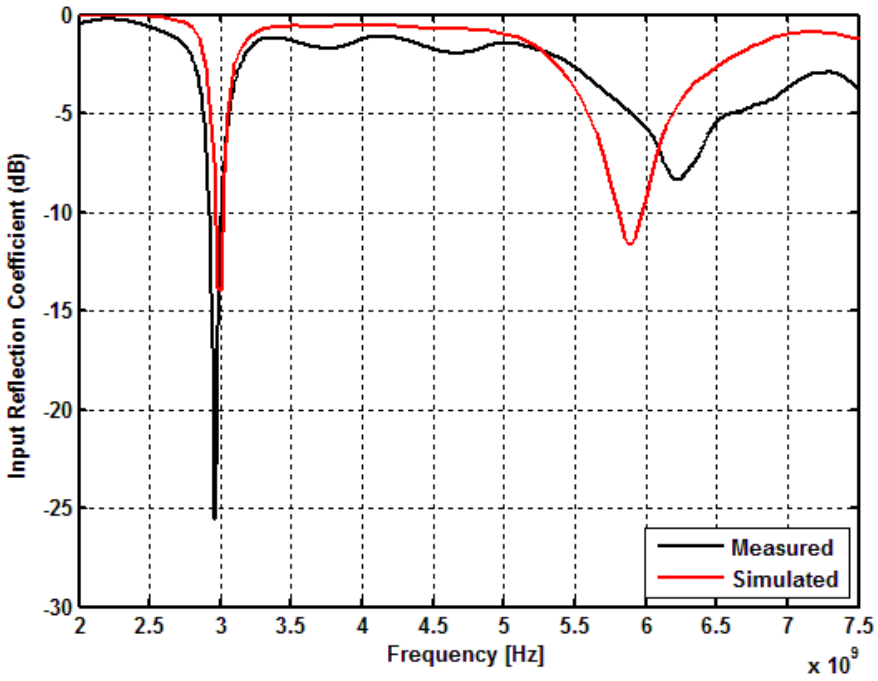

Figure 33: Frequency Response of Single-wall Reconfigurable DRA OSO Configuration

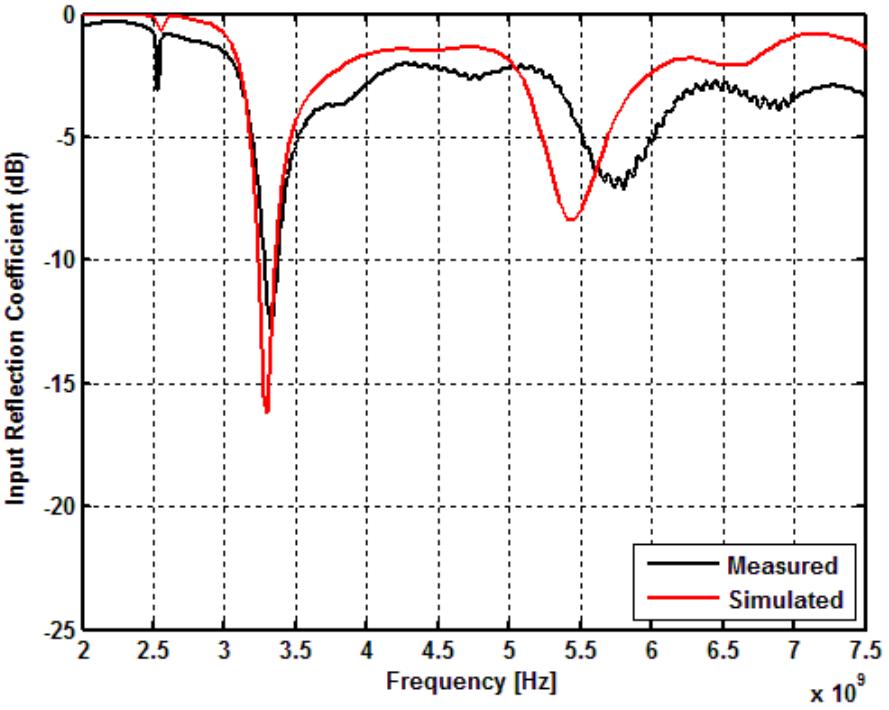

Figure 34: Frequency Response of Single-wall Reconfigurable DRA OSS Configuration

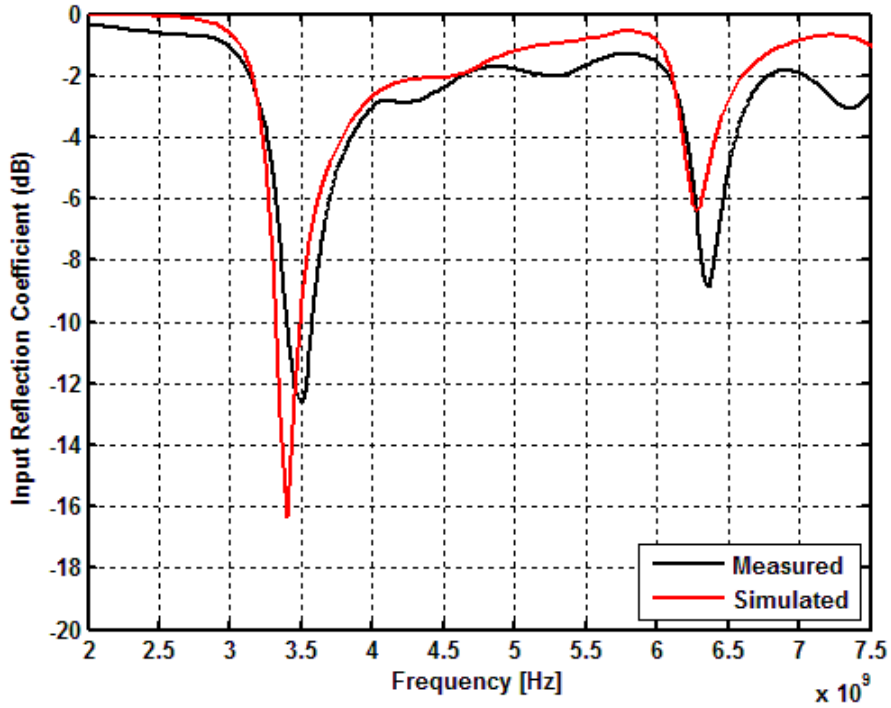

Figure 35: Frequency Response of Single-wall Reconfigurable DRA SOS Configuration

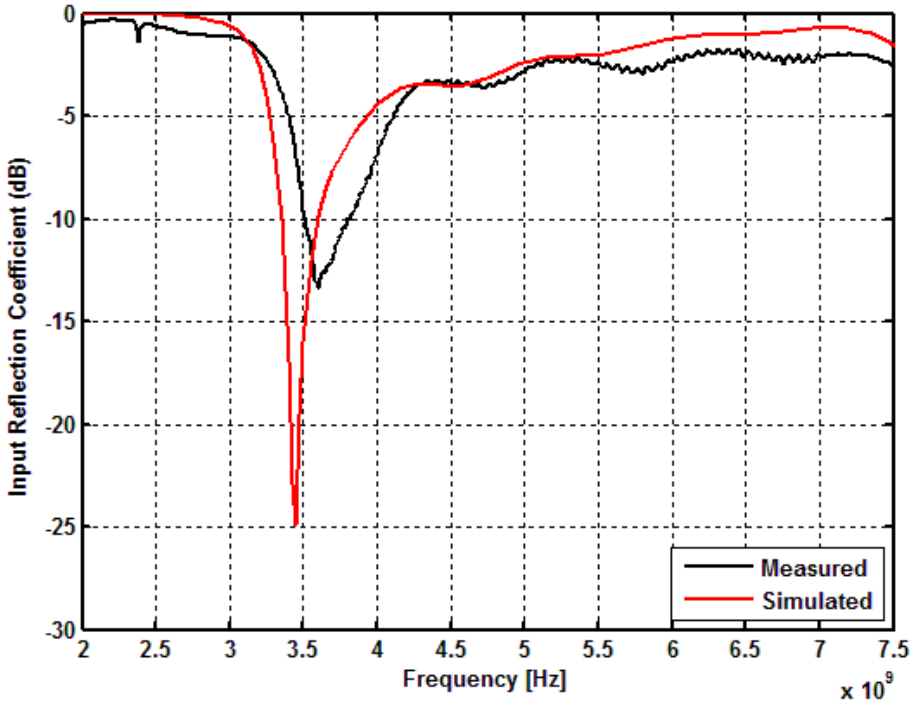

Figure 36: Frequency Response of Single-wall Reconfigurable DRA SSS Configuration

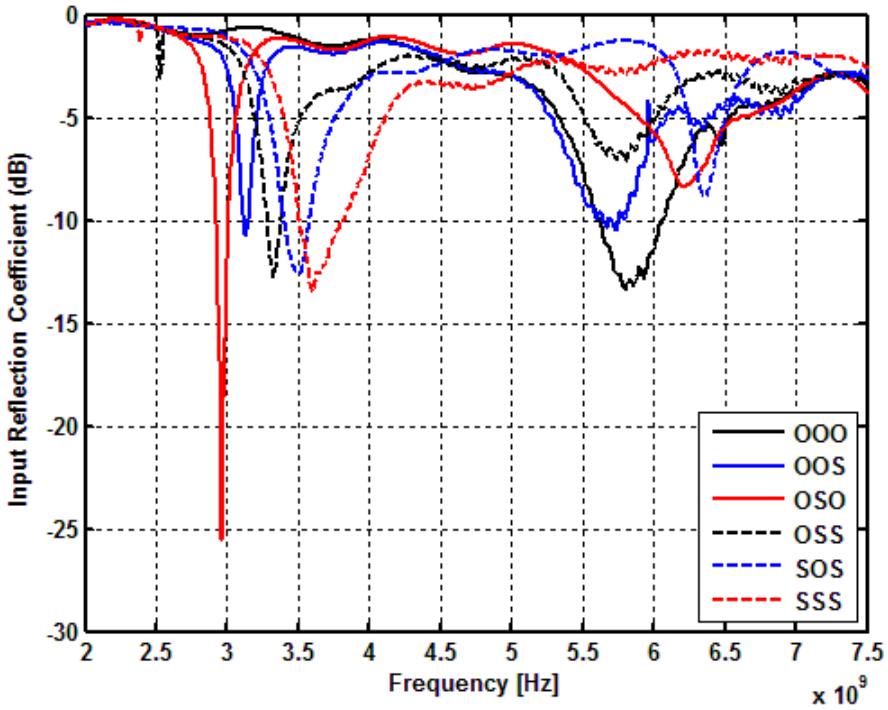

Figure 37: Summary of Frequency Response for Single-wall Reconfigurable DRA

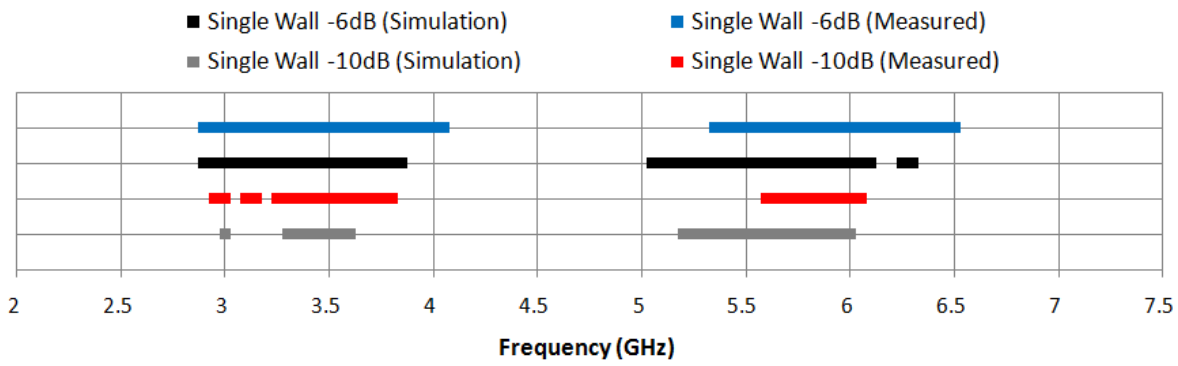

Figure 38: Tuning Range and Tuning Operating Bands for Single-wall Reconfigurable DRA

One significant observation from the simulation with regard to the operation of the single-wall reconfigurable DRA is that the antenna does not solely operate with the $TE^{x}_{\delta 11}$ mode. While the antenna does operate in the $TE^{x}_{\delta 11}$ mode in the operating band between 3 – 4 GHz, within the 5 – 6.5 GHz operating band the antenna is exciting a $TE^{x}_{\delta 13}$ mode that utilizes the shorting wall. The simulated internal electric and magnetic fields are shown in Figure 39 to Figure 42. In each case the DRA is viewed from the perspective shown in Figure 43 with the shorting wall on the right.

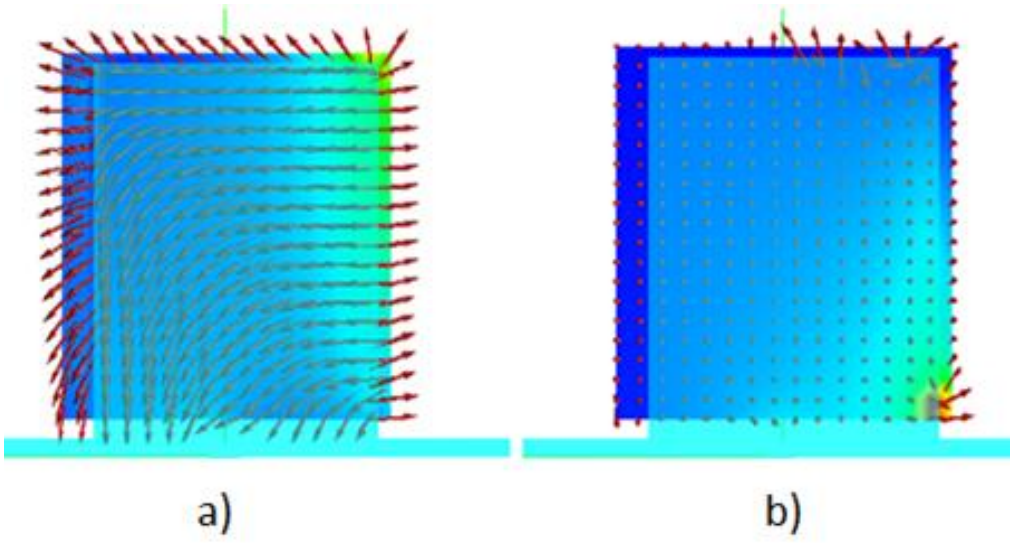

Figure 39: Simulated Electric and Magnetic Fields for the Single-wall OSO Configuration Operating at 3 GHz ($TE^{x}_{\delta 11}$ mode). a) Electric Field b) Magnetic Field

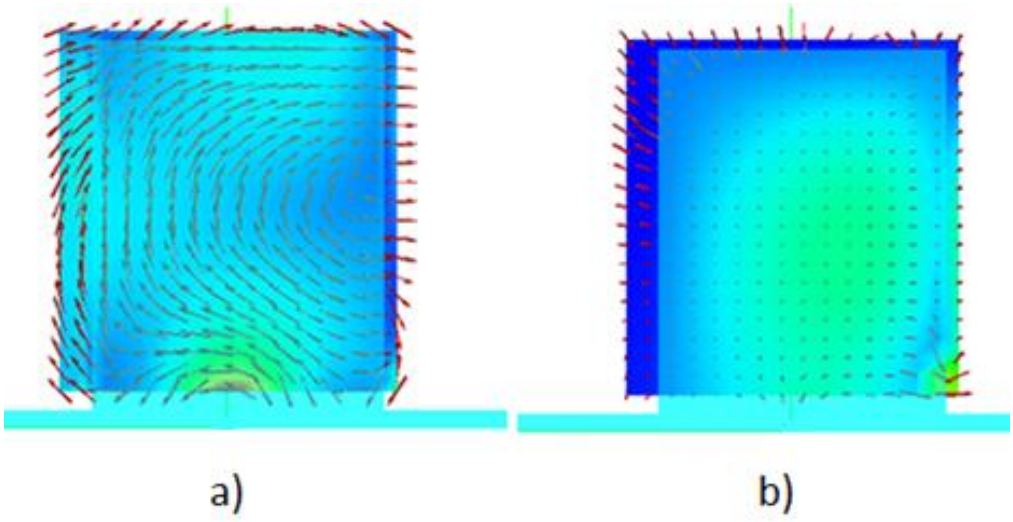

Figure 40: Simulated Electric and Magnetic Fields for the Single-wall OSO Configuration Operating at 6.2 GHz ($TE^{x}_{\delta 13}$ mode). a) Electric Field b) Magnetic Field

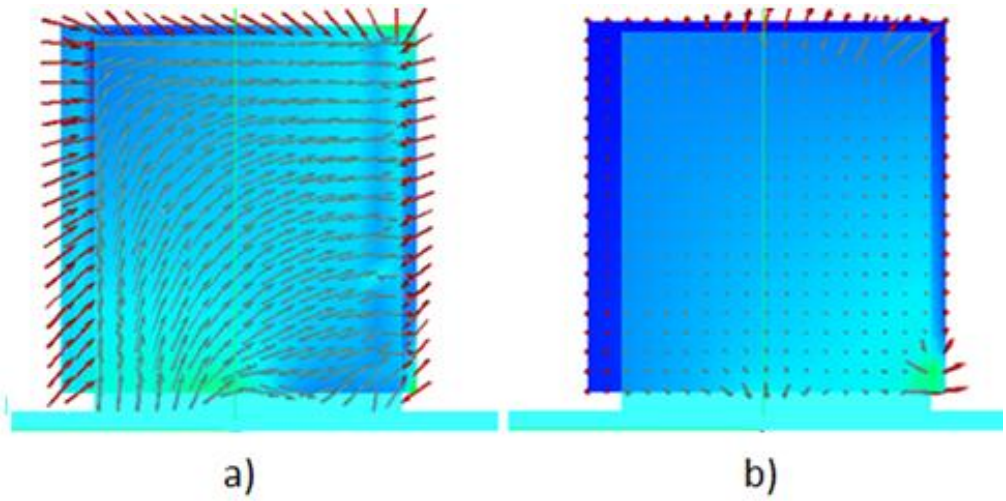

Figure 41: Simulated Electric and Magnetic Fields for the Single-wall SSS Configuration Operating at 3.5 GHz ($TE^{x}_{\delta 11}$ mode). a) Electric Field b) Magnetic Field

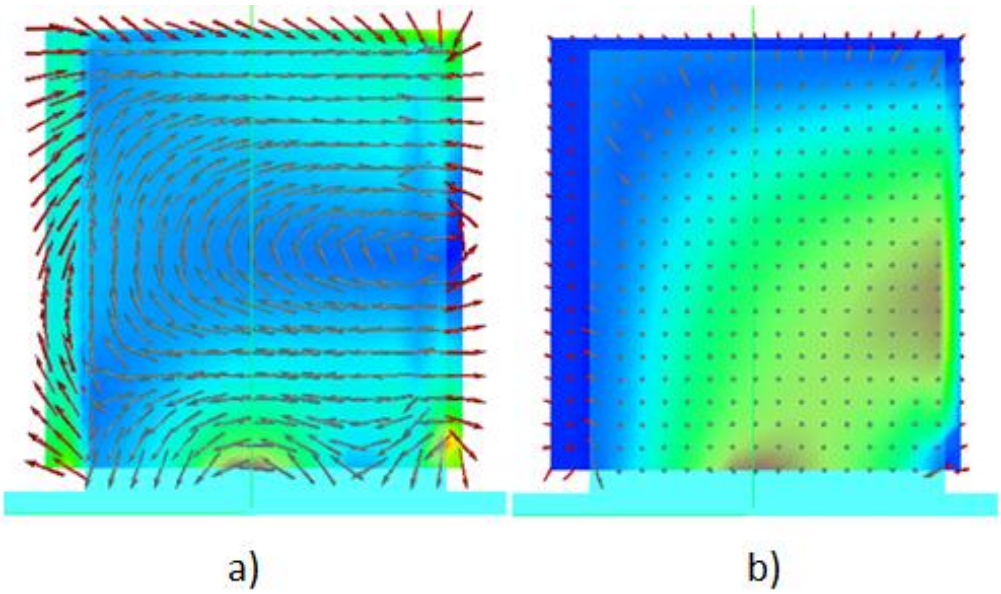

Figure 42: Simulated Electric and Magnetic Fields for the Single-wall OOO Configuration Operating at 5.8 GHz ($TE^{x}_{\delta 13}$ mode). a) Electric Field b) Magnetic Field

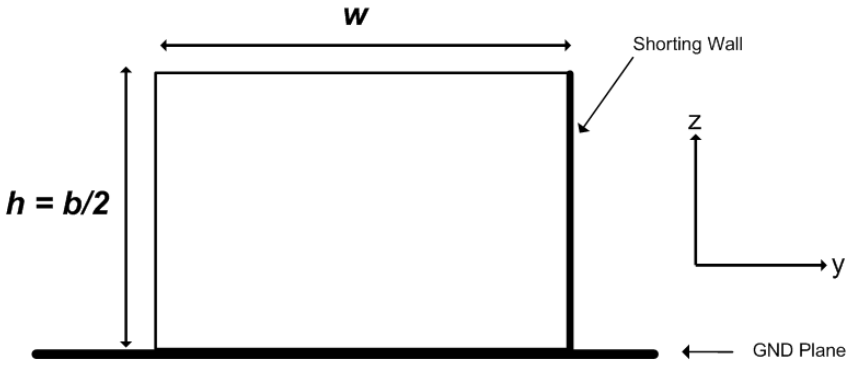

Figure 43: DRA Orientation for Figure 39 to Figure 42

The radiation patterns of the various configurations were also simulated and measured. The results of several cases are shown in Figure 44 to Figure 47. The cases shown are highly representative of the results for all configurations and at all operating frequencies. A summary for simulated and measured results is presented in Table 4 through Table 7, which show the gain of each configuration as well as the cross-polarized to co-polarized level in both the E-plane and H-plane. Due to the measurement positioner's design, the measured patterns are only obtained from -90° to 90° in the theta plane.

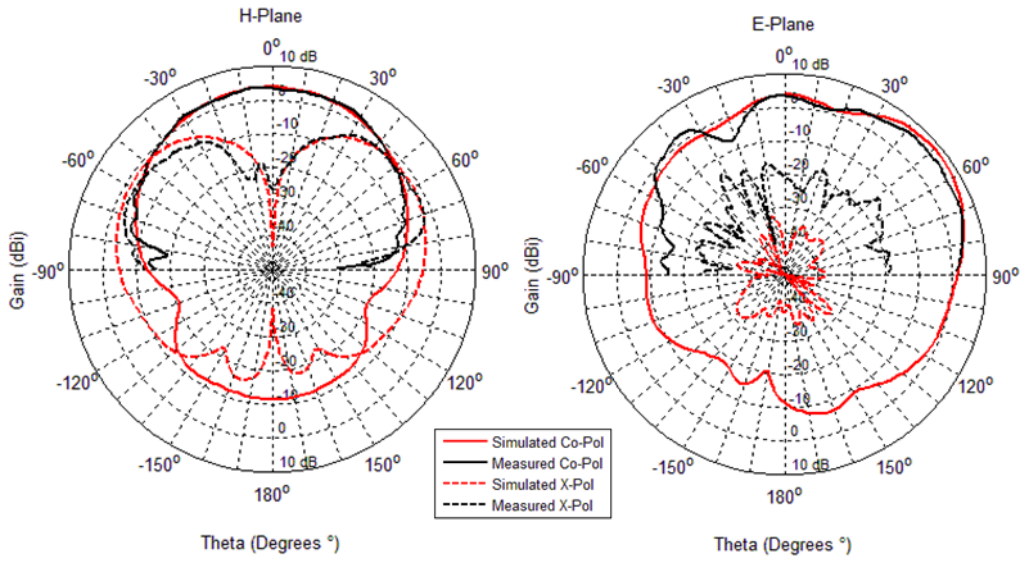

Figure 44: Measured and Simulated Gain for OOO Configuration of Single-wall Reconfigurable DRA Operating at 5.8 GHz

Table 4: Measured and Simulated Gain and Cross Polarization Levels for Single-wall OOO Configuration Operating at 5.8 GHz

	Peak Co-Pol Gain (H-Plane)	Peak Co-Pol Gain (E-Plane)	X-Pol – Co-Pol Level (H-Plane)	X-Pol – Co-Pol Level (E-Plane)
Simulated	3.89 dBi	8.42 dBi	-5.27 dB	-40.71 dB
Measured	3.71 dBi	6.42 dBi	-5.54 dB	-20.22 dB

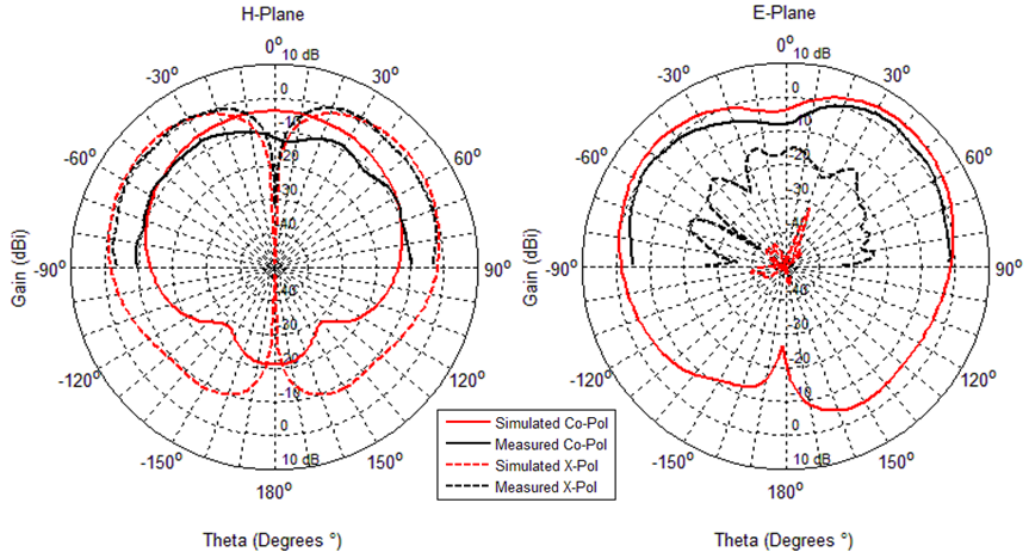

Figure 45: Measured and Simulated Gain for OSO Configuration of Single-wall Reconfigurable DRA Operating at 2.9 GHz

Table 5: Measured and Simulated Gain and Cross Polarization Levels for Single-wall OSO Configuration Operating at 2.9 GHz

	Peak Co-Pol Gain (H-Plane)	Peak Co-Pol Gain (E-Plane)	X-Pol – Co-Pol Level (H-Plane)	X-Pol – Co-Pol Level (E-Plane)
Simulated	-3.84 dBi	4.44 dBi	5.57 dB	-46.61 dB
Measured	-7.08 dBi	2.54 dBi	8.28 dB	-16.93 dB

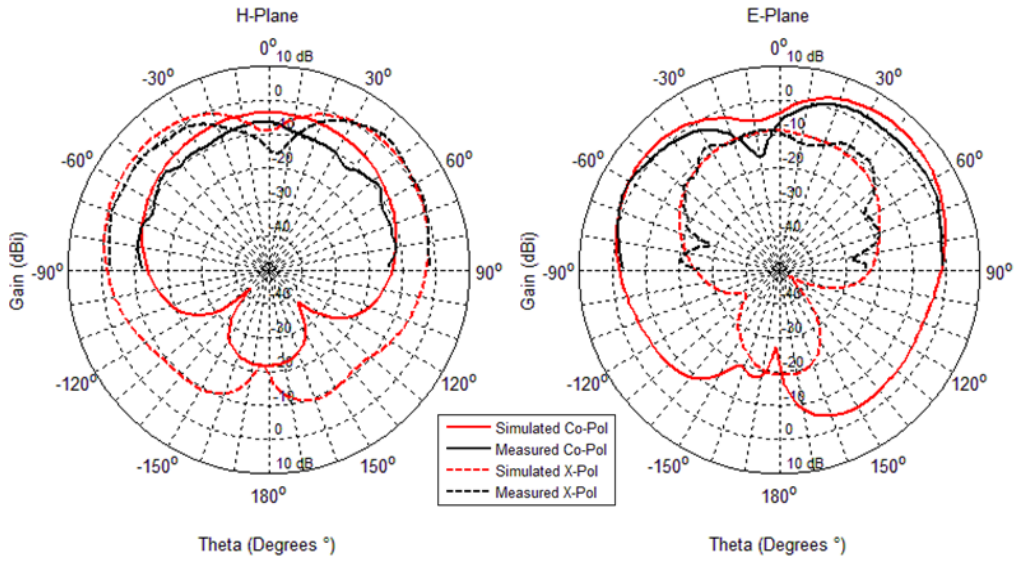

Figure 46: Measured and Simulated Gain for OSS Configuration of Single-wall Reconfigurable DRA Operating at 3.3 GHz

Table 6: Measured and Simulated Gain and Cross Polarization Levels for Single-wall OSS Configuration Operating at 3.3 GHz

	Peak Co-Pol Gain (H-Plane)	Peak Co-Pol Gain (E-Plane)	X-Pol – Co-Pol Level (H-Plane)	X-Pol – Co-Pol Level (E-Plane)
Simulated	-3.65 dBi	5.06 dBi	5.72 dB	-14.10 dB
Measured	-6.44 dBi	2.12 dBi	9.05 dB	-10.01 dB

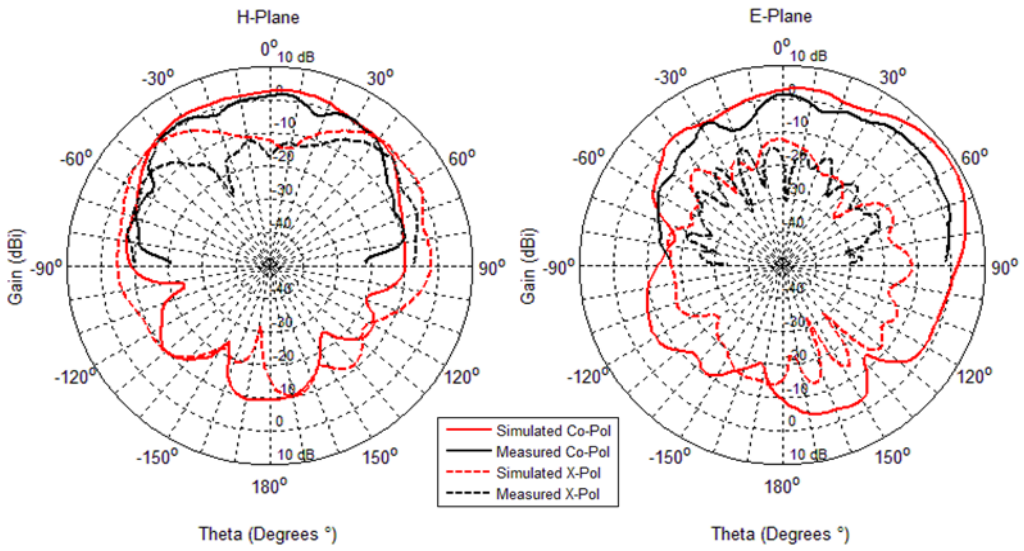

Figure 47: Measured and Simulated Gain for SOS Configuration of Single-wall Reconfigurable DRA Operating at 6.4 GHz

Table 7: Measured and Simulated Gain and Cross Polarization Levels for Single-wall SOS Configuration Operating at 6.4 GHz

	Peak Co-Pol Gain (H-Plane)	Peak Co-Pol Gain (E-Plane)	X-Pol – Co-Pol Level (H-Plane)	X-Pol – Co-Pol Level (E-Plane)
Simulated	2.91 dBi	8.47 dBi	-2.45 dB	-20.07 dB
Measured	1.58 dBi	3.28 dBi	-3.22 dB	-16.23 dB

From the far field pattern results it is again clear that there is good agreement between the simulated and measured results. However, it is also apparent that the measured co-polarized radiation pattern in the H-plane at frequencies below 4 GHz is much reduced at broadside (Figure 44 and Figure 46). This is not observed in the measured patterns for frequencies greater than 4GHz. It is also clear that there is significant gain (3 – 7 dBi) in the 4-6.5 GHz operating band. This is expected since the $TE^{x}_{\delta 13}$ mode is analogous to three stacked horizontal magnetic dipoles, which leads to a radiation pattern with greater gain than what could be obtained if the $TE^{x}_{\delta 11}$ mode were excited [7]. One prominent weakness in the design is the large cross polarization component in the H-plane that is observed in all configurations. It is also clear that the cross polarized radiated pattern in the H-plane resembles the radiation pattern of a vertical electric monopole.

In order to determine the source of the large cross polarized component in the H-plane the current distribution on the antenna was examined. A simulation showing the current distribution for the OSO configuration is shown in Figure 48. It is clear from Figure 48 that there are large currents travelling vertically along the edges of the shorting wall. Although there are also large currents travelling along the 300µm bias gaps, they travel in opposite directions on either side of each bias gap and so they do not have a significant contribution to the cross polarized field, unlike the currents on the edges. Such a current distribution is analogous to an electric monopole which is likely the source of the large cross polarized radiated field in the H-plane. This issue is addressed in Section 3.3. Finally, Figure 49 contains a photograph of the fabricated antenna (OSO configuration).

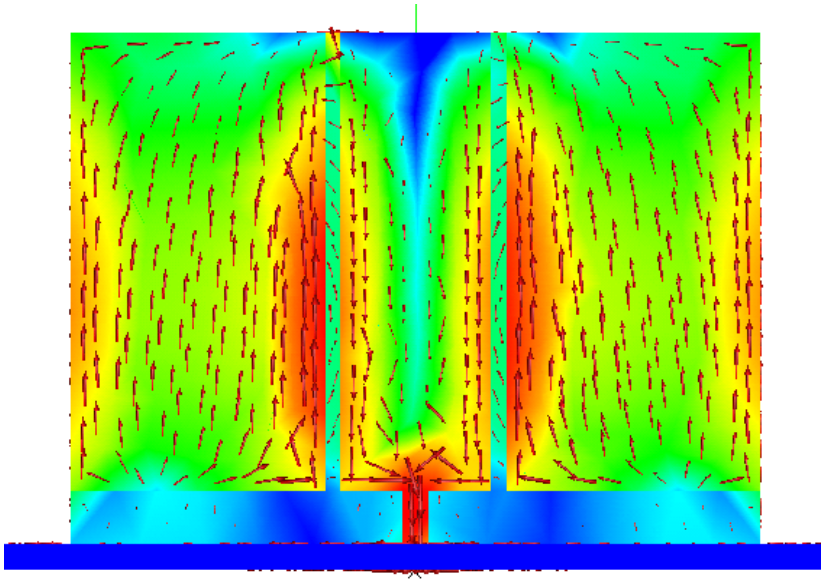

Figure 48: Electrical Currents on the Shorting Wall for the OSO Configuration Operating at 5.8 GHz. This Shows a View of the DRA Face with the Conducting Wall

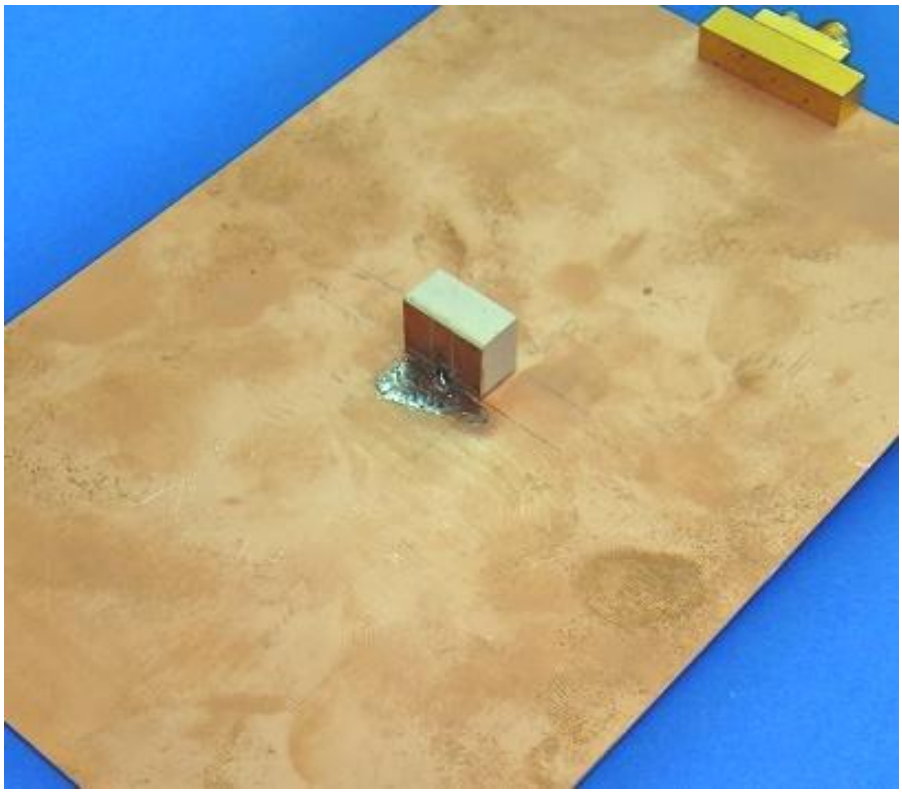

Figure 49: Fabricated Single-wall Reconfigurable DRA Optimized for Tuning Range

3.3 Reconfigurable DRA with Dual Shorting Walls

As mentioned in Section 3.2.4, a large cross polarization component in the H-plane was observed in all configurations of the single-wall reconfigurable DRA. In this section the cross polarization level will be addressed with a targeted goal of obtaining a maximum cross polarization to co-polarization level of -10 dB. In Section 3.2.4 it was shown that the currents running along the edges of the shorting walls were the cause of the unwanted radiation.

One method that the present author attempted to address this issue was to place horizontal gaps at the midpoint of the shorting wall (Figure 50) in an attempt at disrupting the currents. However, the slotted shorting wall did not effectively reduce the currents, while adversely affecting the antennas performance.

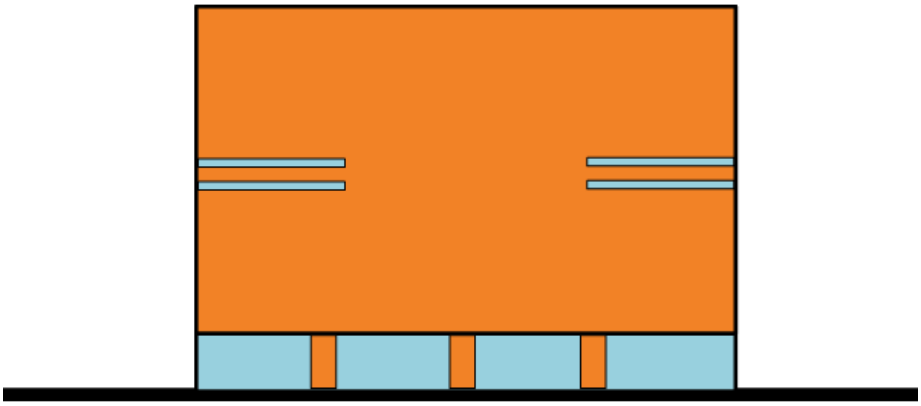

Figure 50: Slots Used to Reduce Cross Polarization Component by Altering Currents on the Shorting Wall Edge

A second method to reduce the cross polarization component is to place a second shorting wall on the other side of the DRA, as shown in Figure 51. The conjecture is that the currents will be of equal magnitude but in opposite directions on the second shorting wall and so the fields due to the edge currents on the two walls should effectively cancel since the walls are electrically close together ($w < 0.2\lambda$). The technique was applied and simulations were performed using HFSS and FEKO, which demonstrated the effectiveness of the method. Although there are now six "switches", each side will be switched in pairs, and so there are still only six unique configurations. After performing several simulations an optimized geometry was obtained which, is discussed in Section 3.3.1.

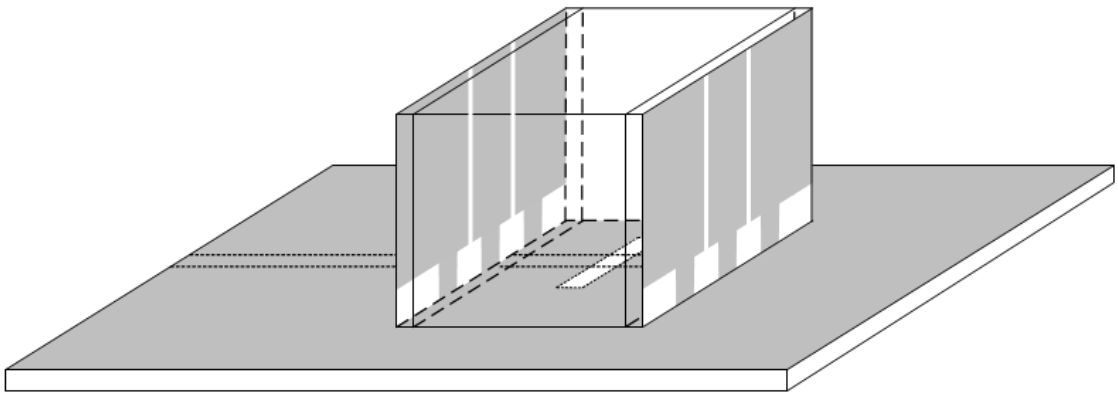

Figure 51: Dual-Wall Reconfigurable DRA to Reduce Cross Polarization Levels

3.3.1 Optimum Design for Tuning Range and Cross-Polarization Performance

As previously mentioned, an antenna geometry was obtained (via simulation trade-off studies) that had an optimal tuning range, frequency response, radiation pattern, and most importantly, addressed the cross polarization issue that plagued the single shorting wall design. A DRA of dimension 12mm × 12mm × 8mm for $w \times d \times h$ and a dielectric constant of ten was chosen. The design was first simulated with and without the shorting walls in order to estimate the tuning range and to verify the resonant mode types. Since the DRA now has shorting walls on both sides, and a ground plane, the electric field must be perpendicular to the three surfaces. It is likely that the $TE^{x}_{\delta 01}$ mode will be excited when the two shorting walls are present [6]. Simulation with HFSS and FEKO verified this assumption, and the electric fields within the DRA are shown in Figure 52 for the case with two shorting walls. Using equation (2.4.1) with m=0 and n=1 gave a resonant frequency of 3.7 GHz while simulation predicted a resonant frequency of 3.3 GHz, the difference is likely due to the loading effect of the slot that is not accounted for in the transcendental equation (2.4.1). Of course when no shorting walls are present the DRA operates in the $TE^{x}_{\delta 11}$ mode. Using equation (2.4.1) with m=1 and n=1 gave a resonant frequency of 5.6 GHz, while simulation predicted a resonant frequency of 5.8 GHz. The above sets of results represent a tuning range of 55%, which can likely to be improved on by making use of frequency shifts induced by the tabs.

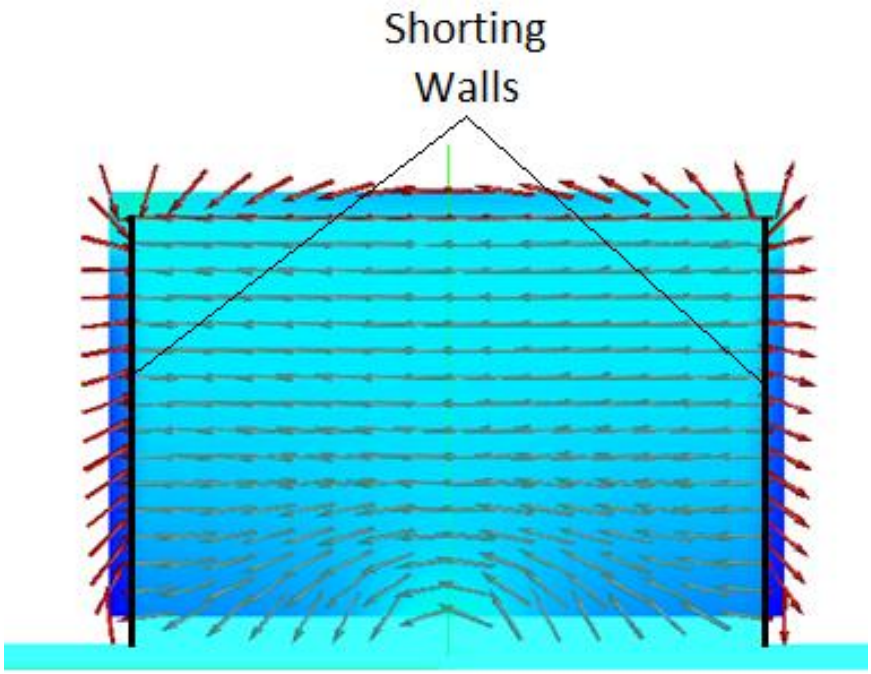

Figure 52: Simulated Electric Field for DRA with Two Shorting Walls operating at 3.3 GHz ($TE^{x}_{\delta 01}$ mode)

The tab width was again selected to be 0.5 mm since this value best represents the package size of the switching devices that will be used in Chapters 4 and 5. As in Section 3.2.4, the shorting wall was designed with 300µm vertical bias gaps in order to facilitate the eventual need for the separation of bias voltages. The shorting walls and tab configurations were again printed using an etching process on 25 mil Rogers 6010 substrate that had a dielectric constant of 10.2. Since the shorting walls substrate had a thickness of 25 mils (0.635 mm) the DRA was fabricated to have a width of only 10.73 mm so that the total width would be 12 mm. A ground plane of 150 mm by 100 mm was used with an aperture of length 10mm and width 1mm centered about the ground plane. The substrate which contains the ground plane had a thickness of 0.508mm and a dielectric constant of 3.38. The aperture is coupled via a microstrip line of width 1.18 mm and length 81 mm that has a characteristic impedance of 50Ω. The microstrip line extends 6 mm past the aperture which behaves like an open-circuit stub. The length of the stub is selected so that the imaginary component of the slot admittance is reduced, resulting in an improved impedance match to the microstrip line. The DRA, complete with shorting wall, was then bonded to the ground plane and, depending on the configuration, the tabs were soldered to the ground plane in order to ensure a good electrical connection. The dual-wall reconfigurable DRA is shown in Figure 53, along with applicable dimensions.

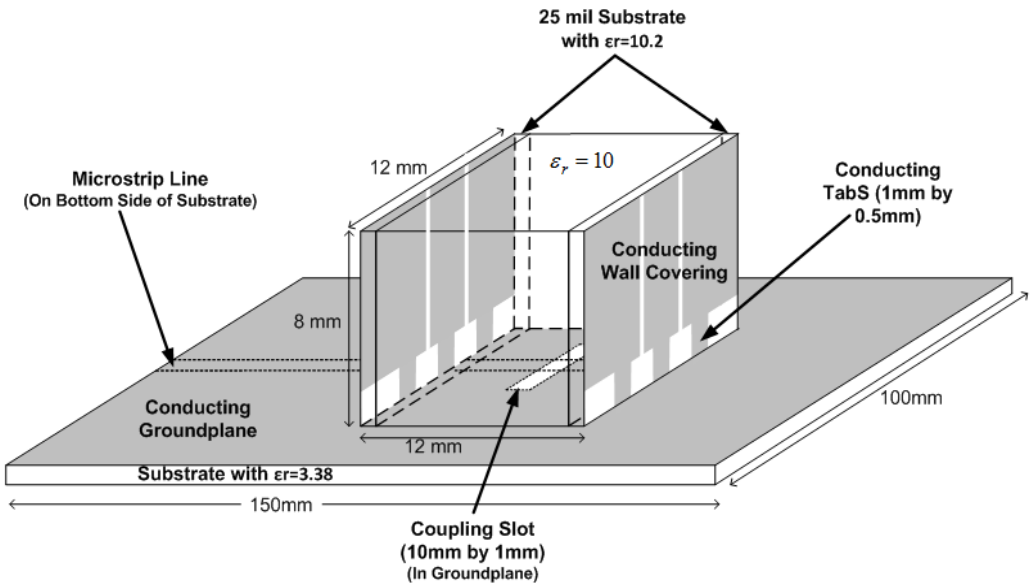

Figure 53: Dual-wall Reconfigurable DRA

Since the tabs on either side of the DRA are switched as pairs there are still six different shorting wall configurations. Therefore, six separate antennas had to be constructed. Once the antennas were fabricated the input reflection coefficient was measured and compared to simulation using HFSS. The results are shown in Figure 54 to Figure 59 with a summary in Figure 60. It is clear from the results that the simulation was fairly accurate as there is very good correlation between simulated and measured results. It is also evident that the fabricated antenna achieved a tuning range of 83% and 87% for a return loss specification of 10 dB and 6 dB respectively. This closely resembles the predicted tuning range obtained via simulation, which was determined to be 84% and 92% for a return loss specification of 10 dB and 6 dB respectively. The reconfigurable antenna also has several operating bands as shown in Figure 61. The data points in Figure 61 represent operating frequencies where there is either a -6dB or -10 dB input reflection or better, as indicated. In other words it displays the tuning range of the antenna along with all tuning operating bands that meet or exceed the specification of a 6 dB or 10 dB return loss. It is clear that the dual-wall reconfigurable DRA exceeded expectations in terms of tuning range performance as it outperforms the single-wall configuration. The dual-wall antenna has obtained a tuning range performance on par with the largest tuning range levels obtained using switching mechanisms with other antenna types in recent years while simultaneously reducing the cross polarization level, as we will see later in the section.

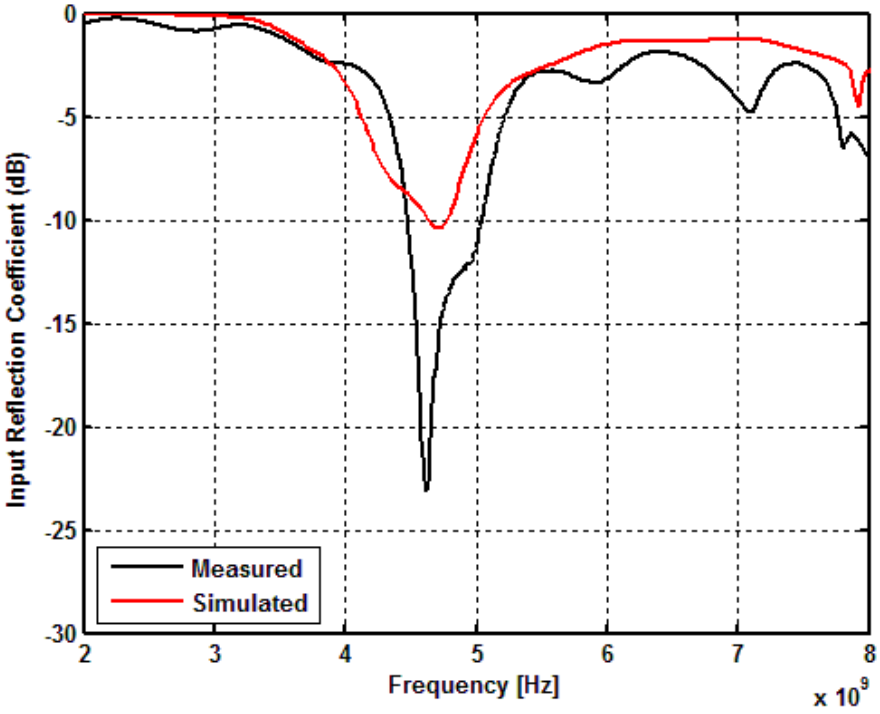

Figure 54: Frequency Response of Dual-wall Reconfigurable DRA OOO Configuration

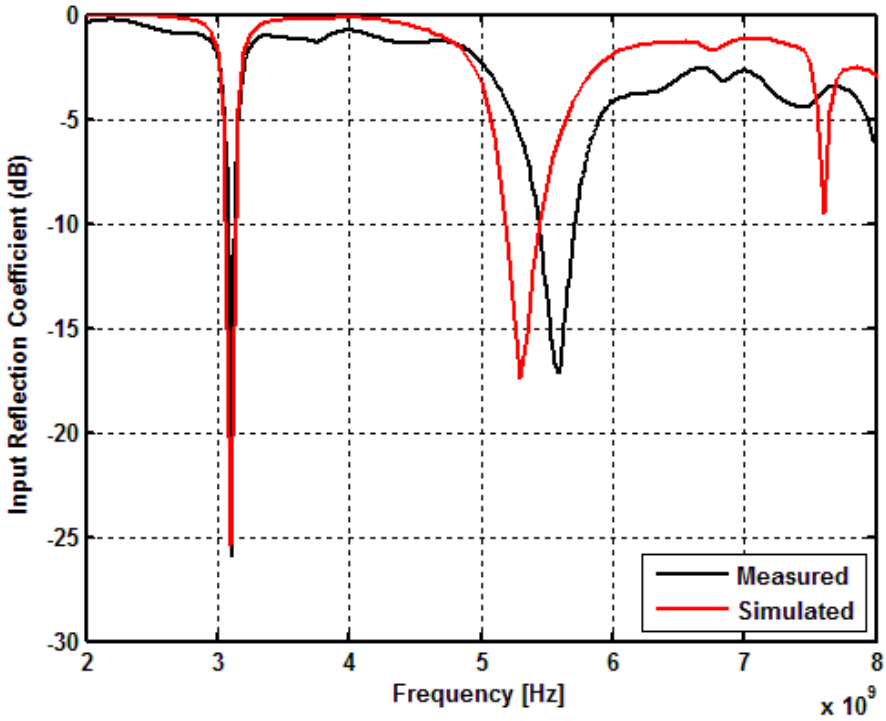

Figure 55: Frequency Response of Dual-wall Reconfigurable DRA OOS Configuration

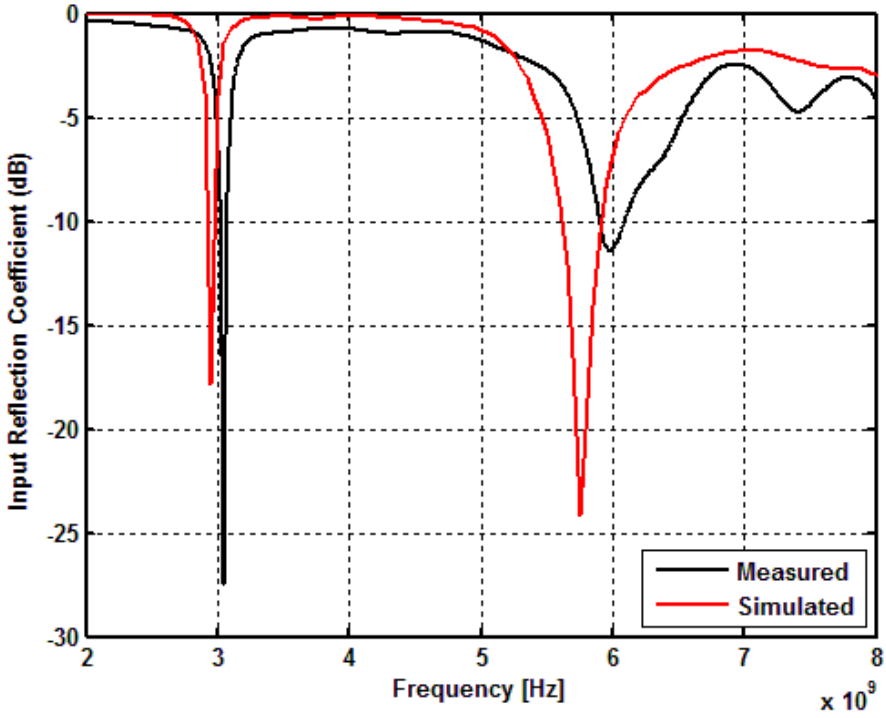

Figure 56: Frequency Response of Dual-wall Reconfigurable DRA OSO Configuration

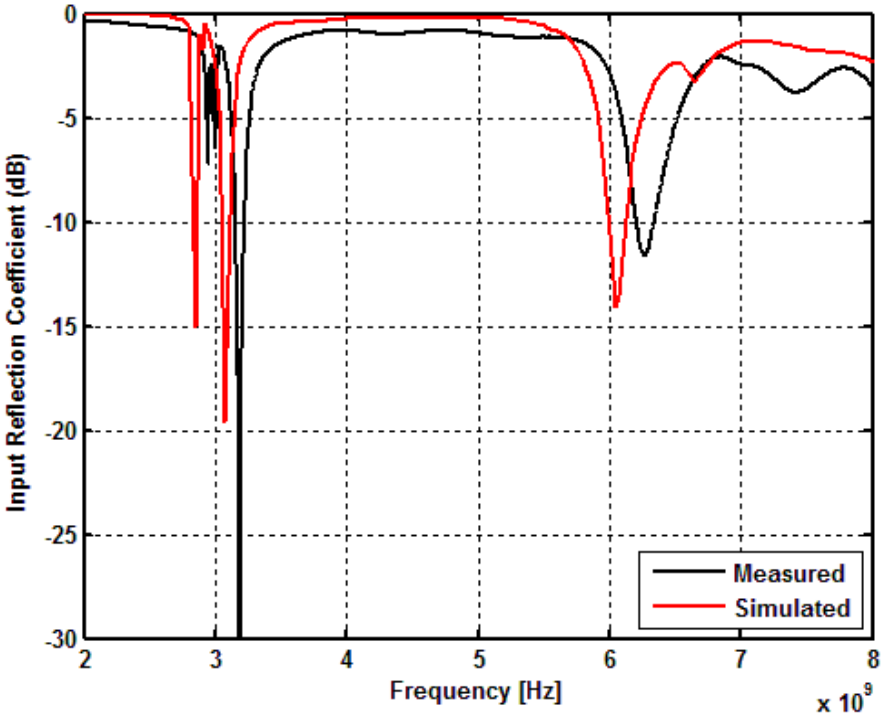

Figure 57: Frequency Response of Dual-wall Reconfigurable DRA OSS Configuration

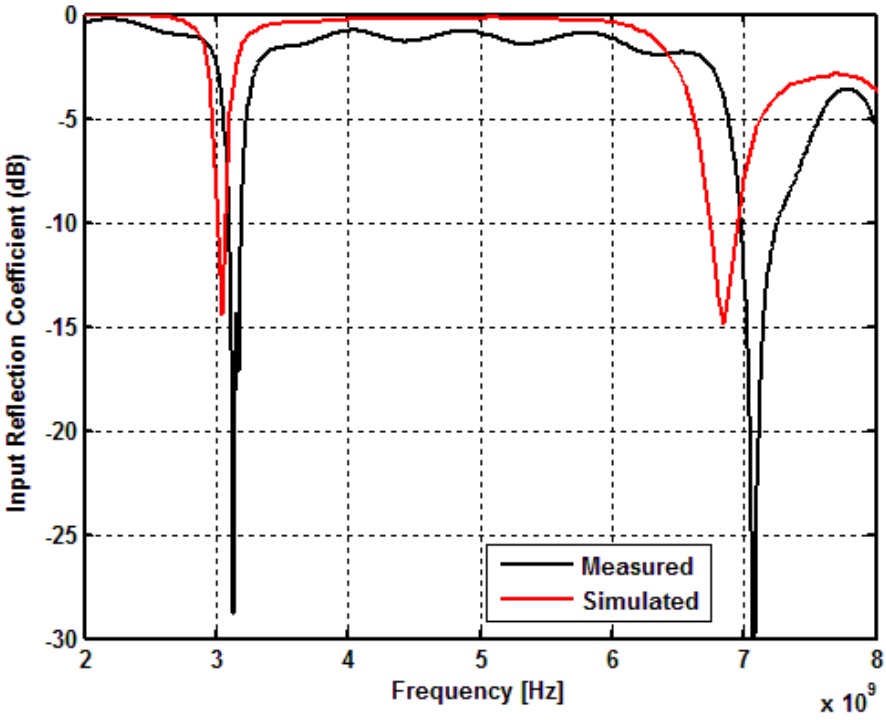

Figure 58: Frequency Response of Dual-wall Reconfigurable DRA SOS Configuration

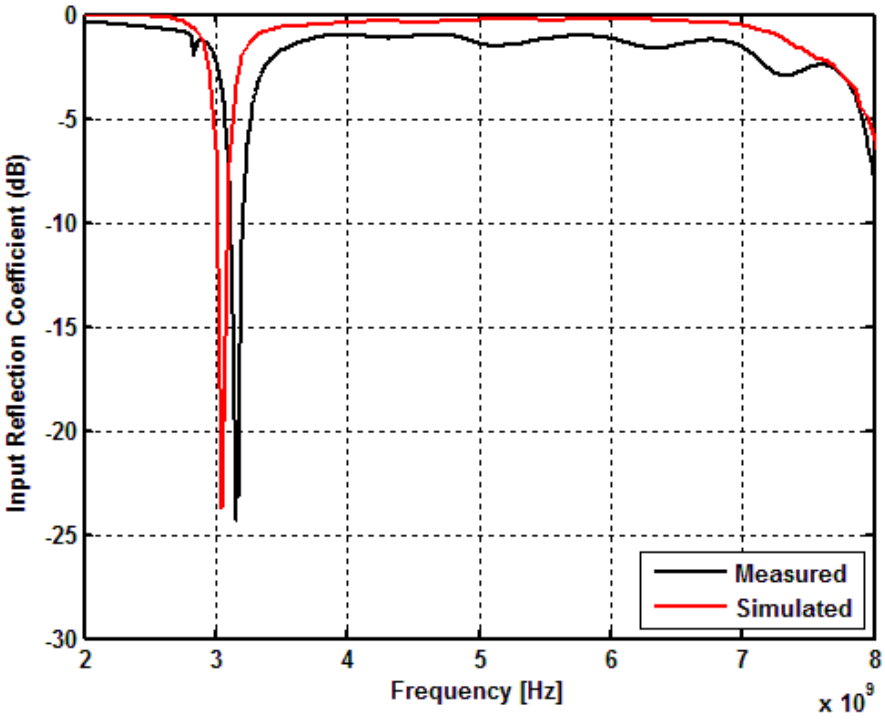

Figure 59: Frequency Response of Dual-wall Reconfigurable DRA SSS Configuration

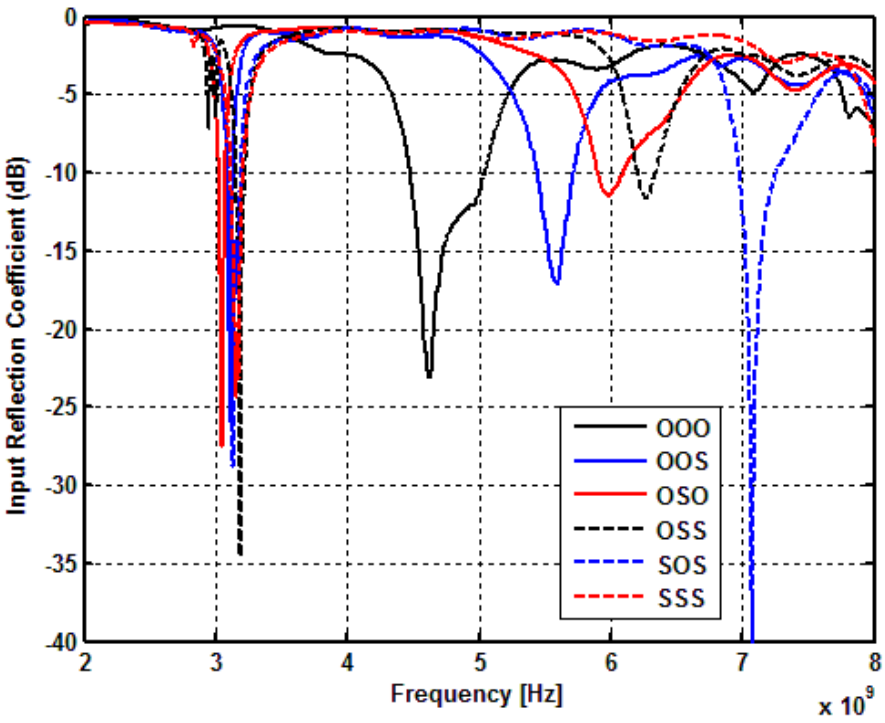

Figure 60: Summary of Frequency Response for Dual-wall Reconfigurable DRA

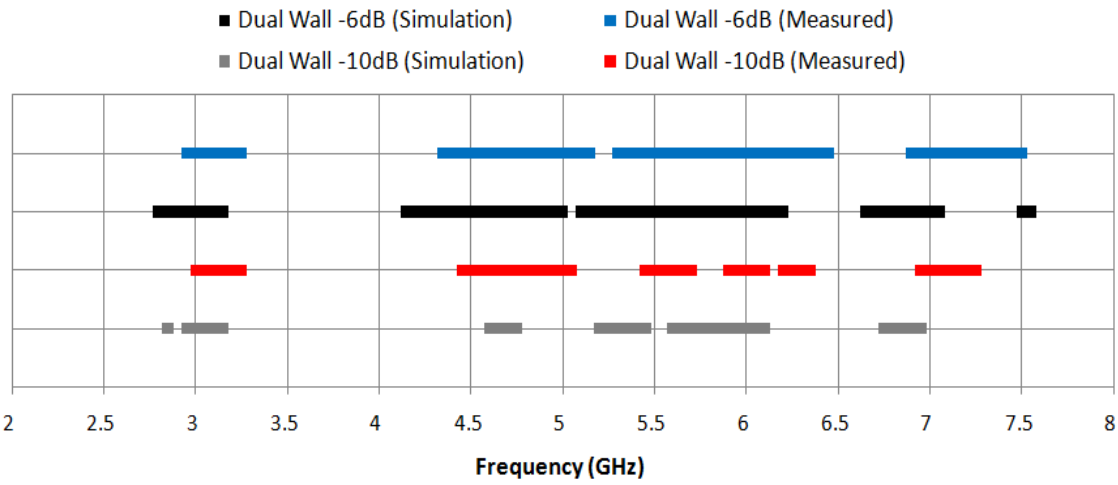

Figure 61: Tuning Range and Tuning Operating Bands for Dual-wall Reconfigurable DRA

As shown in Figure 54 to Figure 59 the dual-wall DRA achieves dual band performance by making use of the $TE^{x}_{\delta 01}$ mode at the low frequencies (~ 3GHz) and the $TE^{x}_{\delta 11}$ mode at all other frequencies. The simulated internal electric and magnetic fields are shown in Figure 62 to Figure 65. In each case the DRA is viewed from the perspective shown in Figure 66 with the shorting walls on the left and right side. It is clear from the internal electric and magnetic fields that only the $TE^{x}_{\delta 01}$ mode and the $TE^{x}_{\delta 11}$ mode are utilized.

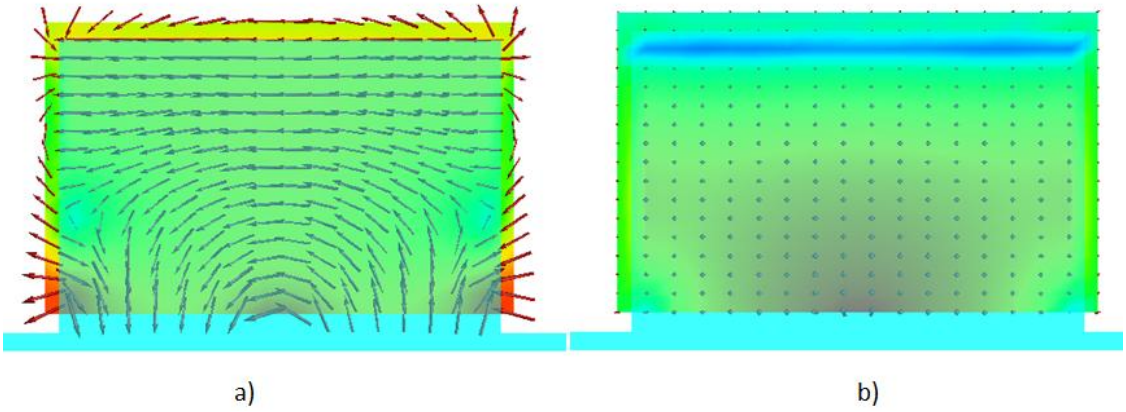

Figure 62: Simulated Electric and Magnetic Fields for the Dual-wall OOO Configuration Operating at 4.65 GHz ($TE^{x}_{\delta 11}$ mode). a) Electric Field b) Magnetic Field

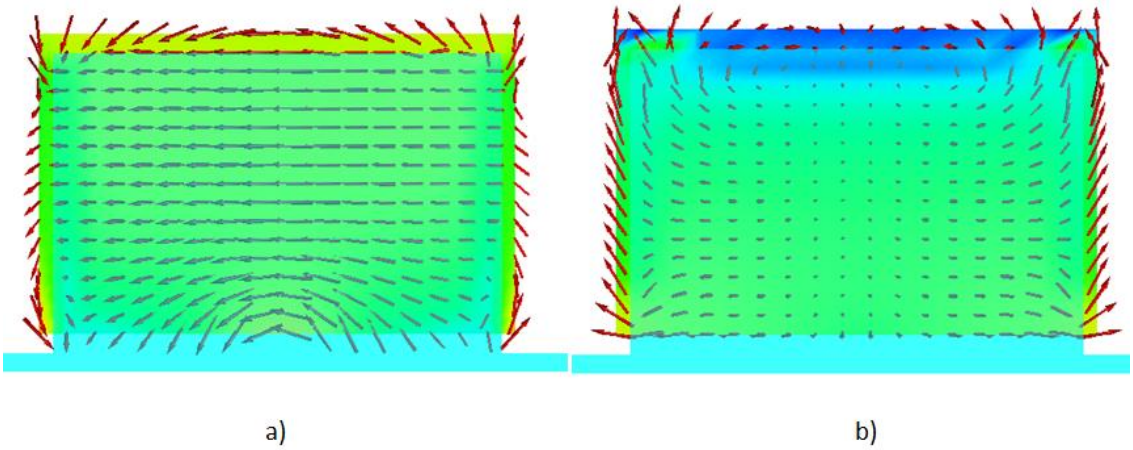

Figure 63: Simulated Electric and Magnetic Fields for the Dual-wall OOS Configuration Operating at 3.1 GHz ($TE^{x}_{\delta 01}$ mode). a) Electric Field b) Magnetic Field

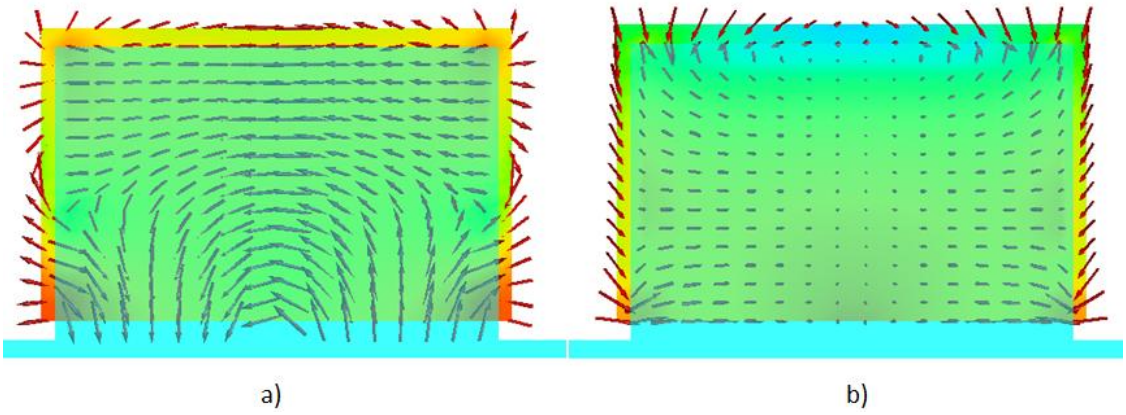

Figure 64: Simulated Electric and Magnetic Fields for the Dual-wall OOS Configuration Operating at 5.65 GHz ($TE^{x}_{\delta 11}$ mode). a) Electric Field b) Magnetic Field

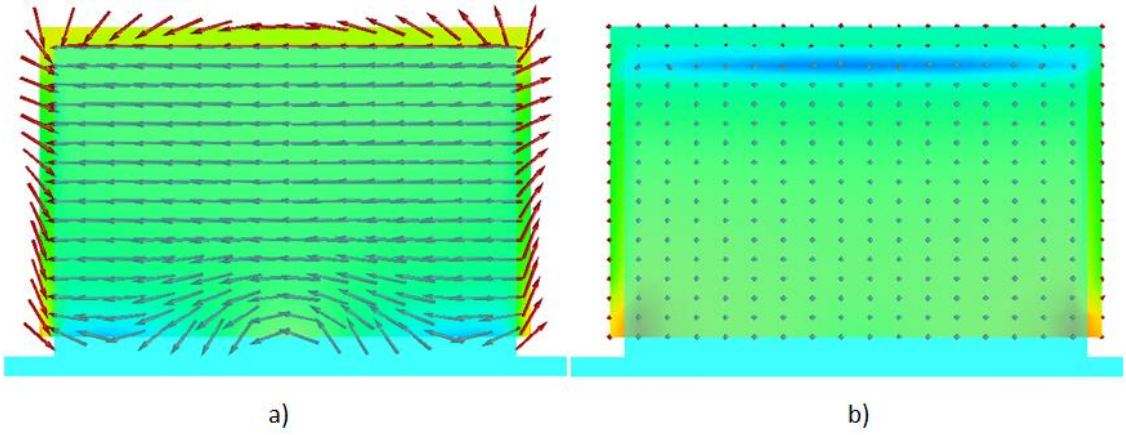

Figure 65: Simulated Electric and Magnetic Fields for the Dual-wall SSS Configuration Operating at 3.1 GHz ($TE^{x}_{\delta 01}$ mode). a) Electric Field b) Magnetic Field

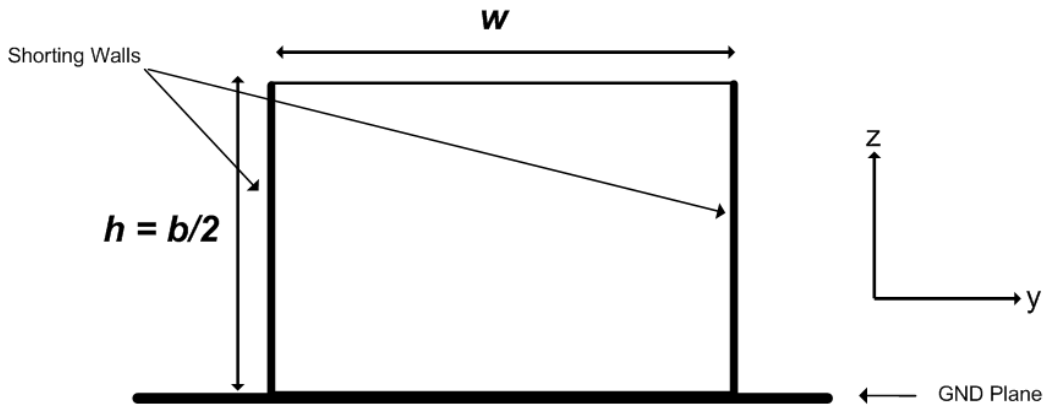

Figure 66: DRA Orientation for Figure 62 to Figure 65

The radiation patterns of the various configurations were also simulated and measured. The results of several cases are shown in Figure 67 through Figure 71. The cases shown are highly representative of the results for all configurations and at all resonant frequencies. A summary for simulated and measured results is given in Table 8 through to Table 12, which shows the gain of each configuration as well as the cross-polarized to co-polarized level in both the E-plane and H-plane.

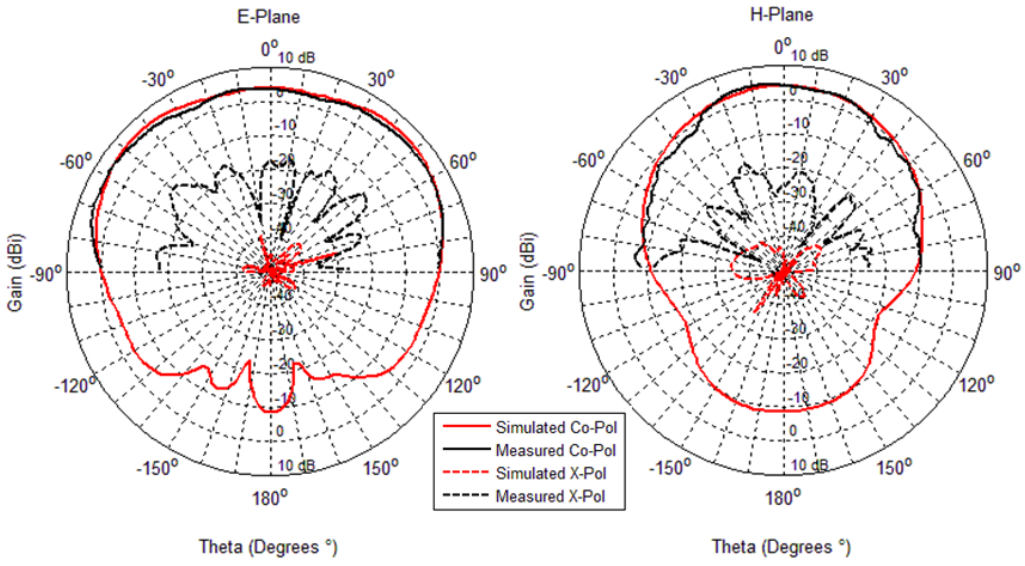

Figure 67: Measured and Simulated Gain for OOO Configuration of Dual-wall Reconfigurable DRA Operating at 4.65 GHz

Table 8: Measured and Simulated Gain and Cross Polarization Levels for Dual-wall OOO Configuration Operating at 4.65 GHz

	Peak Co-Pol Gain (H-Plane)	Peak Co-Pol Gain (E-Plane)	X-Pol – Co-Pol Level (H-Plane)	X-Pol – Co-Pol Level (E-Plane)
Simulated	4.02 dBi	6.38 dBi	-38.78 dB	-44.65 dB
Measured	4.68 dBi	5.72 dBi	-16.92 dB	-18.14 dB

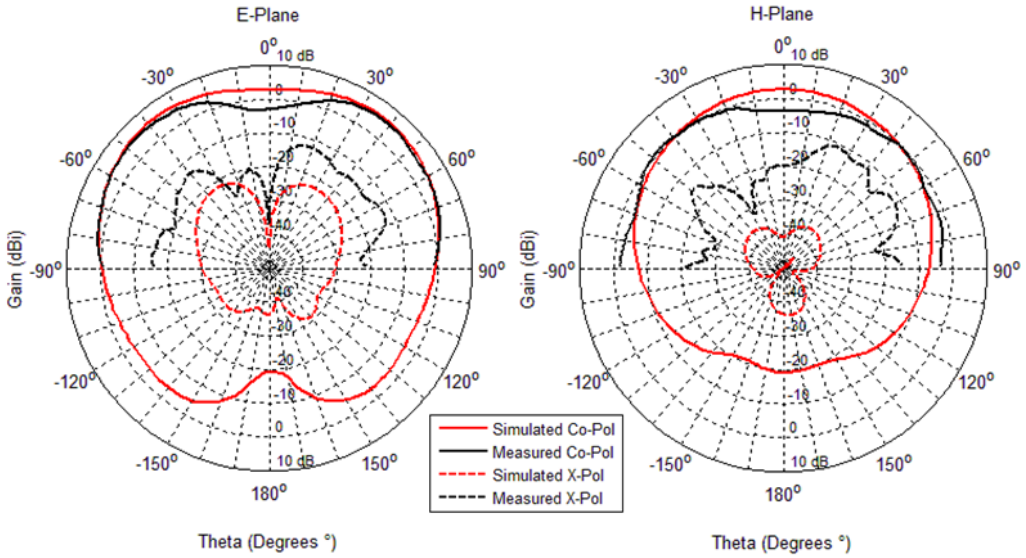

Figure 68: Measured and Simulated Gain for OOS Configuration of Dual-wall Reconfigurable DRA Operating at 3.1 GHz

Table 9: Measured and Simulated Gain and Cross Polarization Levels for Dual-wall OOS Configuration Operating at 3.1 GHz

	Peak Co-Pol Gain (H-Plane)	Peak Co-Pol Gain (E-Plane)	X-Pol – Co-Pol Level (H-Plane)	X-Pol – Co-Pol Level (E-Plane)
Simulated	2.63 dBi	5.90 dBi	-38.38 dB	-27.45 dB
Measured	0.70 dBi	5.31 dBi	-11.66 dB	-17.53 dB

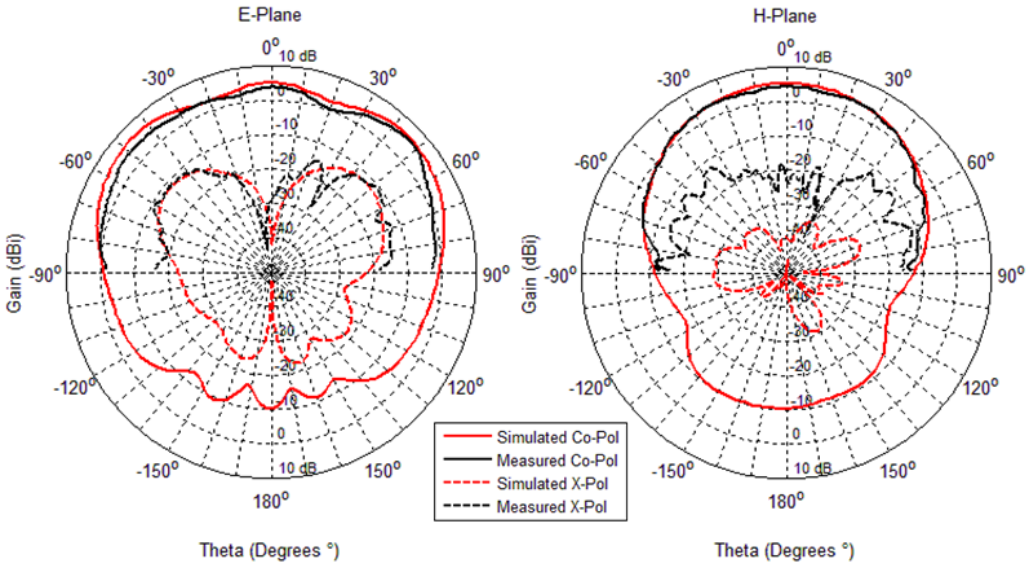

Figure 69: Measured and Simulated Gain for OOS Configuration of Dual-wall Reconfigurable DRA Operating at 5.65 GHz

Table 10: Measured and Simulated Gain and Cross Polarization Levels for Dual-wall OOS Configuration Operating at 5.65 GHz

	Peak Co-Pol Gain (H-Plane)	Peak Co-Pol Gain (E-Plane)	X-Pol – Co-Pol Level (H-Plane)	X-Pol – Co-Pol Level (E-Plane)
Simulated	5.28 dBi	6.40 dBi	-32.28 dB	-18.10 dB
Measured	4.43 dBi	5.66 dBi	-15.75 dB	-16.21 dB

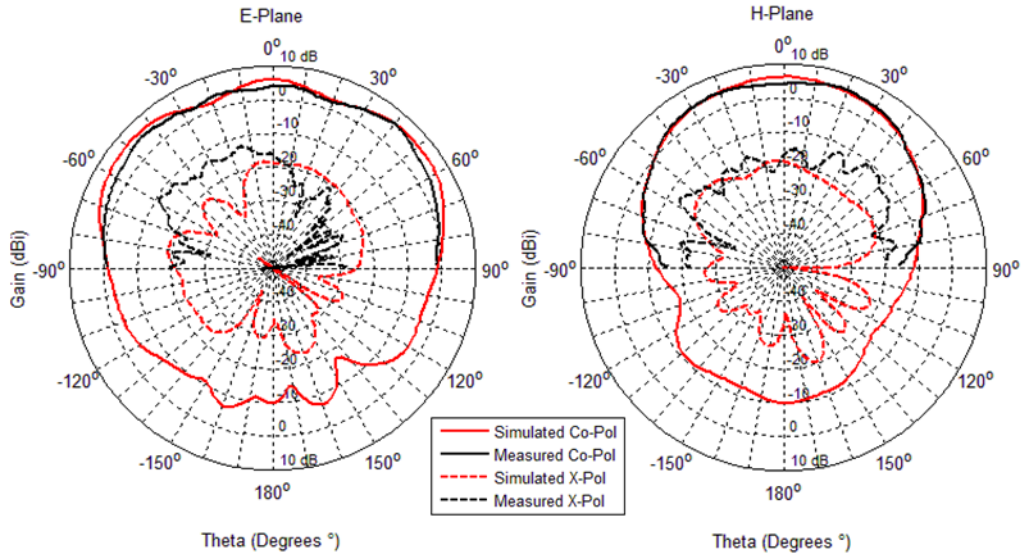

Figure 70: Measured and Simulated Gain for OSO Configuration of Dual-wall Reconfigurable DRA Operating at 6.1 GHz

Table 11: Measured and Simulated Gain and Cross Polarization Levels for Dual-wall OSO Configuration Operating at 6.1 GHz

	Peak Co-Pol Gain (H-Plane)	Peak Co-Pol Gain (E-Plane)	X-Pol – Co-Pol Level (H-Plane)	X-Pol – Co-Pol Level (E-Plane)
Simulated	6.12 dBi	6.40 dBi	-23.22 dB	-24.80 dB
Measured	5.64 dBi	5.98 dBi	-16.25 dB	-16.79 dB

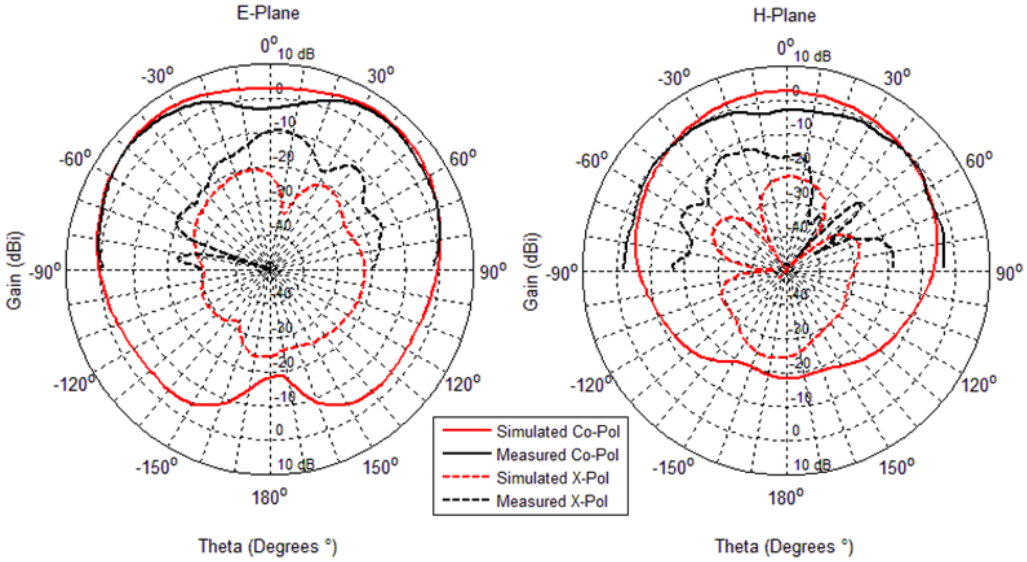

Figure 71: Measured and Simulated Gain for SSS Configuration of Dual-wall Reconfigurable DRA Operating at 3.1 GHz

Table 12: Measured and Simulated Gain and Cross Polarization Levels for Dual-wall SSS Configuration Operating at 3.1 GHz

	Peak Co-Pol Gain (H-Plane)	Peak Co-Pol Gain (E-Plane)	X-Pol – Co-Pol Level (H-Plane)	X-Pol – Co-Pol Level (E-Plane)
Simulated	2.59 dBi	5.83 dBi	-25.00 dB	-26.29 dB
Measured	-0.10 dBi	5.20 dBi	-11.70 dB	-14.59 dB

From the far field pattern results it is again clear that there is good agreement between the simulated and measured results. However, similar to the single-wall case, the measured co-polarized radiation pattern in the H-plane at frequencies below 4 GHz is much reduced at broadside (Figure 68 and Figure 71). This is not observed in the measured patterns for frequencies greater than 4GHz. Nonetheless, there is still sufficient gain in the E-plane at the low frequencies. It is also clear from the radiation patterns that the large cross polarization component in the H-plane has been successfully reduced to the target specification of -10 dB or better (x-pol maximum to co-pol maximum). Furthermore, the H-plane cross polarization radiation pattern no longer resembles that of a short electric monopole as the effect of the currents has been successfully mitigated. It is interesting to note that in the E-plane the cross polarized radiated pattern resembles that of a short electric monopole in the OOS (Figure 68 and Figure 69) and in the OSS configuration (not shown). This is likely caused by currents along the bottom edge of the shorting wall since the OOS and OSS configuration are not symmetrical in the E-plane. Since the cross polarization component is sufficiently low in the E-plane this source of unwanted radiation need not be addressed. Finally, Figure 72 contains a photograph of the fabricated dual-wall antenna in the SOS configuration.

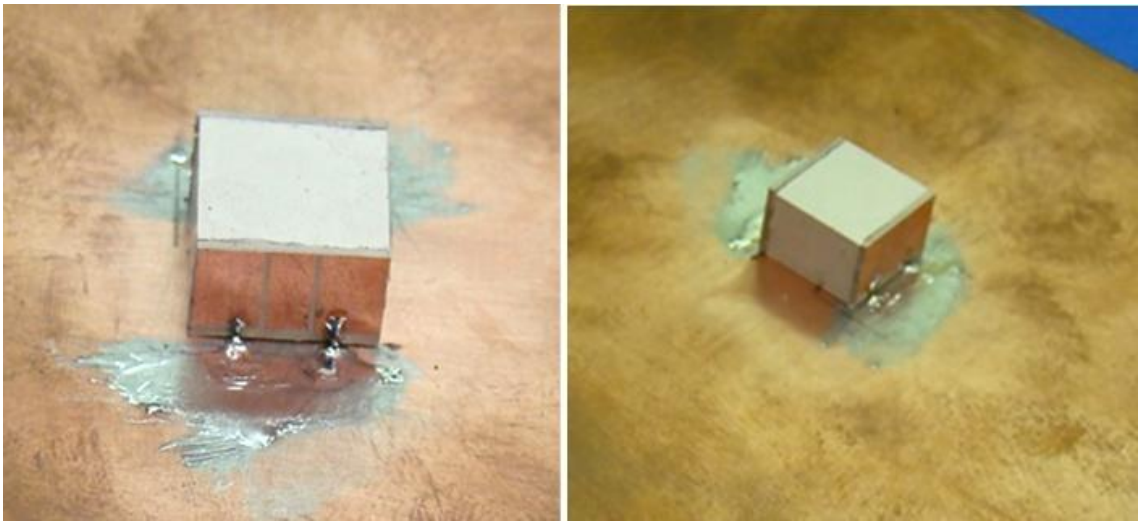

Figure 72: Fabricated Dual-wall Frequency Reconfigurable DRA

3.4 Conclusions

A novel method for achieving frequency agility with a dielectric resonator antenna has been presented using ideal switches. The theoretical tuning range performance of the single-wall reconfigurable DRA was examined for various aspect ratios and a study on various switching geometries was performed. Using this information an optimum design was obtained and simulation and measured data showing the frequency response, radiating modes and radiation pattern was presented. The fabricated single-wall frequency reconfigurable DRA obtained a measured discrete tuning range of 69% and 77% for a return loss specification of 10 dB and 6 dB respectively with two contiguous operating bands. The lower operating band (3-4 GHz) was shown to operate with the $TE^{x}_{\delta 11}$ mode and upper operating band (5-6.5 GHz) the $TE^{x}_{\delta 13}$ mode. The antenna was also shown to have a return loss of 6 dB or better over 65.7% of the tuning range from 2.9 GHz to 6.5 GHz. Although this optimised antenna's performance exceeded that in [2], there was a large cross polarized component in the H-plane resembling the fields of a short vertical electric monopole. In order to lower the cross polarization levels a dual-wall reconfigurable DRA was designed. The fabricated dual-wall frequency reconfigurable DRA achieved a measured discrete tuning range of 83% and 87% for a return loss specification of 10 dB and 6 dB respectively with multiple operating bands. The lower operating band (~ 3 GHz) was shown to operate with the $TE^{x}_{\delta 01}$ mode and upper operating bands (4-7.5 GHz) the $TE^{x}_{\delta 11}$ mode. The former mode is different from that excited in the single-wall DRA at the lower end of the

operating band. The antenna's radiation pattern had sufficient gain and the cross-polarization to co-polarization level did not exceed -10 dB. The antenna was also shown to have a return loss of 6 dB or better and a cross-polarization to co-polarization level that did not exceed -10 dB, over 66.3% of the tuning range from 2.95 GHz to 7.5 GHz. This is the best performance level achieved using DRAs.

3.5 References for Chapter 3

[1] M.T.K Tam and R.D. Murch, "Half volume dielectric resonator antenna designs", *Electronics Letters*, vol.33, no. 23, pp. 1914-1916, Nov. 1997.

[2] A. Petosa and S. Thirakoune, "Frequency Tunable Rectangular Dielectric Resonator Antenna," in *IEEE Antennas and Propagation Society International Symposium,* Charleston SC, 2009

[3] HFSS, Ansoft LLC, USA (www.ansoft.com).

[4] FEKO, EM Software & Systems Inc. (www.feko.info).

[5] EMPIRE XCcelTM, IMST GmbH, Germany (www.empire.de).

[6] Y. Gao, Z. Zhang, Z. Feng, M.F. Iskander and L. Ruihong, "Dielectric resonator antenna with TEδ01 mode", in *IEEE Antennas and Propagation Society International Symposium,* Toronto, 2010.

[7] A. Petosa, S. Thirakoune, A. Ittipiboon, "Higher-order modes in rectangular DRAs for gain enhancement," in *Antenna Technology and Applied Electromagnetics and the Canadian Radio Science Meeting,* Banff ,2009, pp.1-4.

Chapter 4 - Reconfigurable Dielectric Resonator Antennas - PIN Diode Switching

4.1 Introductory Remarks

As the dual-wall frequency reconfigurable antenna from Section 3.3 showed excellent performance, the ideal switches (tabs) were replaced with PIN diodes in order to achieve electronic switching. In this chapter the selection process for the PIN diodes is outlined in Section 4.2 along with equivalent circuit models that represent the two PIN diode states. The antenna design is then presented in Section 4.3 along with simulation and measured data showing the frequency response and radiation pattern in Section 4.4. In addition, the bias network design and DC power consumption are discussed.

4.2 PIN Diode Selection and Characterization

In order to achieve discrete tuning using electronic switching, a MEMS switch, PIN diode or FET is required. The author selected to use PIN diodes due to several reasons. Firstly, since PIN diodes are a mature technology they are inexpensive, very low loss, have good isolation and are easy to model with lumped elements. Making use of low cost components is an essential requirement if such an antenna is to be used for mobile communications. Furthermore, the PIN diode's small physical size compared to wavelength, its high switching speed, and the low package parasitic reactances, make it an ideal component for use in miniature, broadband RF signal control circuits. In addition, the PIN diode has the ability to control moderate amounts of RF signal power while using small levels of control power (approximately 8.5 dBm) [1]. The package size of the device was also a very important requirement since there was little flexibility in terms of device footprint as the switching device must have two ports and be no larger than 2 mm by 0.5 mm. The aforementioned requirements eliminated all other devices, leaving the PIN diode as the selected switching component.

Given the plethora of PIN diodes available for use, and the wide array of applications, it was important to select the most advantageous device. It was determined that the optimum PIN diode for the application would be a beam lead PIN diode. However, although beam lead PIN diodes have the optimal characteristics over the operating range they are very expensive compared to their plastic packaged silicon counterparts. Thus, once again with possible use of

reconfigurable DRAs for consumer devices in mind, the decision was made to use a standard plastic packaged silicon PIN diode that is designed to operate as a high isolation wireless switch from 10 MHz to 6 GHz (Skyworks SMP1345 package SC-79 [2]). Although the PIN diode is designed to operate from 10 MHz to 6 GHz the device will still operate effectively up to 9 GHz without significant losses. The particular PIN diode used was selected due to its very low capacitance (0.115 pF), resistance (0.8 Ω) and forward bias voltage level (0.89 V).

In order to accurately predict the performance of the antenna the PIN diodes characteristics were extracted. To accomplish this, the non-linear SPICE model of the PIN diode [2] was obtained from the manufacturer along with the equivalent circuit for the package parasitics. A switching configuration model which contains the non-linear SPICE model of the PIN diode as well as the package parasitics as shown in Figure 73 was created using ADS [3]. As is evident in Figure 73 the model makes use of an ideal bias network since an ideal DC block and RF choke inductor are used. The configuration was then simulated from 1 – 10 GHz and the S-parameters were obtained. Next, a simplified RLC equivalent circuit model for the PIN diode was adopted (so that it can be included in later electromagnetic simulations of the complete antenna), as indicated in Figure 74. The values of the components in the simplified equivalent circuits will shortly be adjusted so that their S-parameters match those obtained from the SPICE model. Before doing this, it will be useful to note that an “ideal switch” exhibits zero resistance to current flow in the “ON” state and infinite resistance to current flow in the “OFF” state. A practical switch design exhibits a finite (albeit low) resistance in the “ON” state and a finite (albeit high) resistance in the “OFF” state. Therefore, the PIN diode’s equivalent circuit consists of a series parasitic inductance (L), an intrinsic capacitance (C_T) in parallel with an intrinsic resistance (R_P) for the reverse bias case (0 V), and a series parasitic inductance (L) in series with an intrinsic resistance (R_S) for the forward bias case (0.9V) as shown.

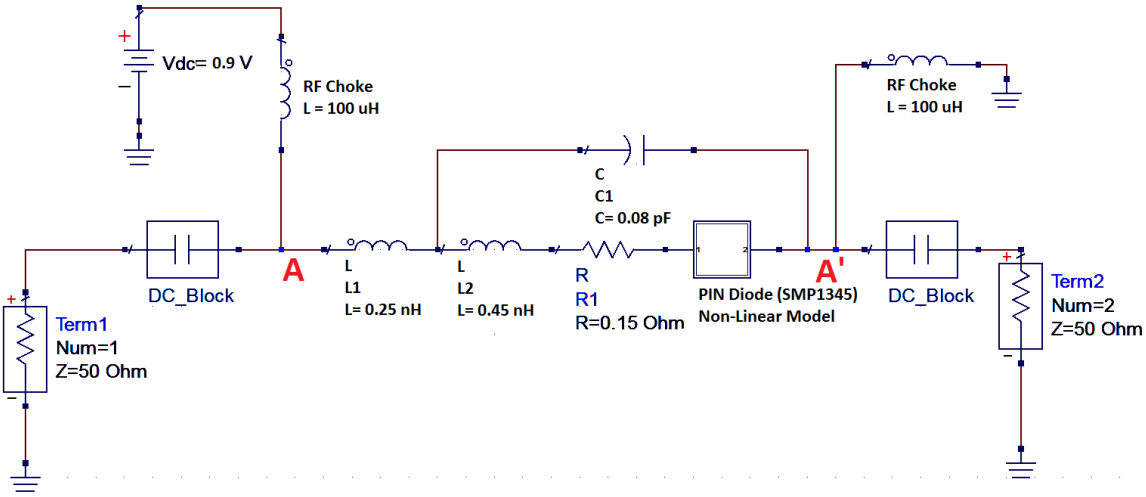

Figure 73: Non-Linear SPICE Model of Skyworks SMP1345 PIN Diode with Ideal Bias Network

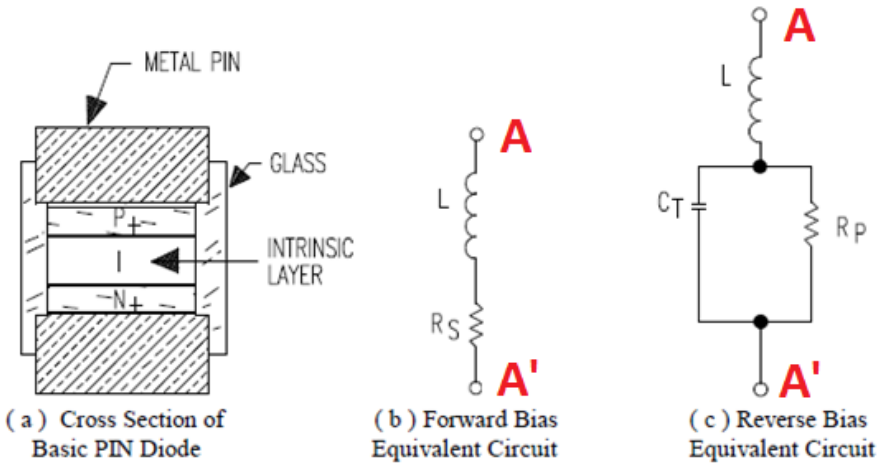

Figure 74: PIN Diode and Corresponding Equivalent Circuits (After [1])

Using the information from the manufacturer the parameter values for the equivalent model were selected and then fine tuned in order to better agree with the SPICE model. The results of the parameter extraction using ADS are shown in Table 13. Figure 75 and Figure 76 show the simulated S-parameters for both the SPICE model and the equivalent model. From the S-parameter results it is evident that the performance of the antenna will likely be degraded at frequencies over 7 GHz due to the degradation in isolation performance when the diode is switched off (S12 crossed -5 dB), and reflections when the diode is switched on (S11 crosses -10 dB). As shown, there is good agreement between the SPICE model and the equivalent circuit model. If the switch were ideal we would have S11 = 0 dB and S12= -∞ dB when it is open, and

S11= -∞ dB and S12= 0 dB when it is closed. The equivalent circuit models can be integrated into HFSS simulation in order to predict the performance of the complete antenna with PIN diodes.

Table 13: Parameter Values of Equivalent Circuit for PIN Diode

Voltage	Parameters			
	L (nH)	R_S (Ω)	R_P (Ω)	C_T (pF)
0 V (Reverse Bias)	0.7	-	4000	0.115
0.9 V (Forward Bias)	0.7	0.8	-	-

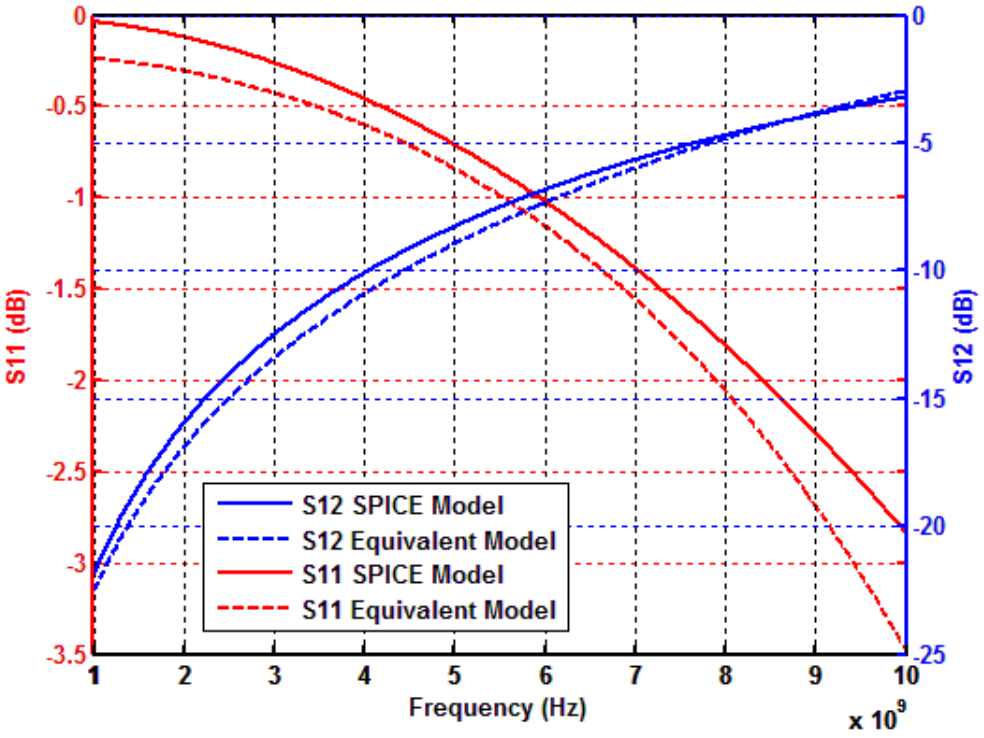

Figure 75: Simulated S-Parameters for the PIN Diode (SMP1345) when Biased at 0 V

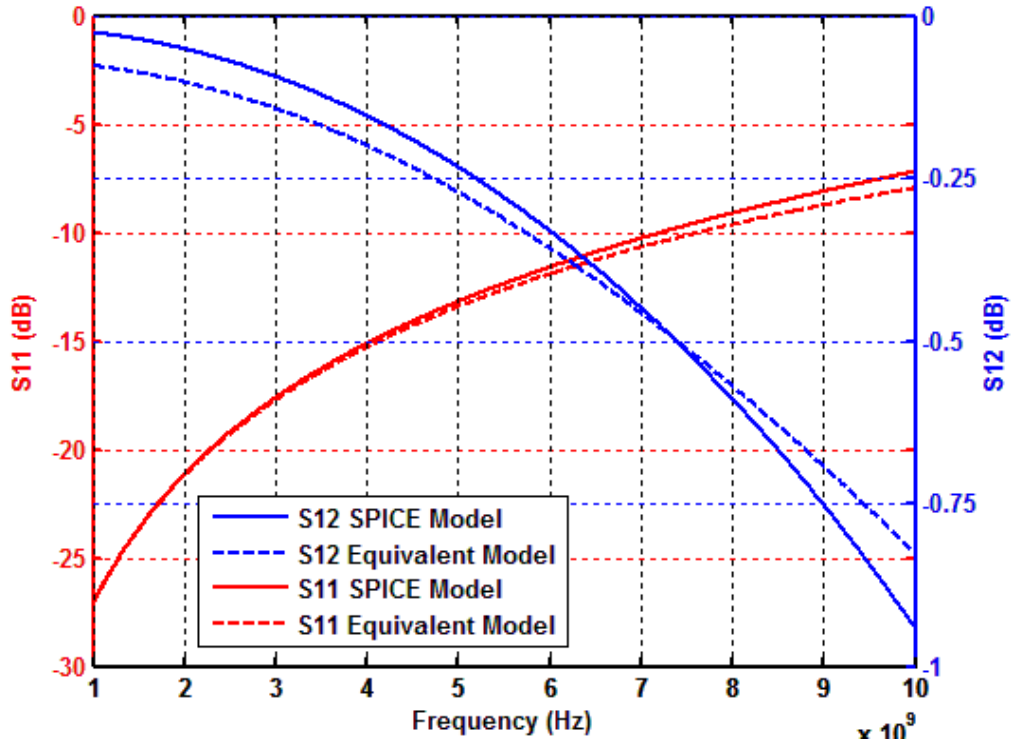

Figure 76: Simulated S-Parameters for the PIN Diode (SMP1345) when Biased at 0.9 V

4.3 Dual-wall Frequency Agile DRA with PIN Diode

Since an accurate equivalent circuit model of the PIN diode has been achieved that makes use of lumped elements, electromagnetic simulation can be performed using HFSS with the practical PIN diode effects included. The equivalent circuit model of the PIN diode is included in HFSS by creating a surface (identical to the PIN diodes package geometry) and assigning a lumped RLC boundary to it. The antenna, with the exception of the PIN diodes, is almost identical to that of Section 3.3.1 except for some minor variations that will be discussed immediately below. In order to provide adequate space for the PIN diode the shorting wall gap was increased to 3 mm, as indicated in Figure 77. A 1 mm gap is also added to accommodate the PIN diode SC-79 package as shown in Figure 78.

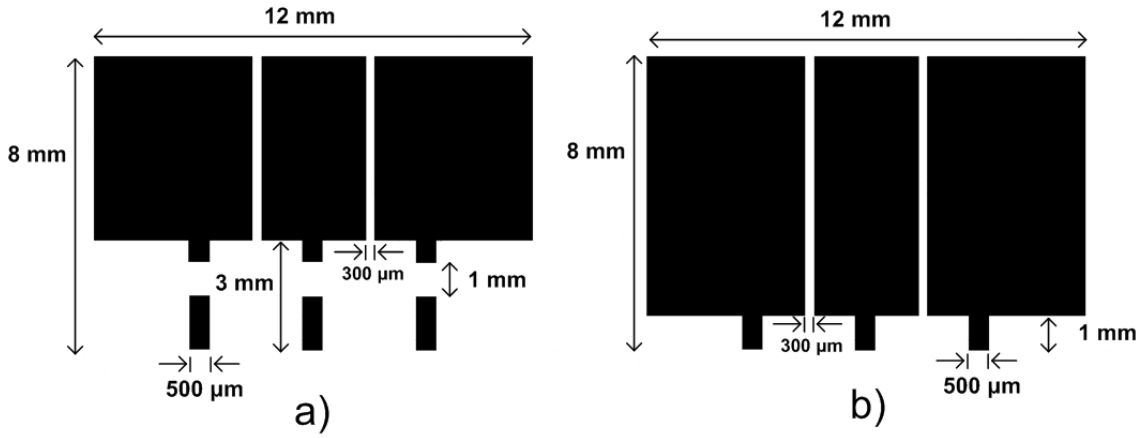

Figure 77: a) Shorting Wall Geometry for PIN Diode b) Shorting wall Geometry for Ideal Switch (SSS Configuration)

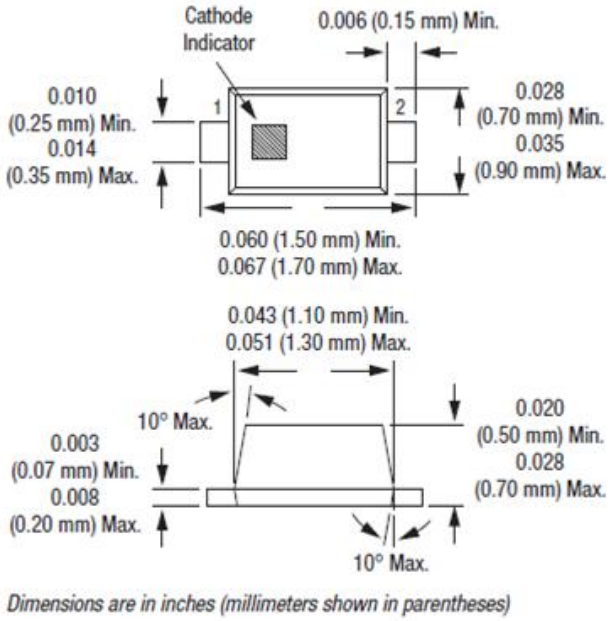

Figure 78: Skyworks SMP1345 PIN Diode's SC-79 Package Dimensions (After [2])

The other change that was required is in relation to the bias network. Since the DC and RF sources must be isolated from one another, RF choke inductors and DC blocking capacitors are employed. DC blocking capacitors are utilized to block DC signals while passing RF with as little loss as possible. It is clear from the DRA feeding mechanism that the RF signal is electrically isolated from the DC signal since the microstrip feed line is electromagnetically coupled to the DRA. On the other hand the RF and DC ground are shared via the ground plane. Therefore, DC currents on the ground plane are unblocked. In order to prevent any unwanted DC interference two methods are employed. The first makes use of a DC blocking capacitor that operates

between 10 MHz to 18 GHz and can withstand 200 V. The DC blocking capacitor is integrated into the outer conductor of an SMA male-female connector. The device is shown in Figure 79 and is manufactured by Aeroflex, model number 8038 [4].

Figure 79: Aeroflex 8038 Male-Female SMA DC Blocking Capacitor on Outer Conductor (After [4])

Although adding an SMA DC blocking capacitor is a solution, such a technique is not feasible if the antenna is used for mobile communications, consequently a second solution was also developed. The second technique involved placing a 254 µm gap in the ground plane 25 mm from the center of the aperture that effectively separates it in two. A surface mount DC blocking capacitor of 0.1 µF [5] was then connected in order to bridge the two ground plane sections. The DC blocking capacitor's value of 0.1 µF was selected over a lower capacitor value since a package size had to be selected that could bridge the 254 µm gap. The capacitor was placed at the center of the ground plane opposite the microstrip line since this is where the surface currents on the ground plane would be the largest (albeit not being zero elsewhere). The configuration is shown in Figure 80. The 0.1 µF DC blocking capacitor and 254 µm gap were also implemented in simulation. The configuration with the SMA DC blocking capacitor will be distinguished as board one, while the 254 µm gap and surface mount DC blocking capacitor is distinguished as board two.

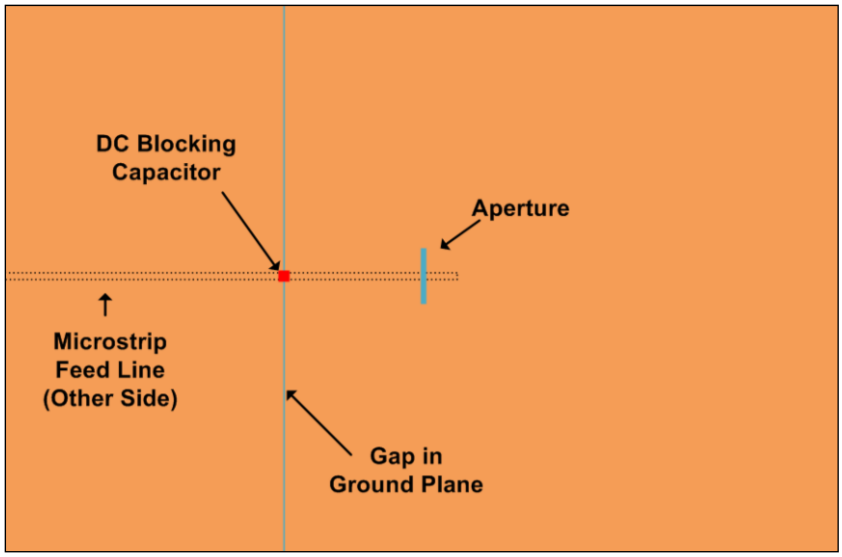

Figure 80: Layout of Gap Configuration for Surface Mount DC Blocking Capacitor (This is essentially a top view of the layout in Figure 18, with the DRA removed)

In order to verify that the SMA DC blocking capacitor does not introduce any additional losses a measurement was performed without the presence of a DRA. From the results in Figure 81 it is clear that the SMA DC blocking capacitor does not introduce any significant losses. On the other hand, similar measurements on board two exhibit unwanted resonances at 3.4 GHz and 5.6 GHz, as indicated in Figure 82. Observe also from Figure 82 that the resonances are not as sharply predicted by the HFSS simulation. They appear to be present, albeit shifted up in frequency relative to measurements, and are "shallower" than their measured counterparts. This is most likely due to the fact that for the measured results we have an actual lumped capacitor while in the HFSS model we have to represent this as a distributed reactively loaded surface with 0.5 mm width. In the model environment a 0.5 mm wide surface is present over the gap but has an effective capacitance of 0.1 μF. Thus the two situations are not identical. Attempts were made to increase the discretization in the HFSS model as well as add additional capacitors to the fabricated design. Both methods yielded no improvement or change in result. Although the resonance at 3.4 GHz and 5.6 GHz is unwanted, for the purpose of this research the results of board two will still be presented.

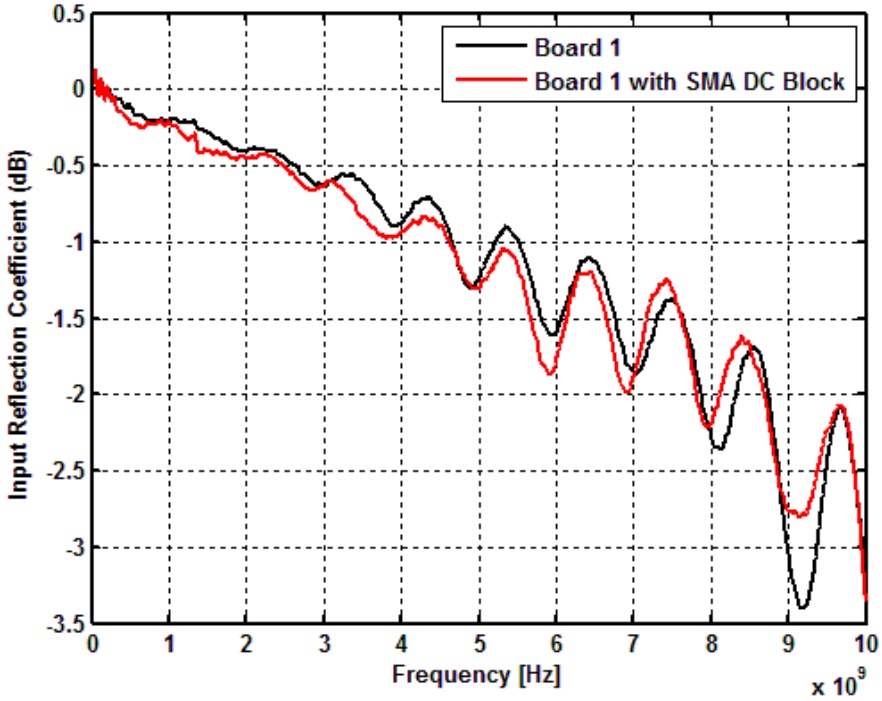

Figure 81: Measured Frequency Response of Board One With and Without SMA DC Blocking Capacitor

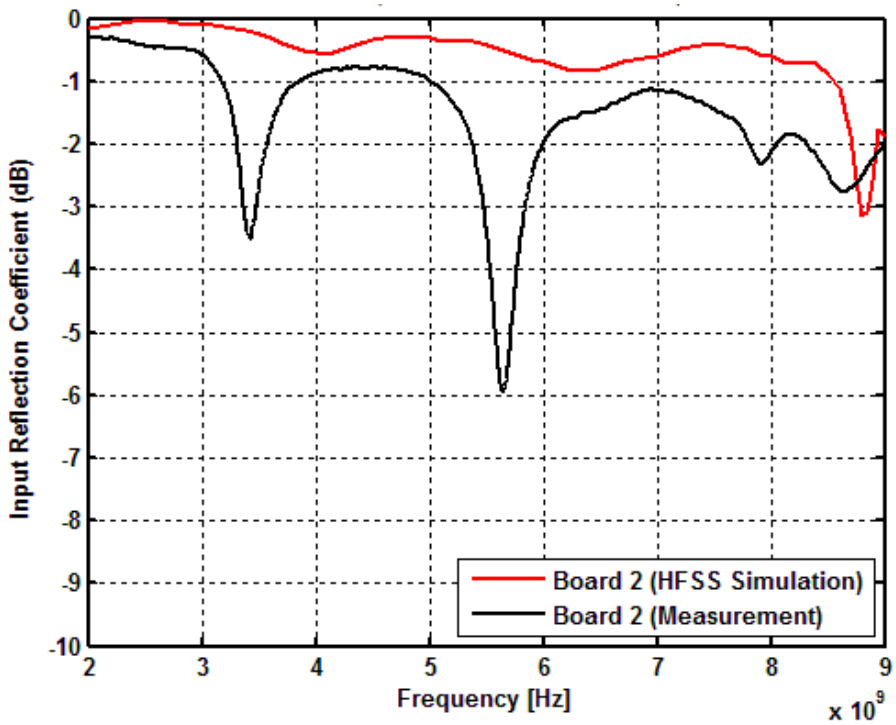

Figure 82: Frequency Response of Board Two with DC Blocking Capacitor

In order to isolate the DC power supply from unwanted RF signals it is crucial to use an RF choke inductor. To accomplish this, four surface mount very wideband RF choke inductors that

operate from 50 MHz to 10 GHz and can support up to 100 mA of current were used [6]. The RF chokes have an inductance of approximately 3 μH. Four inductors are required for the three sets of PIN diodes and the ground path. A small printed circuit board (PCB) was fabricated in order to facilitate the integration of the RF choke inductors as well as the bias wires leading to the shorting wall and the leads connected to the power supply. A photograph of the DC bias PCB is shown in Figure 83.

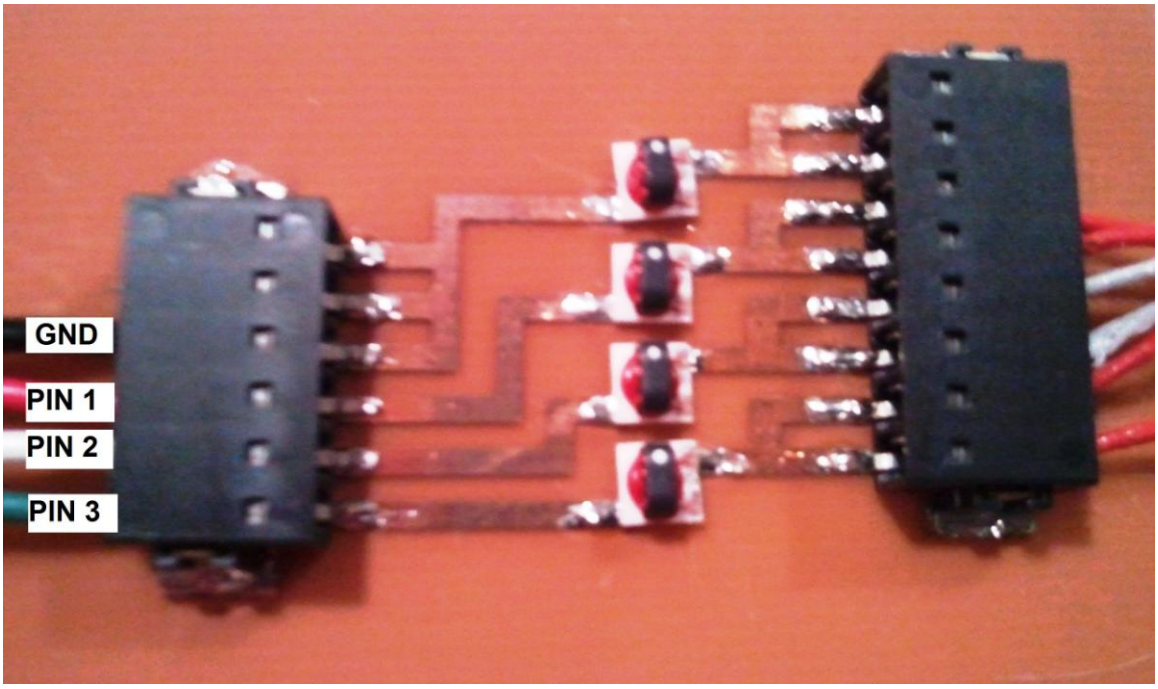

Figure 83: Photograph Showing DC Bias PCB Complete with RF Choke Inductors and Bias Lead Housings

The next step was to connect the DC bias leads from the DC bias PCB to their respective shorting wall. This was first performed by soldering the leads to their respective PIN diode on the shorting wall, spiralling the leads and then routing them back to the DC bias PCB. Although this method had a very clean appearance there was very strong coupling between the leads for the OOO configuration. Since it was clear that there was significant crosstalk between the bias leads they were routed individually and secured with copper tape, which aside from acting as an adhesive also shields the leads to minimize crosstalk, as shown in Figure 84. Figure 85 shows measurement for the OOO case with the two routing methods along with a case where no bias lines were present, which serves as the ideal case.

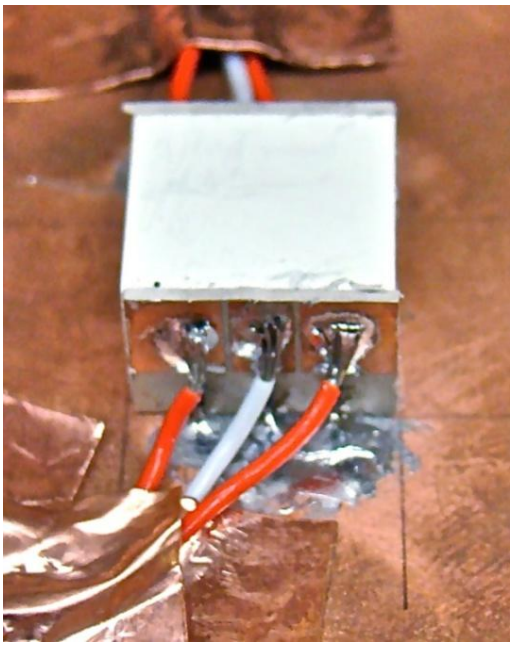

Figure 84: Connection and Routing of Bias Leads for Dual-wall Frequency Reconfigurable DRA with PIN Diodes

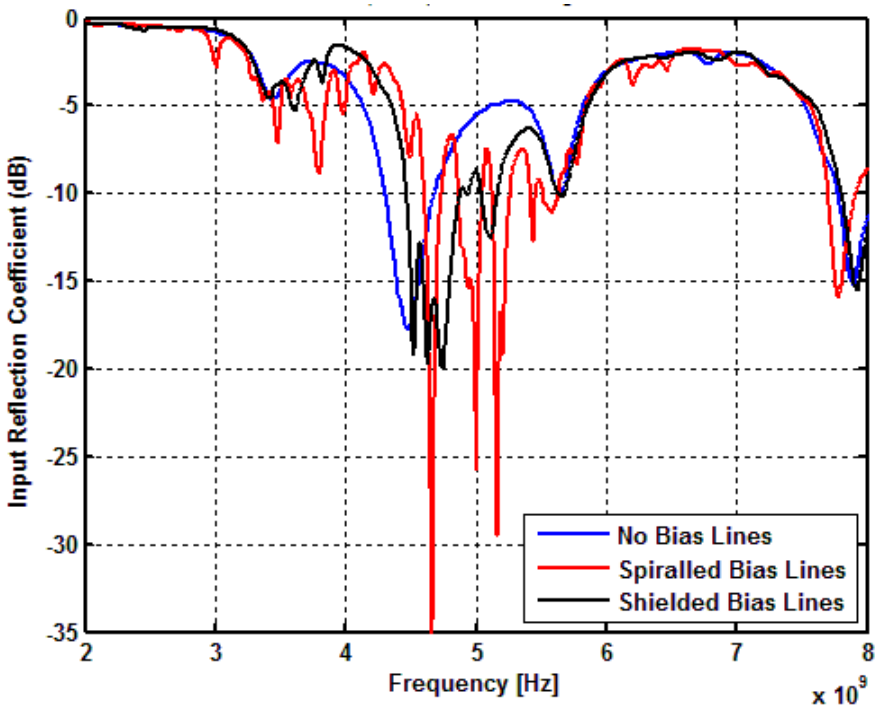

Figure 85: DRA Input Reflection Coefficient for Different Routing Methods for the OOO Configuration using Board Two

It is clear from Figure 85 that without the shielding there is significant crosstalk between the leads and that using shielded bias lines best represents the ideal case where no bias leads are

present. Finally, in order to switch the PIN diodes three power supplies were utilized so that the power consumption could be measured independently.

4.4 Measured and Computed DRA Switching Performance

Since the tabs on either side of the DRA are switched as pairs there are, as noted in Section 3.2.2, six different antenna configurations. Once the antenna was fabricated the input reflection coefficient was measured and compared to simulation using HFSS for each of the switched states. The results are shown in Figure 86 to Figure 91 for both boards one and two. In other words, there is one figure for each of the six states OOO, OOS, OSO, OSS, SOS and SSS. The simulation results shown in the figures are always for board one. Simulation results were obtained for board two but were not included as they closely agree with those of board one, as the HFSS model does not predict the unwanted resonance at 3.4 GHz and 5.6 GHz, as mentioned in Section 4.3.

The measured center-frequencies of the switched states are consistently about 7.5% higher than the computed values. The agreement between the computed and measured values of the antenna is much better in the case of the ideal “switches” of Chapter 3. This is likely due to any number of the following reasons.

- Positioning of the DRA
- Air gaps between the ground plane and DRA
- Air gaps between the DRA and shorting wall substrate
- Soldered tab to ground plane connection
- Shorting wall positioning on the DRA
- The material manufacturers’ design tolerances
- Presence of DC bias leads
- Reactive loading of the PIN diode that is not accounted for in the model

In spite of this, the agreement between computation and measurement is satisfactory in the sense that the ability to switch to six different operating bands is properly predicted, which also confirms that the equivalent circuit model for the PIN diodes is a good one. In order to further confirm that the equivalent circuit model for the PIN diode is acceptable a comparison is shown between the equivalent circuit model that is adapted in HFSS and a model that is similar to that of Chapter 3 (tabs present to represent the “short” condition and absent to represent the

"open" condition). The results of two cases are shown in Figure 89 and Figure 90 along with measured data for board one and two as indicated. It is clear that without the PIN diode equivalent circuit model the operating band is predicted to occur much higher in frequency, as shown in both figures. This prediction is not in agreement with typical observations as the fabricated antenna would normally be shifted up in frequency due to air gaps. Furthermore, if the equivalent circuit model was inaccurate the continuous tuning aspect that will be shown in Chapter 5 with varactors would not be able to predict the performance, which is not the case. Thus it follows that the equivalent circuit model of the PIN diodes is in fact reliable.

In regards to the DC bias leads, the prototype further emphasizes the robustness of the design since the bias leads for the prototype antenna are far from optimally laid out. It is evident that the fabricated antenna achieved a tuning range of 95% and 97% for a return loss specification of 10 dB and 6 dB respectively with board one and of 95% and 99% for a return loss specification of 10 dB and 6 dB respectively with board two. This closely resembles the predicted tuning range obtained via simulation, which was determined to be 96% and 100% for a return loss specification of 10 dB and 6 dB respectively with board one and of 61% and 104% for a return loss specification of 10 dB and 6 dB respectively with board two. The reconfigurable antenna has several operating bands as shown in Figure 92 and Figure 93. Where the data points in the figures represent frequencies where there is either a -10dB or -6 dB input reflection or better, as indicated. In other words it displays the tuning range of the antenna along with all tuning operating bands that meet or exceed the specification of a 10 dB or 6 dB return loss. The third operating band from 7.5 GHz to 8.5 GHz corresponds to the SSS configuration only as this corresponds to the $TE^{x}_{\delta 11}$ mode of operation whereas at all other configurations the resonance observed above 7 GHz is unwanted.

It is clear that the dual-wall reconfigurable DRA with PIN diodes exceeds the performance of the dual-wall antenna in Chapter 3 that utilized ideal switches. The reason for this is due to the change in the shorting wall gap over the ground plane. The change from a 1 mm gap to a 3 mm gap leaves the $TE^{x}_{\delta 01}$ mode (~ 3GHz) unchanged while shifting the $TE^{x}_{\delta 11}$ modes down in frequency. This can be seen by comparing Figure 61 with Figure 92. In the ideal switching case the SSS configuration's $TE^{x}_{\delta 11}$ mode resonance occurred around 9 GHz which resulted in a very poor pattern and thus was not included, while in the PIN diode design in this chapter the SSS

configuration's $TE^{x}_{\delta 11}$ mode is resonant around 8 GHz, which results in a pattern similar to that of a short horizontal magnetic dipole.

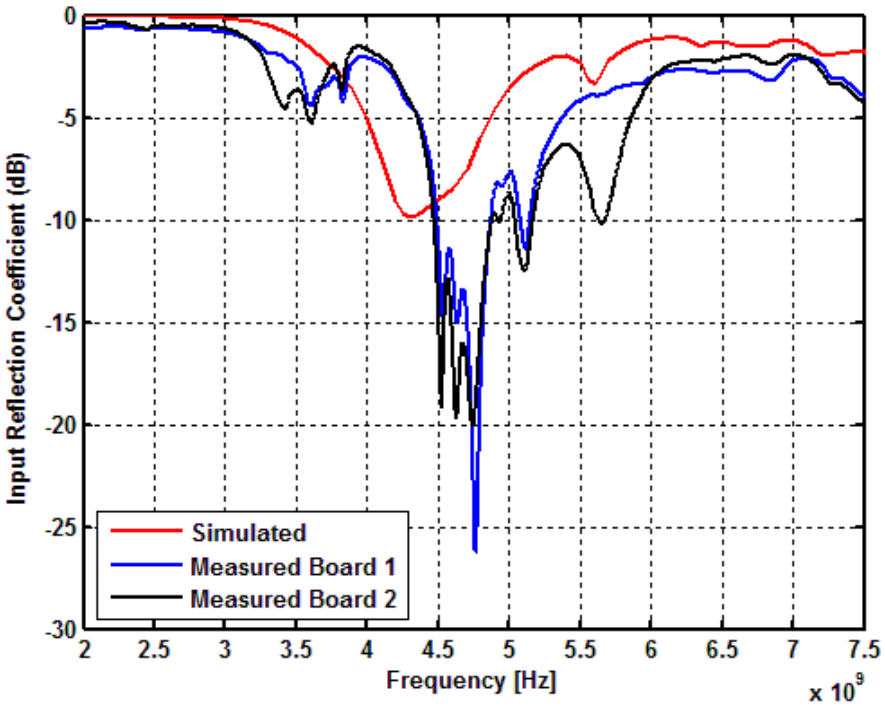

Figure 86: Frequency Response of PIN Diode Switched Dual-wall Reconfigurable DRA for OOO Configuration

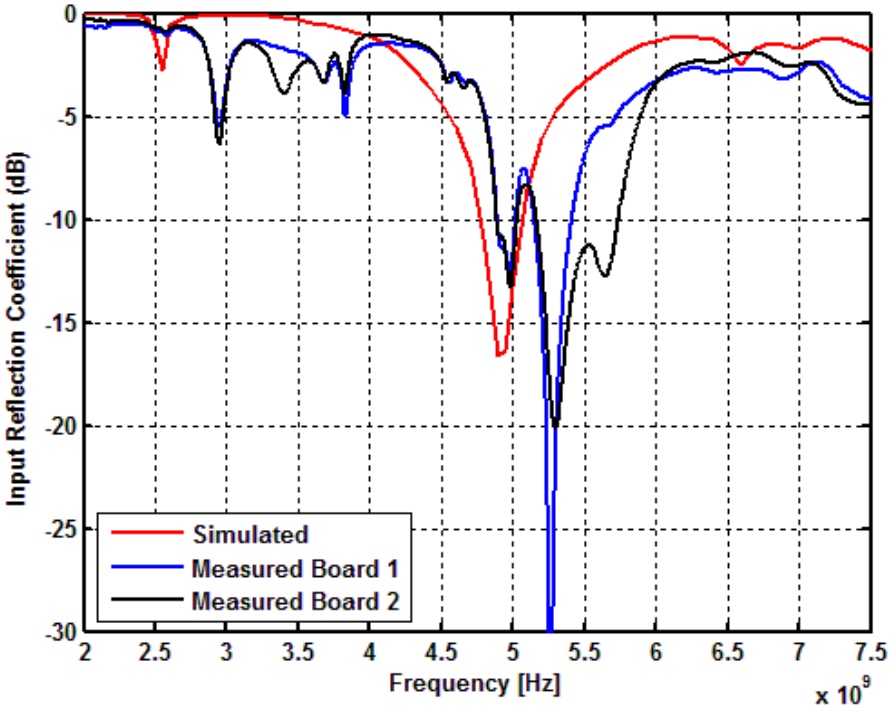

Figure 87: Frequency Response of PIN Diode Switched Dual-wall Reconfigurable DRA for OOS Configuration

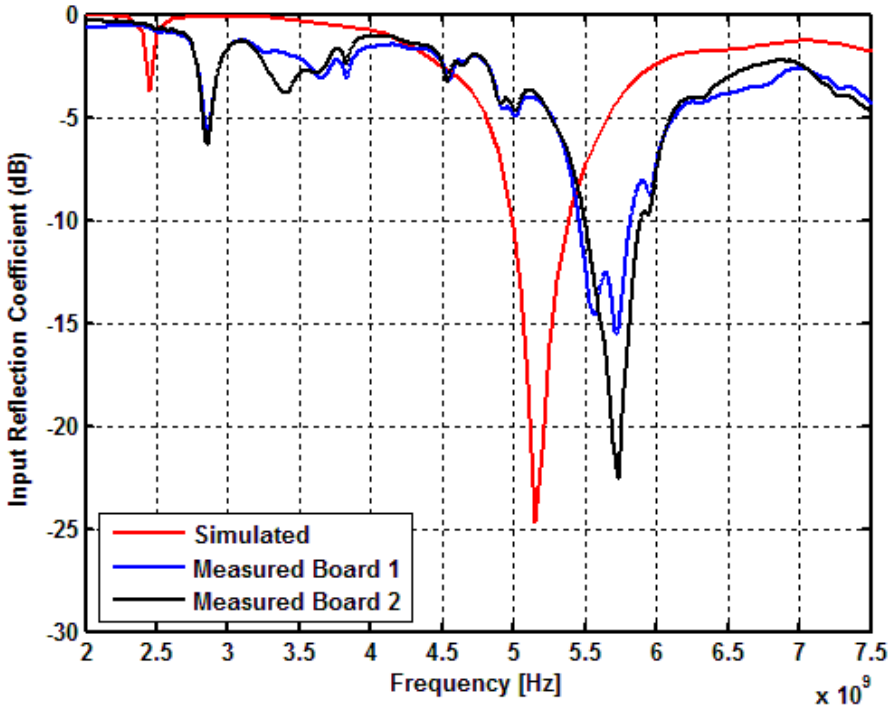

Figure 88: Frequency Response of PIN Diode Switched Dual-wall Reconfigurable DRA for OSO Configuration

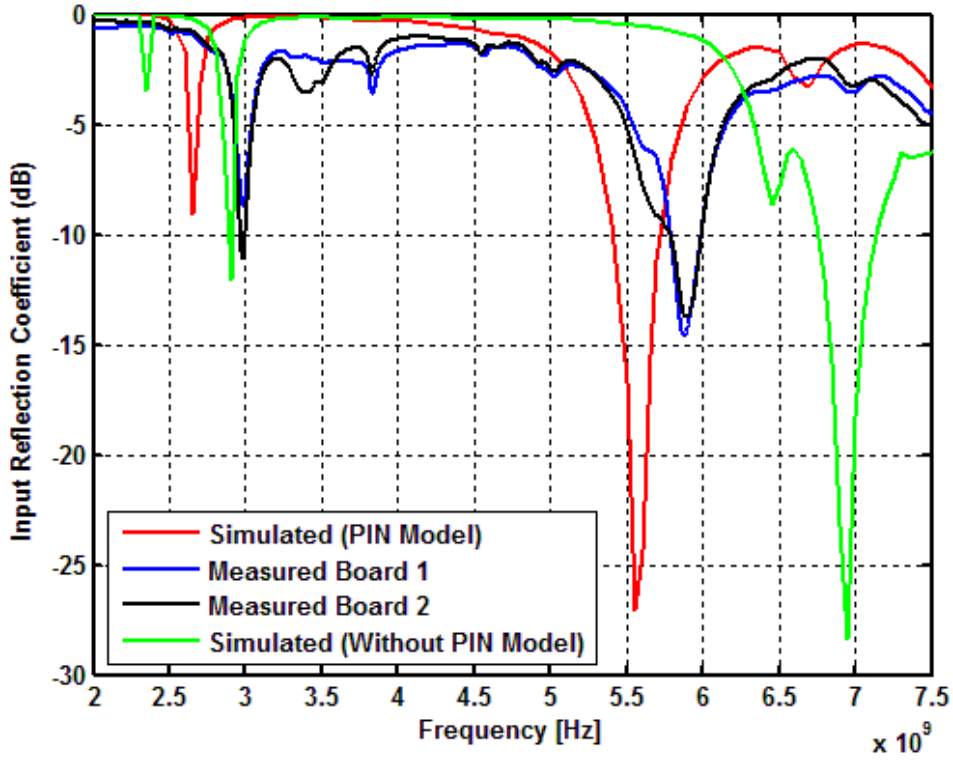

Figure 89: Frequency Response of PIN Diode Switched Dual-wall Reconfigurable DRA for OSS Configuration

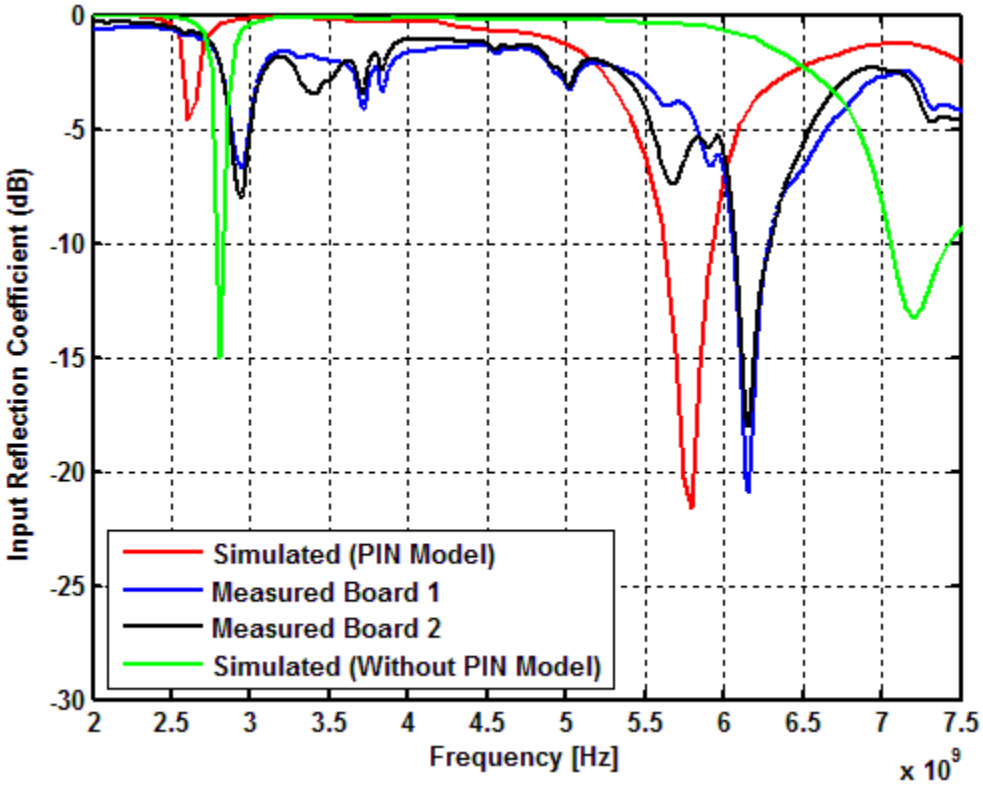

Figure 90: Frequency Response of PIN Diode Switched Dual-wall Reconfigurable DRA for SOS Configuration

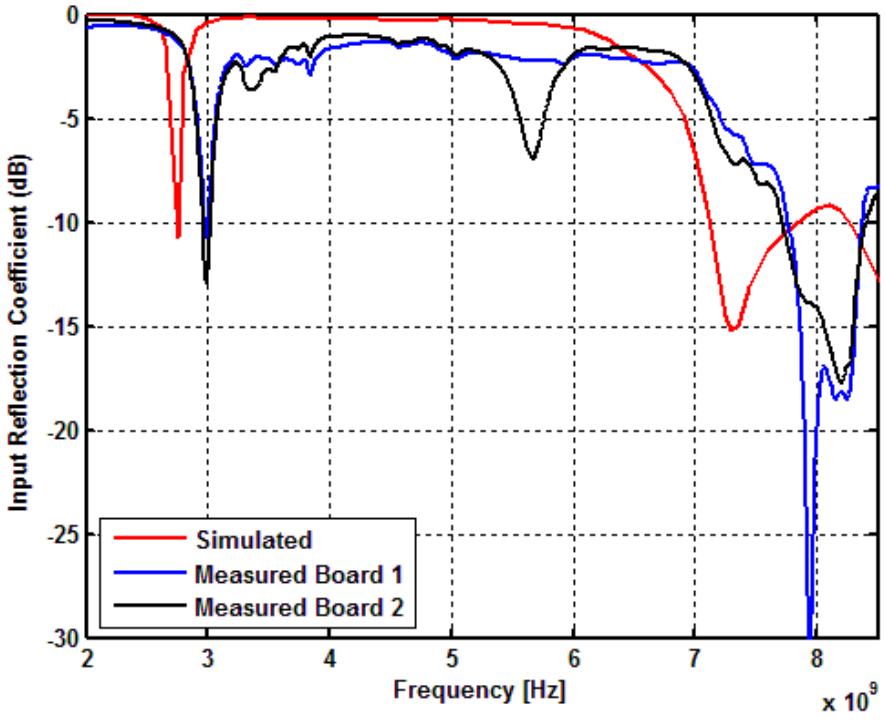

Figure 91: Frequency Response of PIN Diode Switched Dual-wall Reconfigurable DRA for SSS Configuration

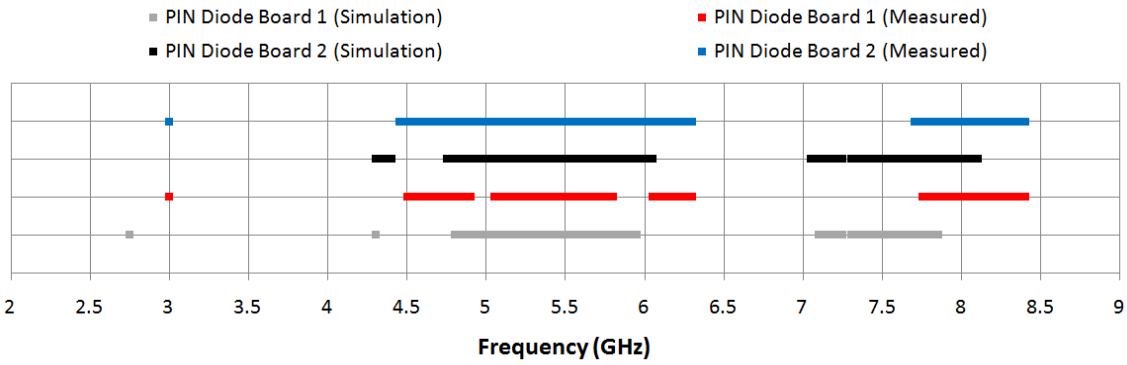

Figure 92: Tuning Range and Tuning Operating Bands that Satisfy a 10 dB Return Loss for PIN Diode Switched Dual-wall Reconfigurable DRA

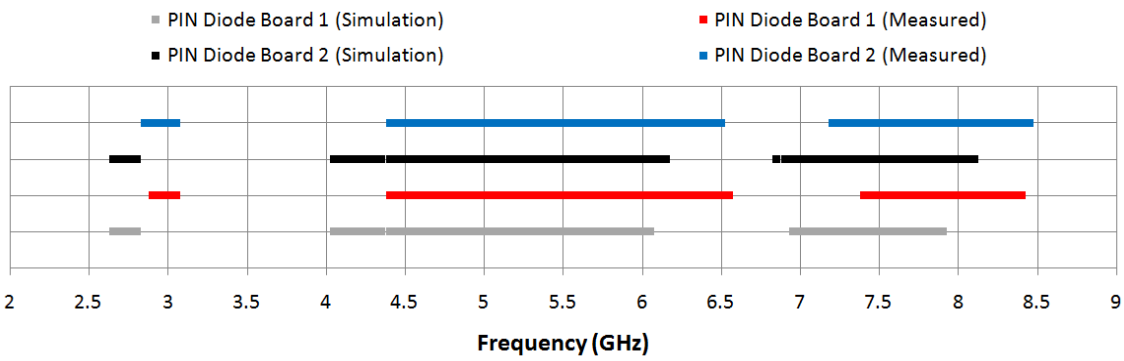

Figure 93: Tuning Range and Tuning Operating Bands that Satisfy a 6 dB Return Loss for PIN Diode Switched Dual-wall Reconfigurable DRA

The radiation patterns of the various configurations were also simulated and measured. These are shown for four of the states Figure 94 to Figure 97. The cases shown are highly representative of the results for all configurations and at all operating frequencies. A summary of the simulated and measured results is provided in Table 14 to Table 17. This identifies the gain of each configuration as well as the cross-polarized to co-polarized level in both the E-plane and H-plane.

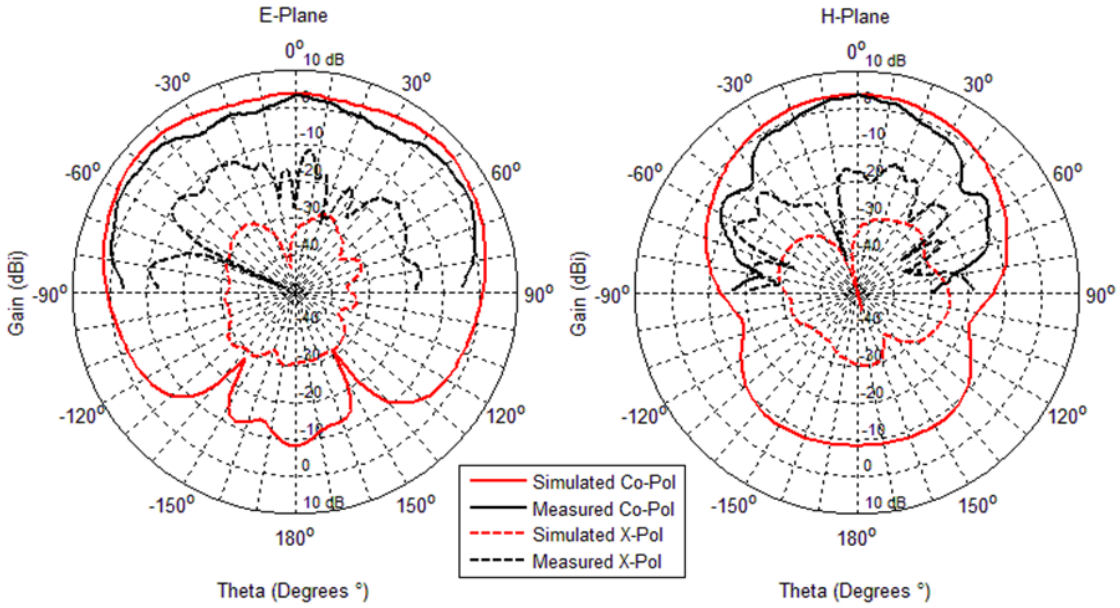

Figure 94: Measured and Simulated Gain for OOO Configuration of PIN Diode Switched Dual-wall Reconfigurable DRA Operating at 4.8 GHz (Board 1)

Table 14: Measured and Simulated Gain and Cross Polarization Levels for PIN Diode Switched Dual-wall OOO Configuration Operating at 4.8 GHz (Board 1)

	Peak Co-Pol Gain (H-Plane)	Peak Co-Pol Gain (E-Plane)	X-Pol – Co-Pol Level (H-Plane)	X-Pol – Co-Pol Level (E-Plane)
Simulated	3.70 dBi	6.20 dBi	-28.47 dB	-33.6 dB
Measured	3.32 dBi	3.97 dBi	-15.88 dB	-13.58 dB

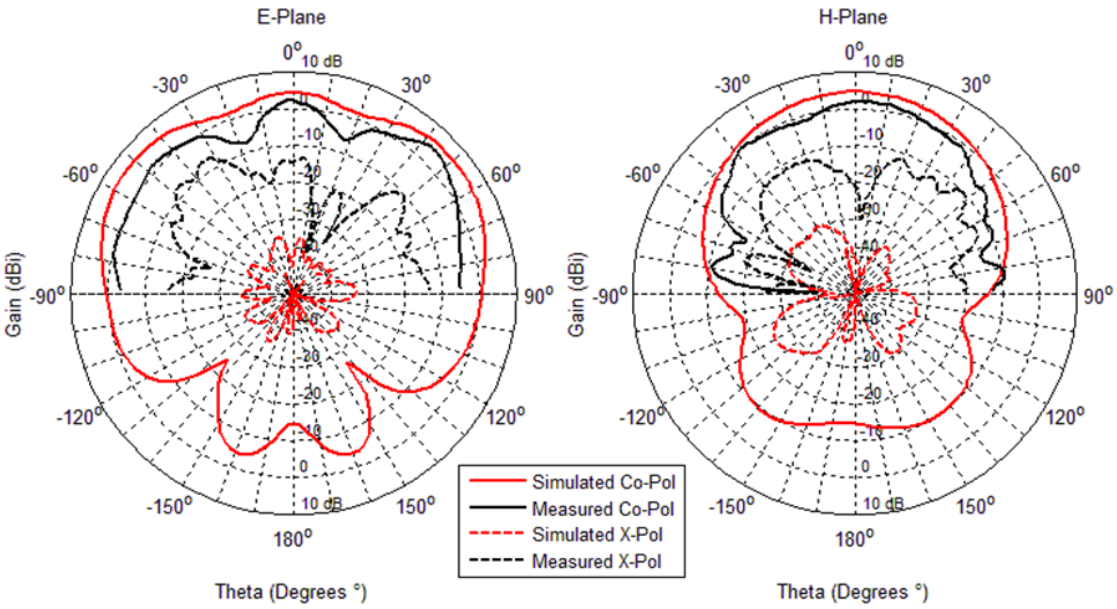

Figure 95: Measured and Simulated Gain for OSO Configuration of PIN Diode Switched Dual-wall Reconfigurable DRA Operating at 5.7 GHz (Board 1)

Table 15: Measured and Simulated Gain and Cross Polarization Levels for PIN Diode Switched Dual-wall OSO Configuration Operating at 5.7 GHz (Board 1)

	Peak Co-Pol Gain (H-Plane)	Peak Co-Pol Gain (E-Plane)	X-Pol – Co-Pol Level (H-Plane)	X-Pol – Co-Pol Level (E-Plane)
Simulated	4.59 dBi	6.03 dBi	-29.79 dB	-39.15 dB
Measured	1.91 dBi	4.34 dBi	-11.74 dB	-10.99 dB

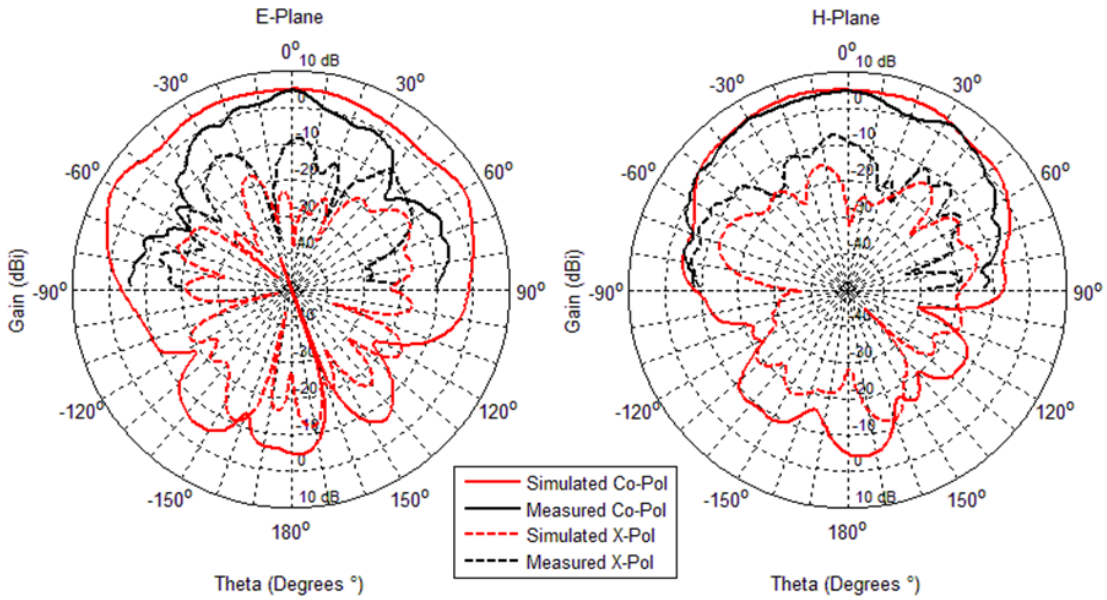

Figure 96: Measured and Simulated Gain for SSS Configuration of PIN Diode Switched Dual-wall Reconfigurable DRA Operating at 8.2 GHz (Board 1)

Table 16: Measured and Simulated Gain and Cross Polarization Levels for PIN Diode Switched Dual-wall SSS Configuration Operating at 8.2 GHz (Board 1)

	Peak Co-Pol Gain (H-Plane)	Peak Co-Pol Gain (E-Plane)	X-Pol – Co-Pol Level (H-Plane)	X-Pol – Co-Pol Level (E-Plane)
Simulated	5.41 dBi	6.22 dBi	-17.37 dB	-18.72 dB
Measured	4.55 dBi	4.56 dBi	-10.52 dB	-11.62 dB

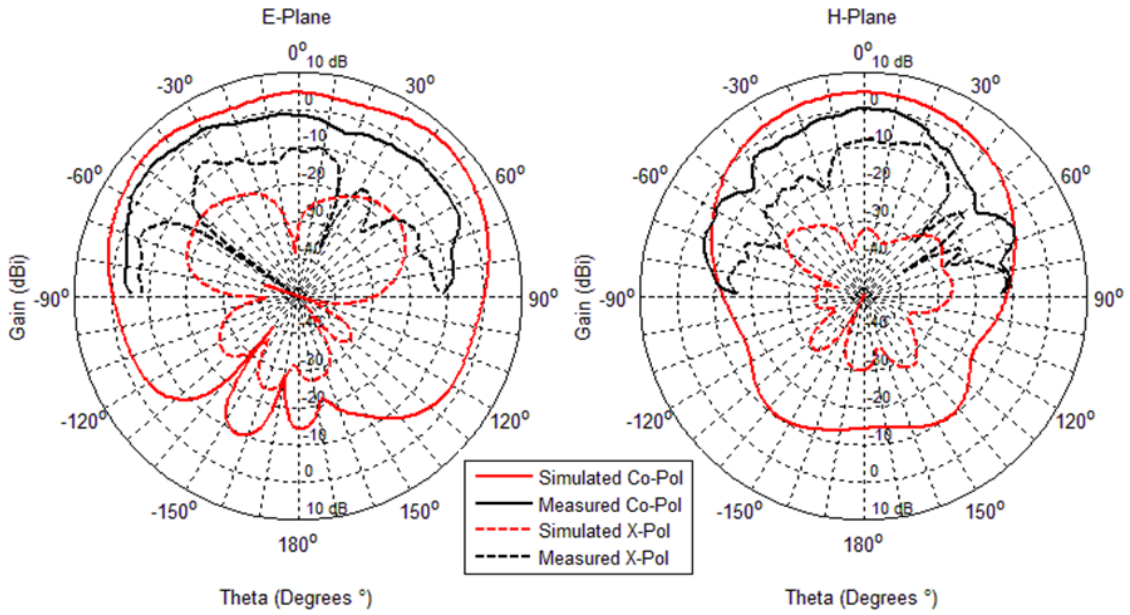

Figure 97: Measured and Simulated Gain for OOS Configuration of PIN Diode Switched Dual-wall Reconfigurable DRA Operating at 5.0 GHz (Board 2)

Table 17: Measured and Simulated Gain and Cross Polarization Levels for PIN Diode Switched Dual-wall OOS Configuration Operating at 5.0 GHz (Board 2)

	Peak Co-Pol Gain (H-Plane)	Peak Co-Pol Gain (E-Plane)	X-Pol – Co-Pol Level (H-Plane)	X-Pol – Co-Pol Level (E-Plane)
Simulated	4.54 dBi	6.69 dBi	-28.74 dB	-23.02 dB
Measured	0.27 dBi	2.55 dBi	-6.65 dB	-7.44 dB

From the far field pattern results it is again clear that there is good agreement between the simulated and measured results. It is also evident that the cross polarization has slightly increased when compared with ideal switching. This is likely due to the presence of the bias leads since they are unshielded in the vicinity of the DRA and likely distort the radiation pattern. Fortunately, it is apparent that the large cross polarization component in the H-plane has remained successfully reduced compared to the single shorting wall arrangement of Section 3.2. However, the target specification of -10 dB or better (x-pol maximum to co-pol maximum) was not maintained in the OOS configuration, as indicated in Table 17. Nonetheless, this can likely be improved on by more careful routing of the bias leads.

A comparison between the PIN diode switched and ideal switched dual-wall DRA from Section 3.3 is shown in Figure 98 and Figure 99 for both the OOO and OSO configuration respectively. It is clear that for the OOO configuration there are losses associated with the PIN diode case as the peak gain in both the E-plane and H-plane are reduced by 1.75 dB and 1.36 dB respectively as compared to the ideal case. The cross polarization level is also degraded in the PIN diode case, as is expected due to the presence of the bias leads. This happens even though the PIN diodes are switched off since there are induced currents in unshielded portions of the bias leads and the PIN diode has a large but finite resistance in the off state. Similarly, the PIN diode switched OSO configuration contains losses, as the peak gain in both the E-plane and H-plane are reduced by 1.64 dB and 3.73 dB respectively as compared to the ideal switching case. Again the cross polarization level is degraded. The losses in the OSO configuration are likely greater since the center PIN diode is switched on. However, when comparing the datasets it must be recalled that the antennas are slightly different (see Figure 77) and the measurements are taken at slightly different frequencies. Nonetheless it provides useful information.

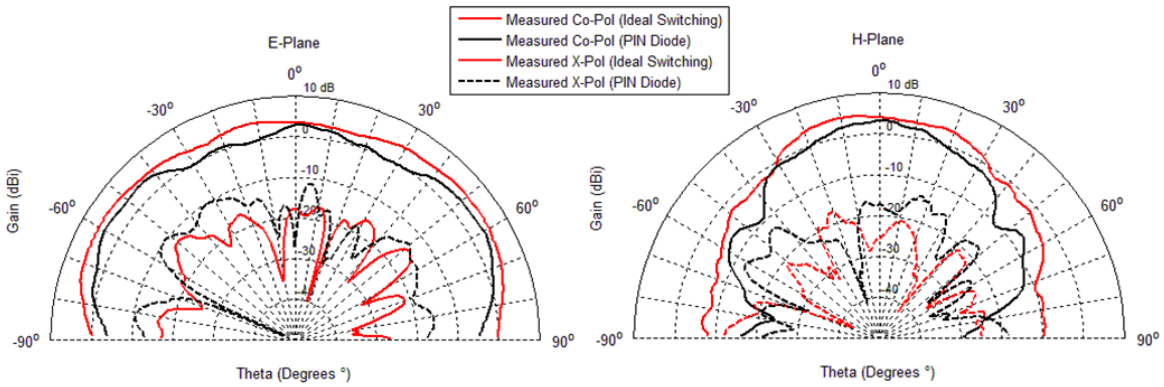

Figure 98: Radiation Pattern Comparison between PIN Diode and Ideal Switch for OOO Configuration (PIN Diode Switched - 4.8 GHz Ideal Switched - 4.65 GHz)

Table 18: Measured Gain and Cross Polarization Levels for PIN Diode Switched and Ideal Switched Dual-wall for OOO Configuration

	Peak Co-Pol Gain (H-Plane)	Peak Co-Pol Gain (E-Plane)	X-Pol – Co-Pol Level (H-Plane)	X-Pol – Co-Pol Level (E-Plane)
Ideal Switch	4.68 dBi	5.72 dBi	-16.92 dB	-18.14 dB
PIN Diode	3.32 dBi	3.97 dBi	-15.88 dB	-13.58 dB

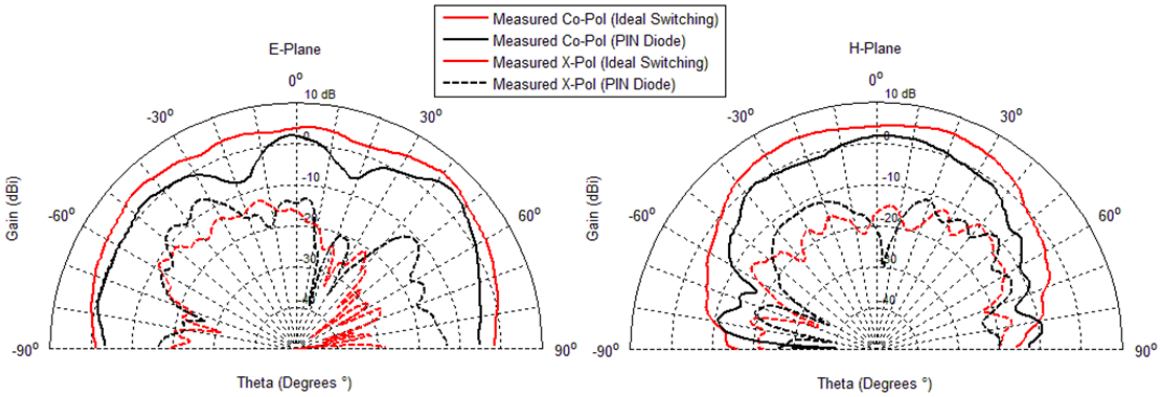

Figure 99: Radiation Pattern Comparison between PIN Diode and Ideal Switch for OSO Configuration (PIN Diode Switched - 5.7 GHz Ideal Switched – 6.1 GHz)

Table 19: Measured Gain and Cross Polarization Levels for PIN Diode Switched and Ideal Switched Dual-wall for OSO Configuration

	Peak Co-Pol Gain (H-Plane)	Peak Co-Pol Gain (E-Plane)	X-Pol – Co-Pol Level (H-Plane)	X-Pol – Co-Pol Level (E-Plane)
Ideal Switch	5.64 dBi	5.98 dBi	-16.25 dB	-16.79 dB
PIN Diode	1.91 dBi	4.34 dBi	-11.74 dB	-10.99 dB

As previously mentioned in Section 4.2, PIN diodes are current controlled devices and therefore the associated power consumption is something to consider. Since the PIN diodes require a forward bias voltage of 0.89 V in order to be switched on, the current drawn was carefully measured for each configuration. It was found that with a DC bias voltage of 900 mV the PIN diodes and associated bias network required 8 mA. Therefore, the SSS configuration requires 900 mV and approximately 24 mA which correspond to 21.6 mW (13 dBm) of power (worst case scenario in terms of power consumption). As shown in Figure 100 the PIN diodes series resistance in the on state is related to the forward current. Hence, the PIN diodes effective series resistance is estimated at 1.8 Ω. Since the series resistance of the PIN diode will adversely affect the antennas performance, one can vary the DC bias voltage and consequently the forward current in order to obtain an optimal tradeoff between the DC power consumption and antenna gain. Such an experiment was performed with the OSO configuration using board 1. As indicated in Figure 101, the OSO configuration's gain was measured in the E-plane at 4.8 GHz for different bias levels. Although the DC bias voltage was varied there was no change in

measured frequency response (no frequency shift and no change in input reflection coefficient). The results are summarized in Table 20 which demonstrate that a DC bias voltage of 900 mV is optimal since the minor improvement in gain when biased at 1100 mV is not justified given the substantial increase in power consumption. On the contrary, although the DC bias point of 700 mV has only a 1 dB reduction in peak gain while drawing negligible current, and thus power, there is little margin for error as any additional voltage drop could modify the antennas performance.

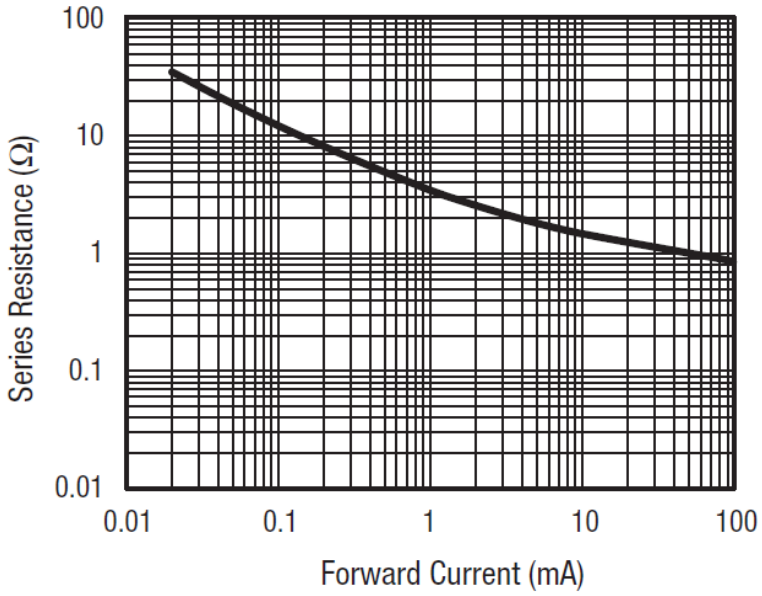

Figure 100: Series Resistance versus Forward Current for PIN Diode (Skyworks SMP1345) (After [2])

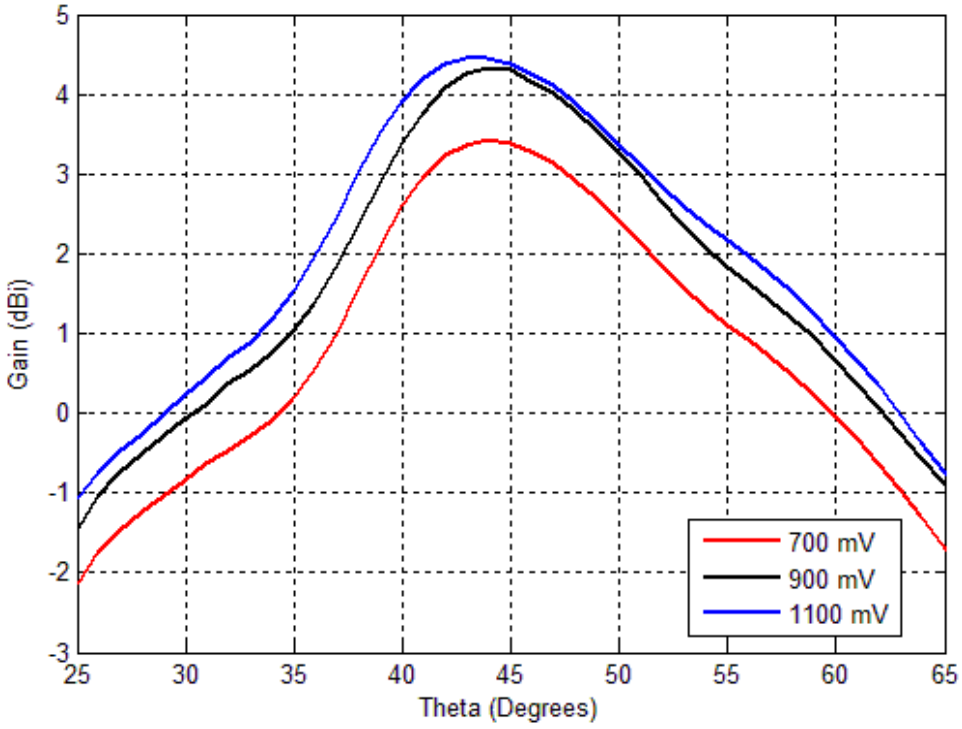

Figure 101: Measured E-Plane Gain Over an Angular Sector Containing the Direction of the Peak Gain at Various DC Bias Levels for PIN Diode Switched OSO Configuration at 4.8 GHz

Table 20: PIN Diode Switched OSO Configuration Bias Level and Associated Peak Gain

Bias Voltage (mV)	Current (mA)	Peak Gain (dBi)
700	~ 0	3.42
900	8	4.34
1100	43	4.46

4.5 Conclusion

In Chapter 3 the theoretical and experimental DRA used ideal switches (eg. soldering or desoldering the conducting tabs). In this chapter a novel method for achieving discrete frequency tuning with a dielectric resonator antenna has been presented using PIN diodes. Vertical gaps were introduced in the conducting walls to facilitate separate application of bias voltages to the individual switching diodes, and the conducting tabs geometry altered to accommodate the PIN diode package. These changes were incorporated into the field

simulation model. The selection process for obtaining an appropriate PIN diode was outlined along with device characterization. The procedure for extracting the PIN diode's characteristics was shown in order to obtain an equivalent circuit model that can be included in the electromagnetic simulation. The electronically switched reconfigurable DRA was also thoroughly described, including the DC bias network. The fabricated PIN diode switched antenna achieved a measured discrete tuning range of 95% and 97% for a return loss specification of 10 dB and 6 dB respectively with board one, and of 95% and 99% for a return loss specification of 10 dB and 6 dB respectively with board two. The lower operating band (~ 3 GHz) was shown to operate in the $TE^{x}_{\delta 01}$ mode and upper operating band (4-8.5 GHz) in the $TE^{x}_{\delta 11}$ mode. The antenna had sufficient gain, and the cross-polarization to co-polarization level was worse than -10 dB on only one measured switched state (OOS configuration on board 2). The antenna was also shown to have a return loss of 6 dB or better for 62% and 66% of the tuning range for board one and board two, respectively. The antennas DC power consumption was examined and was shown to consume a maximum of 13 dBm, which occurs when the SSS configuration is activated. The relationship between DC bias level and PIN diode series resistance was described with the optimal bias level of 900 mV selected due to the tradeoffs between antenna gain and DC power consumption. The frequency agile antenna which makes use of PIN diodes in order to achieve discrete tuning is believed to be the first full electronically switched implementation of a frequency agile DRA using diode switches.

4.6 References for Chapter 4

[1]*The Pin Diode Circuit Designers' Handbook*, Microsemi Corporation, Watertown, MA, 1998, pp. 1-18.

[2] Datasheet of SMP1345 PIN Diode, Skyworks, Application Note [Online], Available at (www.skyworksinc.com)

[3] Advanced Design System (ADS), Agilent Technologies, USA (www.agilent.com)

[4] Datasheet of 8038 SMA DC Block, Aeroflex, Application Note [Online], Available at (www.aeroflex.com)

[5] Datasheet of LMK212SD104KG-T Capacitor, Taiyo-Yuden, Application Note [Online], Available at (www.t-yuden.com)

[6] Datasheet of TCCH80+ RF Choke Inductor, Mini-Circuits, Application Note [Online], Available at (www.minicircuits.com)

Chapter 5 - Reconfigurable Dielectric Resonator Antennas - Varactor Diode Switching

5.1 Introductory Remarks

The dual-wall frequency reconfigurable antenna from Section 3.3 and the PIN diode switched reconfigurable antenna from Chapter 4 showed excellent performance. In this chapter the PIN diode switches are replaced with varactor diodes in order to achieve continuous tuning electronically. In Section 5.2 the selection process for the varactor diodes is outlined along with equivalent circuit models that represent the various varactor diode states. The antenna design is then presented in Section 5.3 followed by simulated and measured data showing the frequency response and radiation pattern in Section 5.4. In addition, the bias network design and DC power consumption are discussed. The format, and even portions of the text, in this chapter is purposefully similar to that for the PIN diode case in Chapter 4, in order to allow easier comparison of the results obtained using the two diode types.

5.2 Varactor Diode Selection and Characterization

In order to achieve continuous tuning using electronic switching, a varactor diode is the best option. The author selected to use varactor diodes for several reasons. Firstly, since varactor diodes are a mature technology they are inexpensive, have relatively low losses, are voltage controlled and are easy to model with lumped elements. As mentioned in Chapter 4, the ability to use low cost components is an essential requirement if such an antenna is to be used for mobile communication applications. Although the varactors incur larger losses than PIN diodes they enjoy the benefit of being voltage controlled devices which do not require current to operate, although they may require DC bias voltages of over 30 volts. Furthermore, the varactor diode's small physical size compared to wavelength and low package parasitic reactances, make it an ideal component for use in miniature, broadband RF signal control circuits. Since a varactor’s capacitance can take on a continuous range of values by varying a DC bias voltage, they make excellent tuning components. Once again the package size of the device was also a very important requirement since there was little flexibility in terms of device footprint as the switching device must have two ports and be no larger than 2 mm by 0.5 mm. Therefore, the varactors must use the SC-79 package, similar to that of the PIN diode from Chapter 4 shown in Figure 78.

Given the large number of varactor diodes available for use and the wide array of applications it was important to select the device that offered the best performance for the application at hand. In order to make use of a varactor's tuning ability while still having the ability to "open" the switches a varactor with a high capacitance ratio and low reverse voltage was selected. A varactor's capacitance ratio is simply c_{max}/c_{min} , thus having a large capacitance ratio results in a large capacitive tuning range. Therefore, a silicon hyperabrupt junction varactor diode was selected (Skyworks SMV2019 [1]). The varactor model was selected due to its high capacitance ratio (9.5) and low series resistance (4.8 Ω). The varactors capacitance versus reverse bias voltage is shown in Figure 102. It is clear that the varactor can tune from 2.22 pF to 0.235 pF, this corresponds to a self resonant frequency range of 4 GHz to 12.5 GHz, which will be shown below. The advantage in having the varactor operate with a capacitance of 0.235 pF is that the component behaves similar to an open switch in the band from 2 GHz to 8 GHz. Thus the varactor can be used similarly to the pin diode "open" state when biased to operate with a capacitance of 0.235 pF.

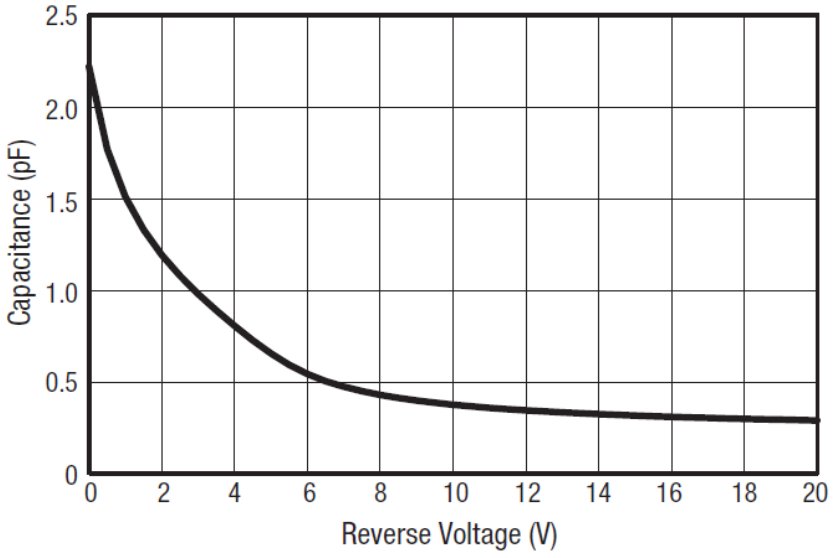

Figure 102: Capacitance versus Reverse Bias Voltage for Varactor Diode Model SMV2019 (After [1])

In order to accurately predict the performance of the antenna in simulation, the varactor's characteristics were extracted. To accomplish this, the non-linear SPICE model of the varactor diode [1] was obtained from the manufacturer along with the equivalent circuit for the package parasitics. An ideal switching configuration which contains the non-linear SPICE model of the varactor diode as well as the package parasitics is shown in Figure 103 in ADS format [2]. As is

evident in Figure 103, the model makes use of an ideal bias network since an ideal DC block and RF choke inductors are used. This configuration was simulated from 1 – 15 GHz and the S-parameters were obtained. Next, a simplified RLC equivalent circuit model for the varactor was adopted, as indicated in Figure 104. The varactor's equivalent circuit consists of a series parasitic inductance (L), an intrinsic capacitance (C) in parallel with an intrinsic resistance (R) as shown [1].

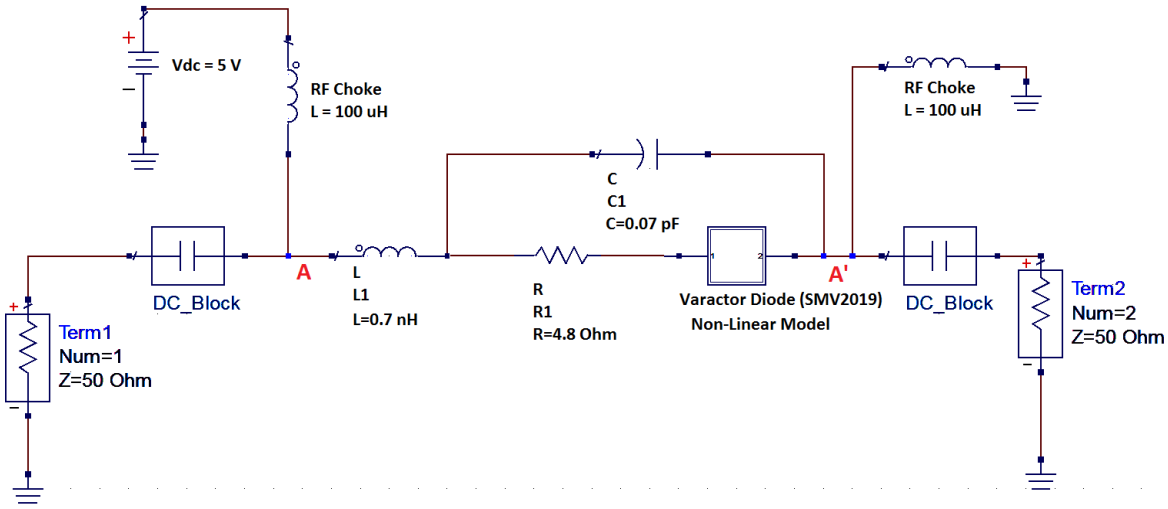

Figure 103: Non-Linear SPICE Model of Skyworks SMV2019 Varactor Diode with Ideal Bias Network

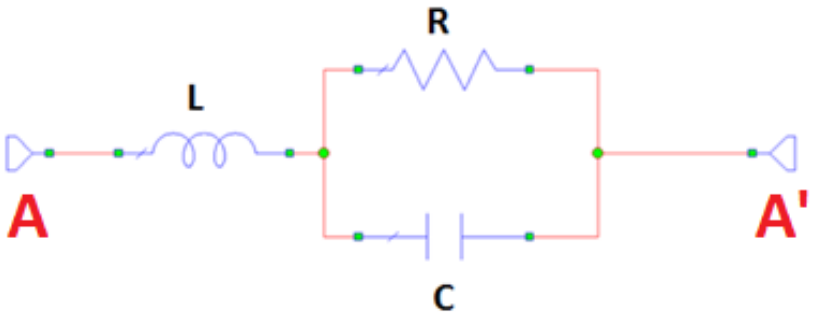

Figure 104: Varactor Diode Equivalent Circuit

Using the information from the manufacturer the parameter values for the equivalent circuit model were selected and then fine tuned in order to better agree with the SPICE model. The results of the parameter extraction are shown in Table 21. Figure 105 to Figure 107 show the simulated S-Parameters for both the SPICE model and the equivalent circuit model. From the S-

parameter results it is evident that the bias voltage of 19 V does not provide sufficient isolation at frequencies greater than 6 GHz since S11 is -4.1 dB and S12 only -2.8, ideally it would be at most -2 dB and -10 dB for S11 and S12 respectively. Nonetheless, it will represent an "open" condition up to 6 GHz, similar to a bad "PIN diode". As shown, there is good agreement between the SPICE model and the equivalent model. It is also clear that although the varactor is a suitable tuning device, the ideal varactor would be similar to an ideal band pass filter where only a brief frequency range is 'passed'. Therefore, the equivalent circuit models can be integrated into HFSS simulation in order to predict the performance of the antenna with varactors present.

Table 21: Parameter Values of Equivalent Circuit for Varactor

Reverse Bias Voltage	L (nH)	R (Ω)	C_T (pF)
0 V ("Short")	0.7	75	2.22
1 V	0.7	100	1.60
2 V	0.7	140	1.25
4 V	0.7	225	0.84
6 V	0.7	290	0.63
18 V	0.7	1200	0.245
19 V ("Open")	0.7	1400	0.235

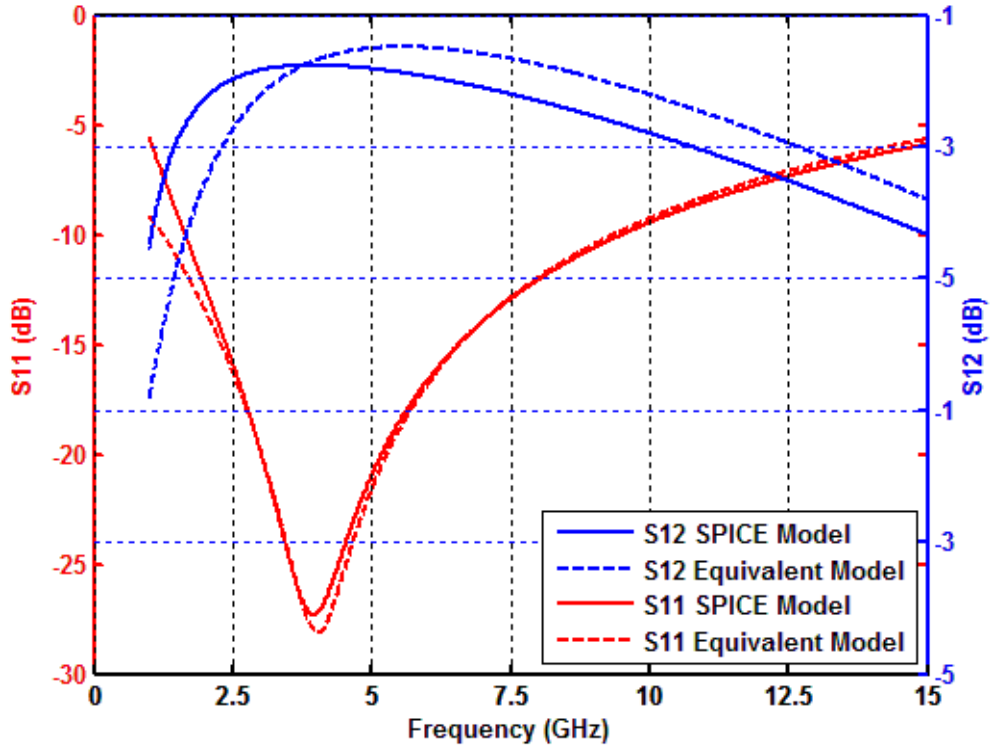

Figure 105: Simulated S-Parameters for the Varactor Diode (SMV2019) when Biased at 0 V

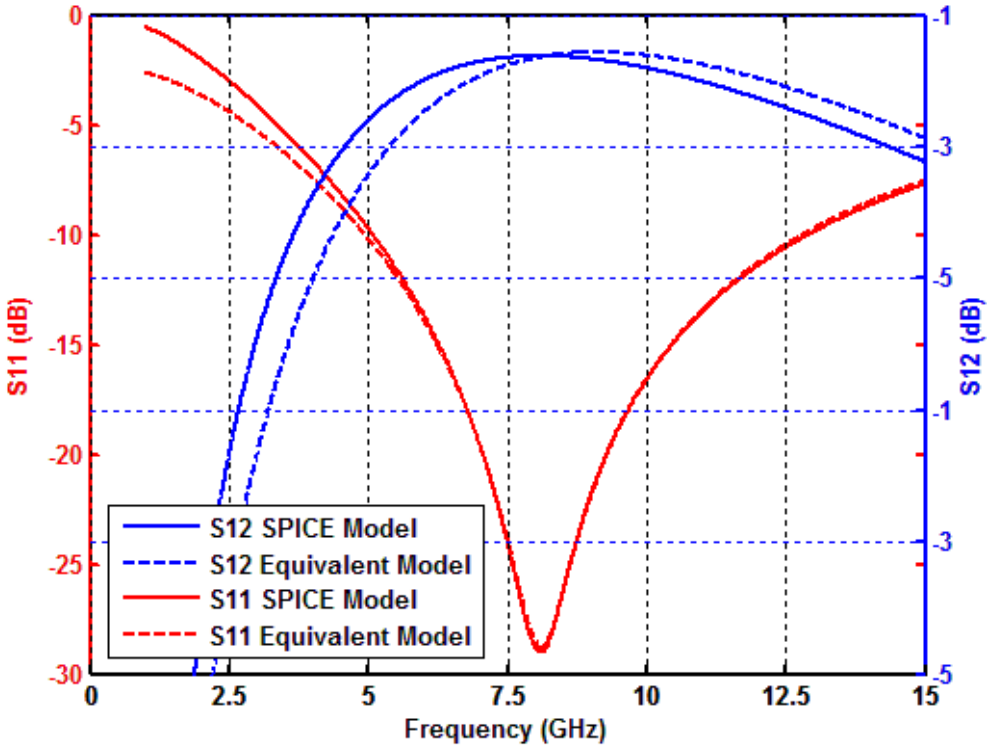

Figure 106: Simulated S-Parameters for the Varactor Diode (SMV2019) when Biased at 7 V

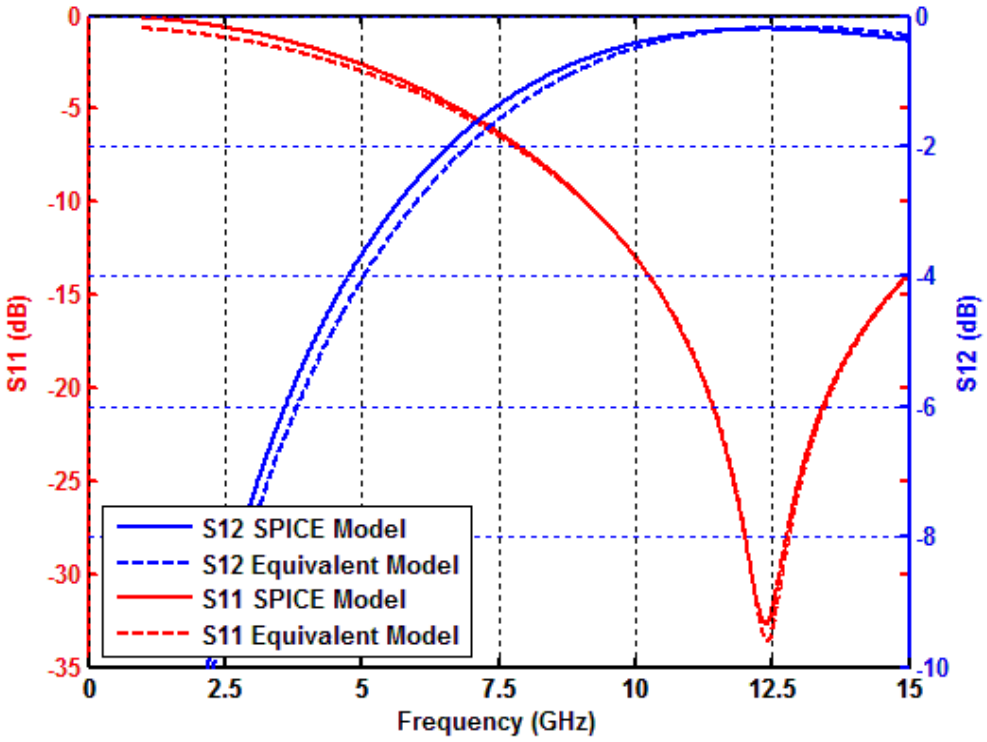

Figure 107: Simulated S-Parameters for the Varactor Diode (SMV2019) when Biased at 19 V

5.3 Dual-wall Frequency Agile DRA with Varactor Diode

Since an accurate equivalent circuit model of the varactor has been obtained that makes use of lumped elements, electromagnetic simulation can be performed using HFSS. The antenna, with the exception of the varactor diodes, is identical to that of Section 3.3.1, with most of the comments in Section 4.3 remaining relevant since the varactor diode has the same package (SC-79) as the PIN diodes used in that section. Again two boards are used, where board one is the configuration with the SMA DC blocking capacitor and board two makes use of the 254µm bias gap and surface mount DC blocking capacitor. Similar to the PIN diode case the antenna's DC bias leads were shielded using copper tape as this was demonstrated to improve performance.

5.4 Measured and Computed DRA Switching Performance

Since the varactors on either side of the DRA are switched as pairs there are still six fundamental antenna configurations for the on/off extremes of the varactor. However, each varactor can be controlled to values between its 2.22 pF (0 V) and 0.235 pF (19 V) extremes so there are effectively many more states. Once the antenna was fabricated the input reflection coefficient was measured and compared to simulation using HFSS modeling. The discrete tuning results are shown in Figure 108 to Figure 113 for both boards one and two, where "open" refers

to a bias voltage of 19 V and “short” to a bias voltage of 0 V. Results for intermediate voltage values will be shown later. The simulation results shown in the figures are always for board one. Simulation results were obtained for board two but were not included as they closely agree with those of board one, as HFSS does not predict the unwanted resonance at 3.4 GHz and 5.6 GHz, as mentioned in Section 4.3.

The agreement between the computed and measured values of the antenna is much similar to the PIN diode case shown in Chapter 4, as the measured results are shown to have a slight increase in frequency. This is again likely due to any number of the following reasons.

- Positioning of the DRA
- Air gaps between the ground plane and DRA
- Air gaps between the DRA and shorting wall substrate
- Soldered tab to ground plane connection
- Shorting wall positioning on the DRA
- The material manufacturers’ design tolerances
- Presence of DC bias leads
- Additional reactive loading of the varactor diode that is not accounted for in the model

In spite of this, the agreement between computation and measurement is satisfactory in the sense that the ability to continuously switch too many different operating bands is properly predicted, which also confirms that the equivalent circuit model for the varactor diodes is a good one. This further emphasizes the robustness of the design since the bias leads for the prototype antenna are far from optimal. It is clear that the unwanted resonance in board two had a large impact on the frequency response. The poor isolation at frequencies greater than 6 GHz for a reverse bias of 19 V (corresponding to the “open” case) is evident as all the configurations are similar over 6 GHz with the exception of the SSS case using board 1.

The continuous tuning ability is shown for board one in Figure 114 and for board two in Figure 115. It is apparent that the use of varactor diodes achieves continuous tuning from 3.1 GHz to 4.9 GHz for board one and from 3.1 GHz to 5.7 GHz for board two (10 dB return loss). It is also evident that the fabricated antenna achieved a tuning range of 95% and 96% for a return loss specification of 10 dB and 6 dB respectively with board one and of 59% and 64% for a return

loss specification of 10 dB and 6 dB respectively with board two. The continuous tuning range for board one was found to be 45% and 48% for a return loss specification of 10 dB and 6 dB respectively and of 59% and 64% for a return loss specification of 10 dB and 6 dB respectively for board two.

The reconfigurable antenna has several operating bands as shown in Figure 116. The data points in the figures represent frequencies where there is either a -10dB or -6 dB input reflection or better (as indicated above the diagram). In other words, Figure 116 displays the tuning range of the antenna along with all tuning operating bands that meet or exceed the specification of a 10 dB or 6 dB return loss. The operating band from 7.5 GHz to 8.5 GHz corresponds to the SSS configuration (18V 18V 18V) in board one only, as this corresponds to the $TE^{x}_{\delta 11}$ mode of operation whereas at all other configurations the resonance observed above 7 GHz is unwanted. It is clear that the dual-wall reconfigurable DRA with varactor diodes is capable of achieving continuous tuning while still maintaining a large tuning range.

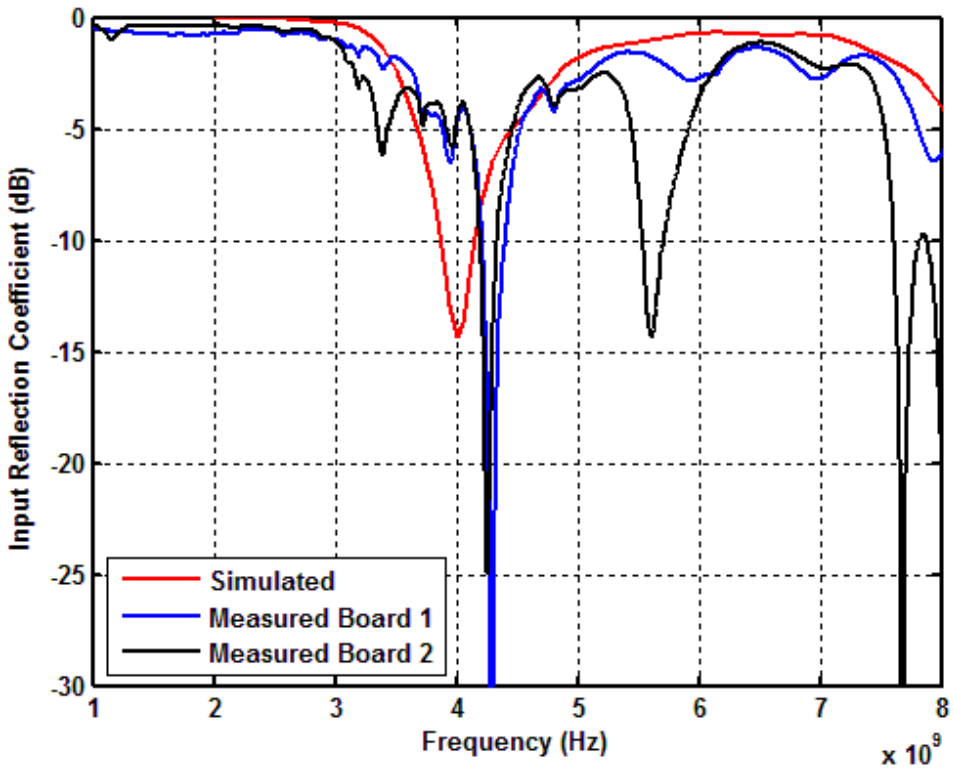

Figure 108: Frequency Response of Varactor Diode Switched Dual-wall Reconfigurable DRA for OOO Configuration

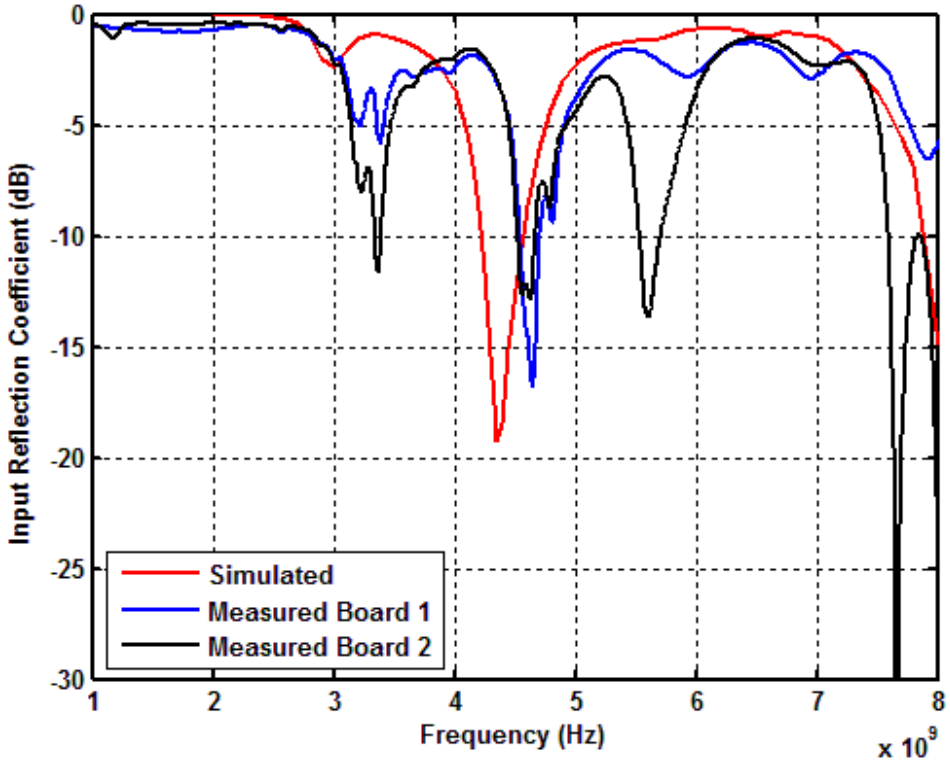

Figure 109: Frequency Response of Varactor Diode Switched Dual-wall Reconfigurable DRA for OOS Configuration

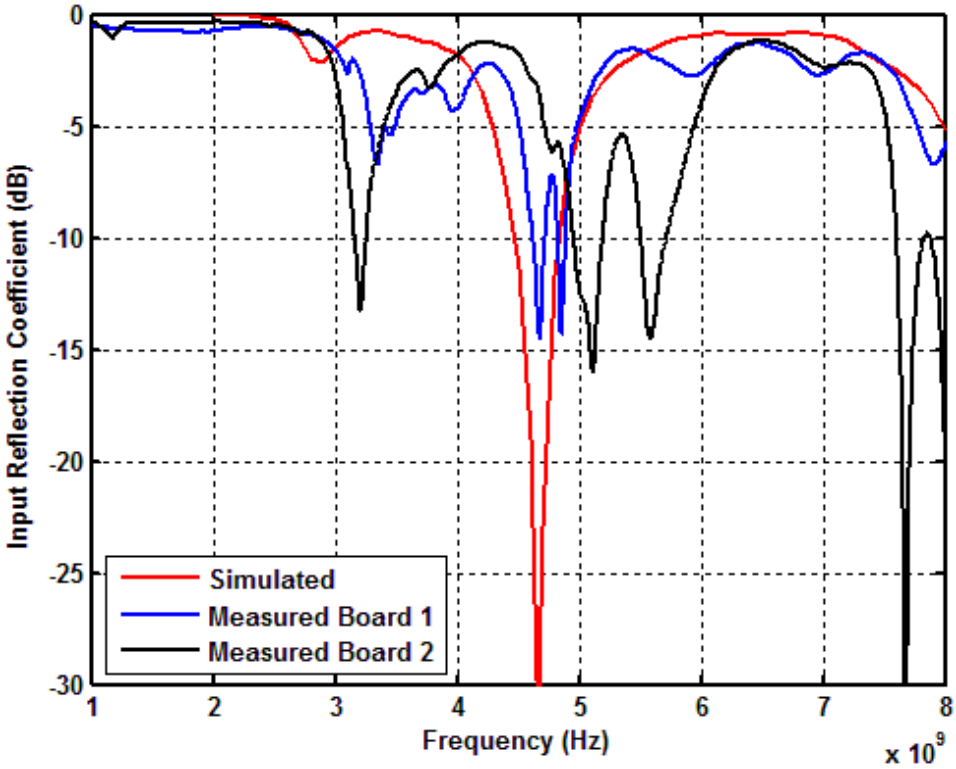

Figure 110: Frequency Response of Varactor Diode Switched Dual-wall Reconfigurable DRA for OSO Configuration

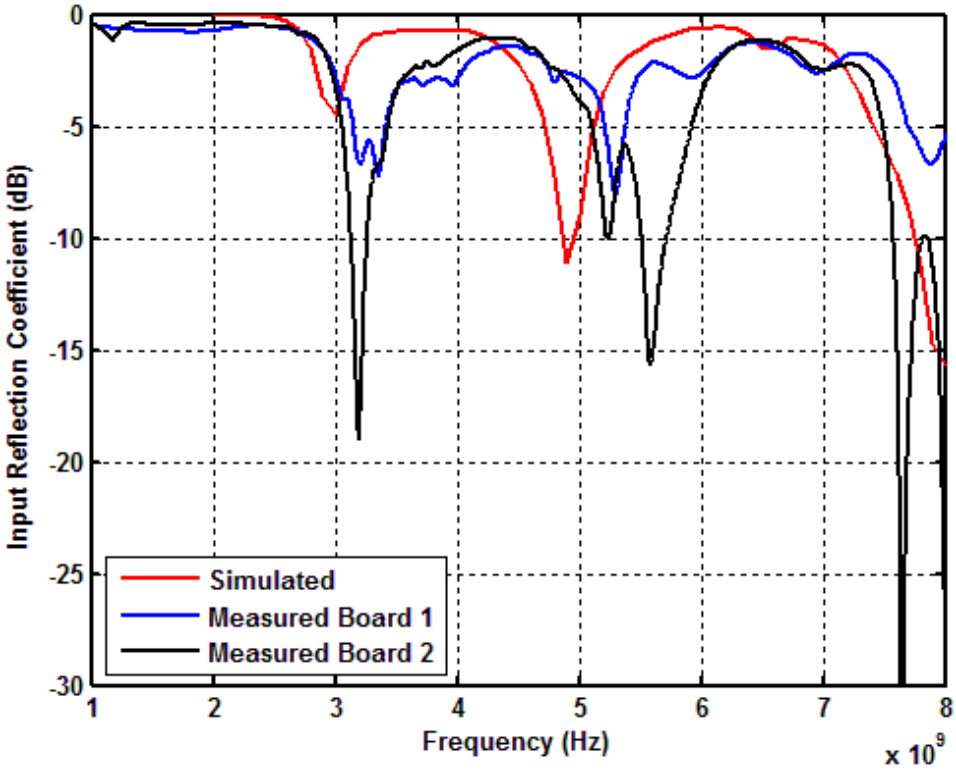

Figure 111: Frequency Response of Varactor Diode Switched Dual-wall Reconfigurable DRA for OSS Configuration

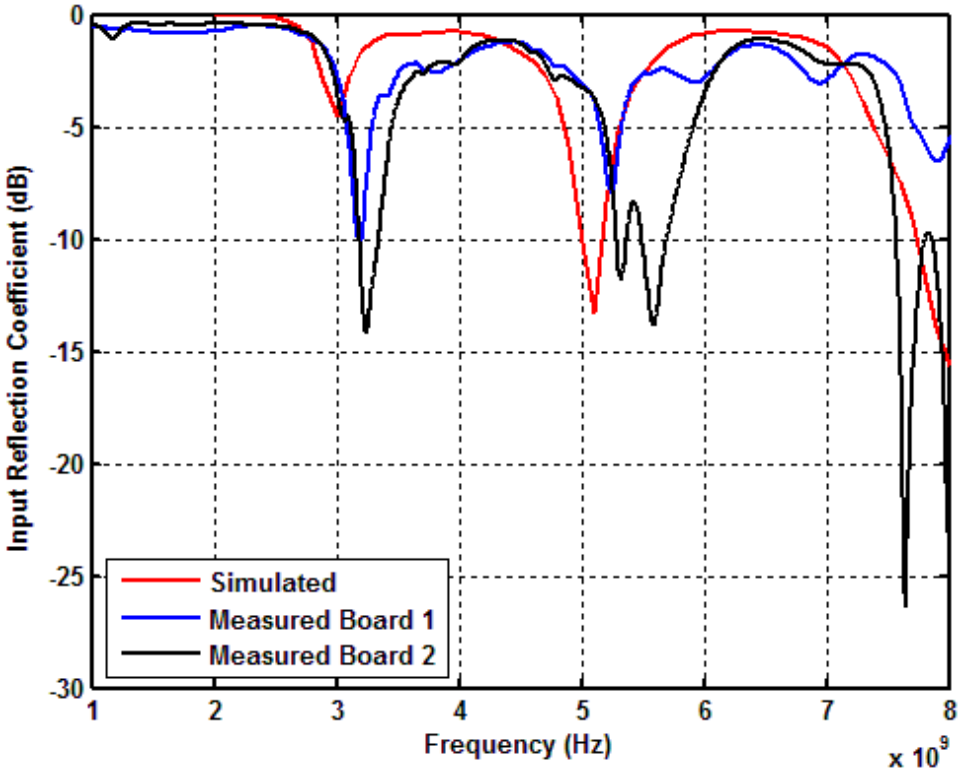

Figure 112: Frequency Response of Varactor Diode Switched Dual-wall Reconfigurable DRA for SOS Configuration

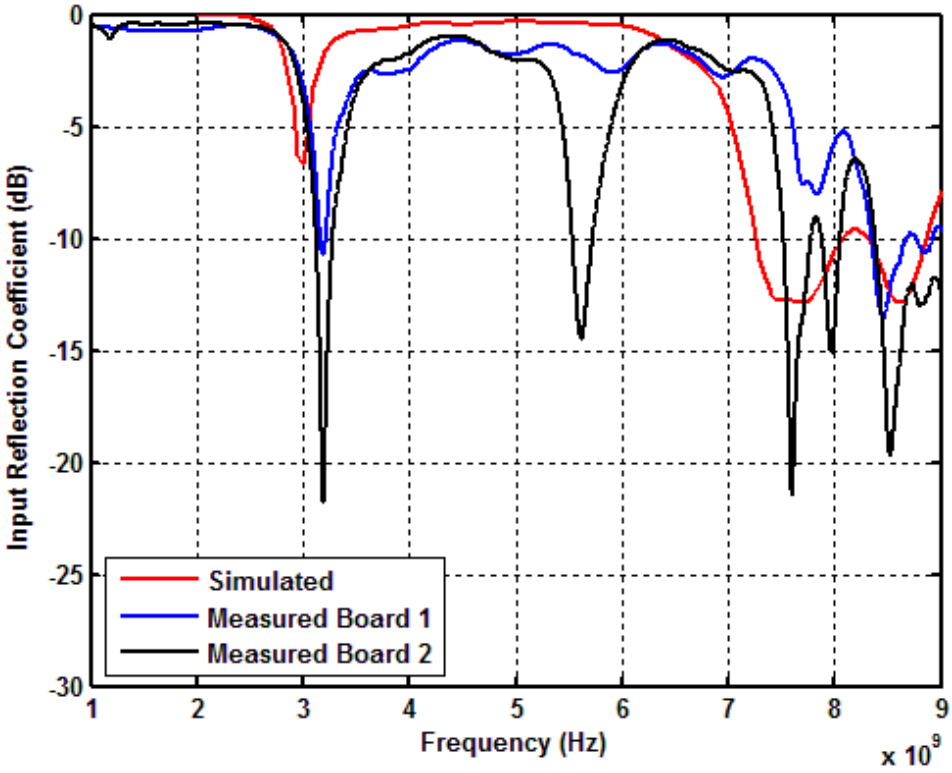

Figure 113: Frequency Response of Varactor Diode Switched Dual-wall Reconfigurable DRA for SSS Configuration

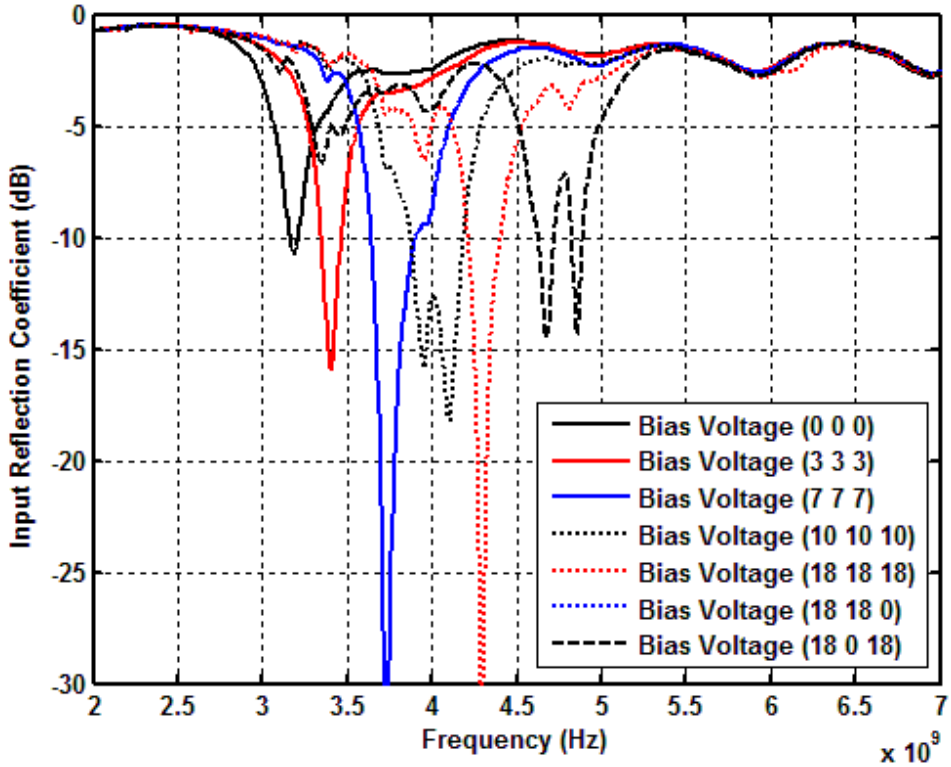

Figure 114: Frequency Response of Varactor Dual-wall DRA Showing Continuous Tuning for Board One

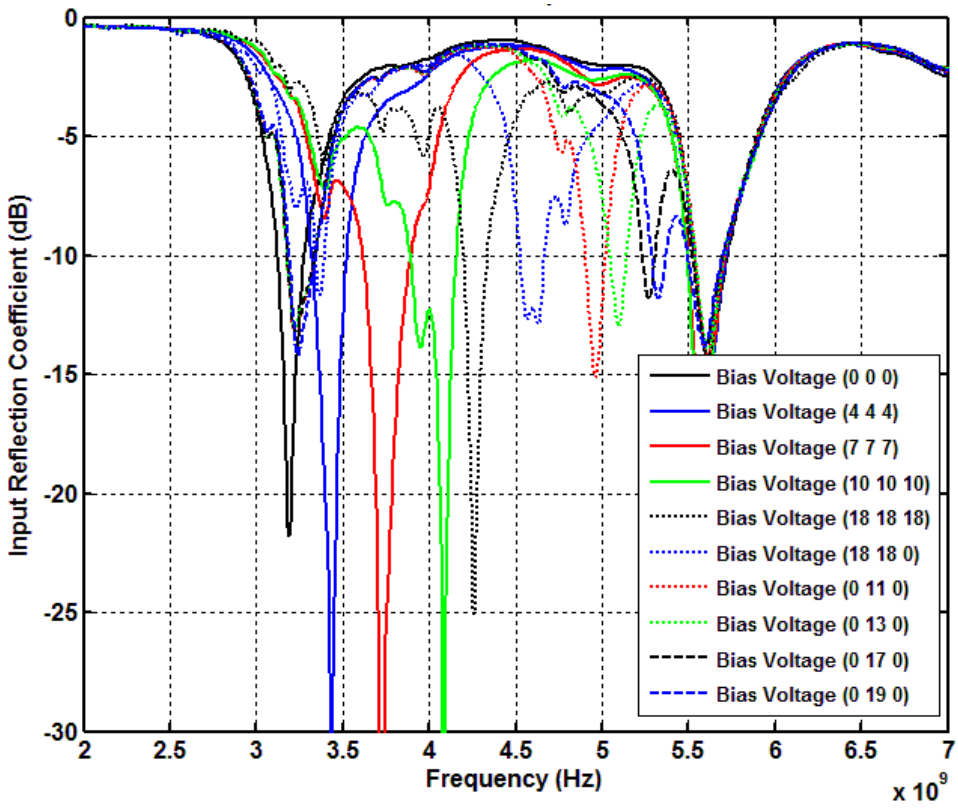

Figure 115: Frequency Response of Varactor Dual-wall DRA Showing Continuous Tuning for Board Two

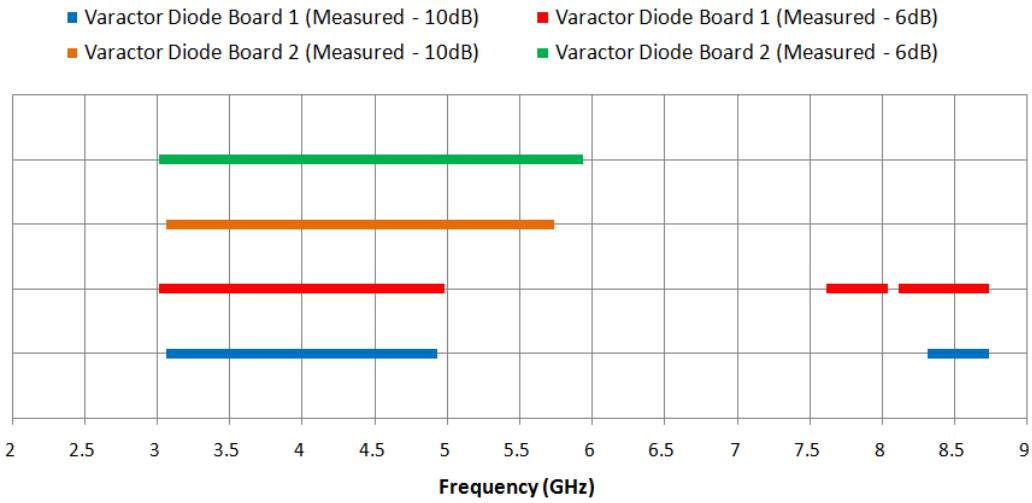

Figure 116: Tuning Range and Tuning Operating Bands that Satisfy a 10 dB and 6 dB Return Loss for Varactor Diode Switched Dual-wall Reconfigurable DRA

The radiation patterns of the various configurations were also computed using the HFSS model and measured. These are shown for four of the statesin Figure 117 to Figure 120. The

cases shown are highly representative of the results for all configurations and at all operating frequencies. A summary of the simulated and measured results is provided Table 22 to Table 25. This identifies the gain of each configuration as well as the cross-polarized to co-polarized level in both the E-plane and H-plane.

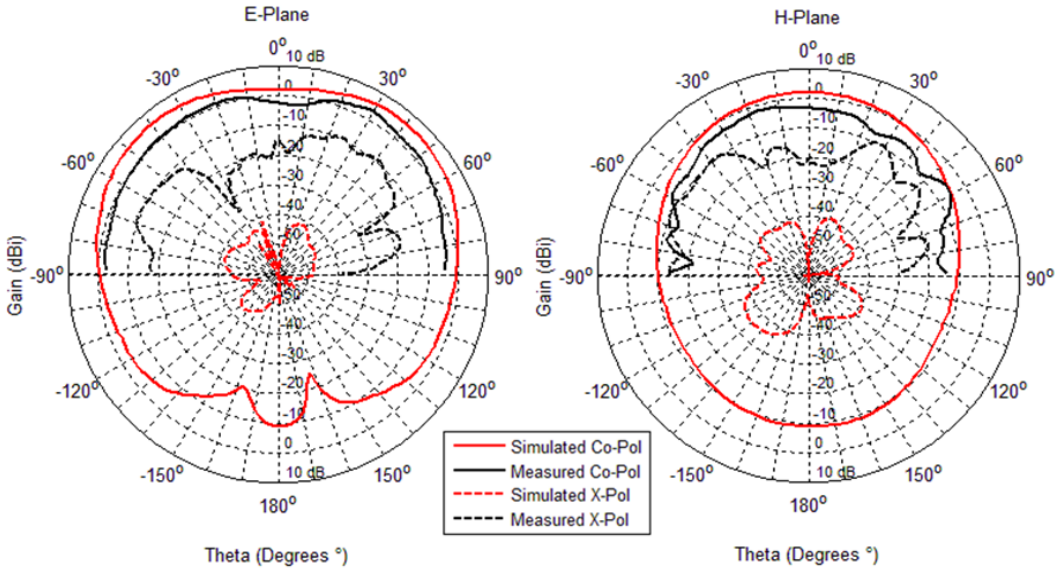

Figure 117: Measured and Simulated Gain for OOO Configuration of Varactor Diode Switched Dual-wall Reconfigurable DRA Operating at 4.2 GHz (Board 2)

Table 22: Measured and Simulated Gain and Cross Polarization Levels for Varactor Diode Switched Dual-wall OOO Configuration Operating at 4.2 GHz (Board 2)

	Peak Co-Pol Gain (H-Plane)	Peak Co-Pol Gain (E-Plane)	X-Pol – Co-Pol Level (H-Plane)	X-Pol – Co-Pol Level (E-Plane)
Simulated	2.11 dBi	6.21 dBi	-37.41 dB	-47.62 dB
Measured	-1.73 dBi	3.16 dBi	-7.68 dB	-12.33 dB

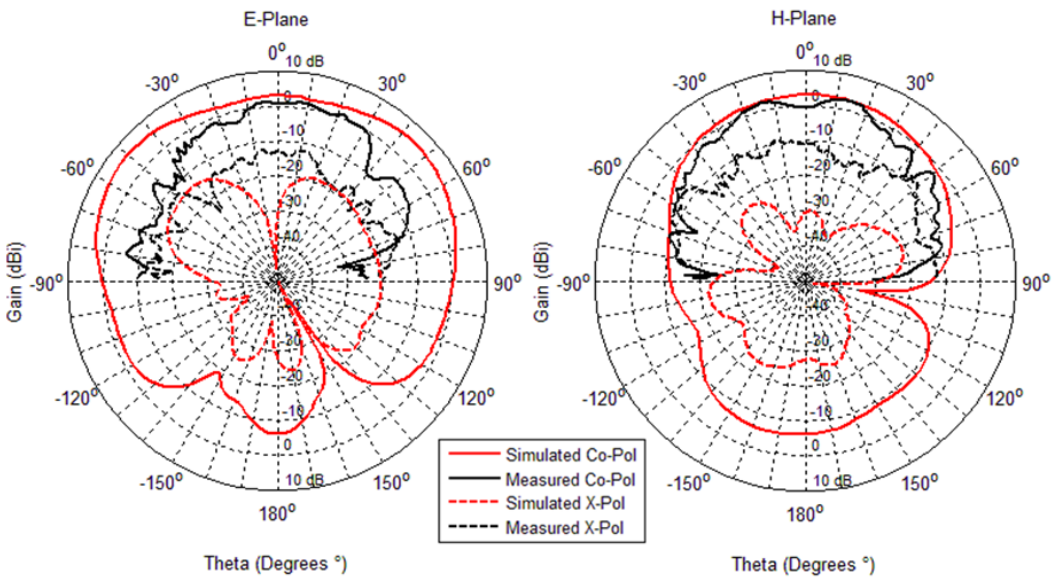

Figure 118: Measured and Simulated Gain for OOS Configuration of Varactor Diode Switched Dual-wall Reconfigurable DRA Operating at 4.7 GHz (Board 1)

Table 23: Measured and Simulated Gain and Cross Polarization Levels for Varactor Diode Switched Dual-wall OOS Configuration Operating at 4.7 GHz (Board 1)

	Peak Co-Pol Gain (H-Plane)	Peak Co-Pol Gain (E-Plane)	X-Pol – Co-Pol Level (H-Plane)	X-Pol – Co-Pol Level (E-Plane)
Simulated	3.13 dBi	6.03 dBi	-24.13 dB	-19.85 dB
Measured	2.72 dBi	1.47 dBi	-9.95 dB	-13.58 dB

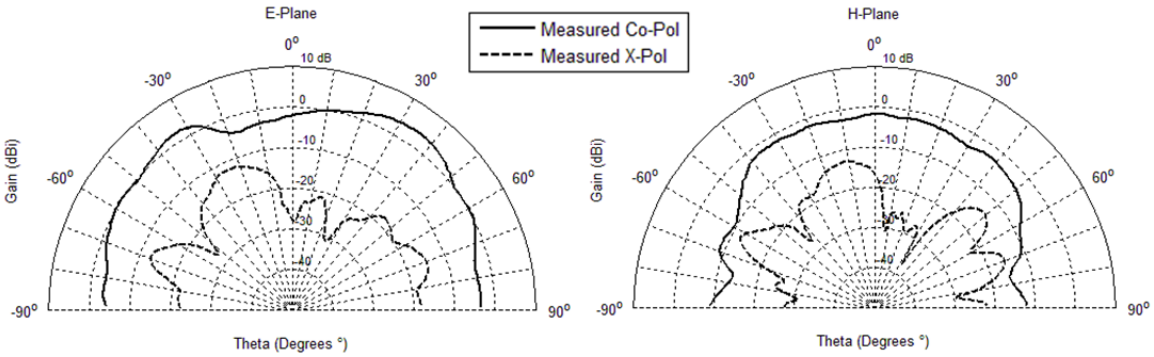

Figure 119: Measured Gain for Biasing of 7V 7V 7V for Varactor Diode Switched Dual-wall Reconfigurable DRA Operating at 3.7 GHz (Board 1)

Table 24: Measured Gain and Cross Polarization Levels for Varactor Diode Switched Dual-wall Biased at 7V 7V 7V Operating at 3.7 GHz (Board 1)

	Peak Co-Pol Gain (H-Plane)	Peak Co-Pol Gain (E-Plane)	X-Pol – Co-Pol Level (H-Plane)	X-Pol – Co-Pol Level (E-Plane)
Measured	-1.76 dBi	3.73 dBi	-10.76 dB	-15.64 dB

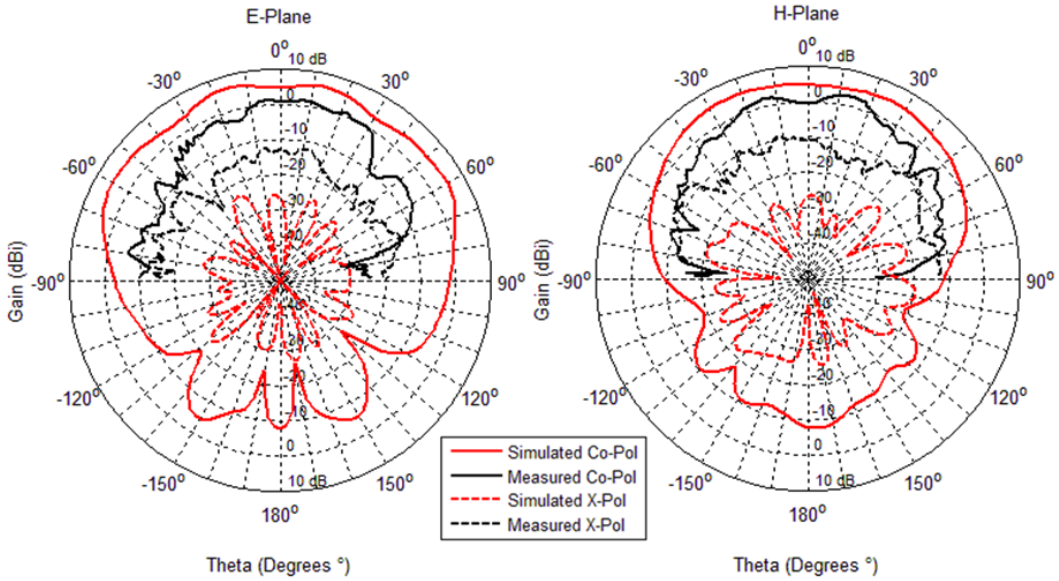

Figure 120: Measured and Simulated Gain for SSS Configuration of Varactor Diode Switched Dual-wall Reconfigurable DRA Operating at 7.8 GHz (Board 1)

Table 25: Measured and Simulated Gain and Cross Polarization Levels for Varactor Diode Switched Dual-wall SSS Configuration Operating at 7.8 GHz (Board 1)

	Peak Co-Pol Gain (H-Plane)	Peak Co-Pol Gain (E-Plane)	X-Pol – Co-Pol Level (H-Plane)	X-Pol – Co-Pol Level (E-Plane)
Simulated	5.65 dBi	6.45 dBi	-25.20 dB	-29.75 dB
Measured	2.72 dBi	1.47 dBi	-9.77 dB	-13.47 dB

From the far field pattern results it is again clear that there is relatively good agreement between the simulated and measured results. It is also evident that the cross polarization is similar to the PIN diode configuration since the levels have slightly increased when compared

with ideal switching. As for the PIN diode case this is due to the presence of the bias leads since they are unshielded in the vicinity of the DRA and likely distort the radiation pattern. Fortunately, it is apparent that the large cross polarization component in the H-plane has remained successfully reduced compared to the single shorting wall arrangement of Section 3.2. However, the target specification of -10 dB or better (x-pol maximum to co-pol maximum) was not maintained in all configurations, as indicated in the summary tables. Nonetheless, this can likely be improved on by more careful routing of the bias leads.

A comparison between the varactor diode switched and ideal switched dual-wall DRA from Section 3.3 is shown in Figure 121 and Figure 122 for both the OOO and SSS configuration respectively. It is clear that for the OOO configuration there are losses associated with the varactors case as the peak gain in both the E-plane and H-plane are reduced by 6.41 dB and 2.56 dB respectively as compared to the ideal case. The cross polarization level is also degraded in the varactor diode case, as is expected due to the presence of the bias leads. Similarly, the varactor loaded SSS configuration contains losses, as the peak gain in both the E-plane and H-plane are reduced by 4.80 dB and 2.94 dB respectively as compared to the ideal case. Again the cross polarization level is degraded. Comparing the results with those for the PIN diode case show that the varactor has a greater reduction in gain and a greater cross polarization component. The reduction in gain is due to the fact that the varactor diodes have larger losses associated with them then the PIN diodes while the cross polarization levels can be for any number of reasons (bias leads, routing method, fabrication, etc.). Again, when comparing the datasets it must be recalled that the antennas are slightly different (see Figure 77) and the measurements are taken at slightly different frequencies. Nonetheless it provides useful information.

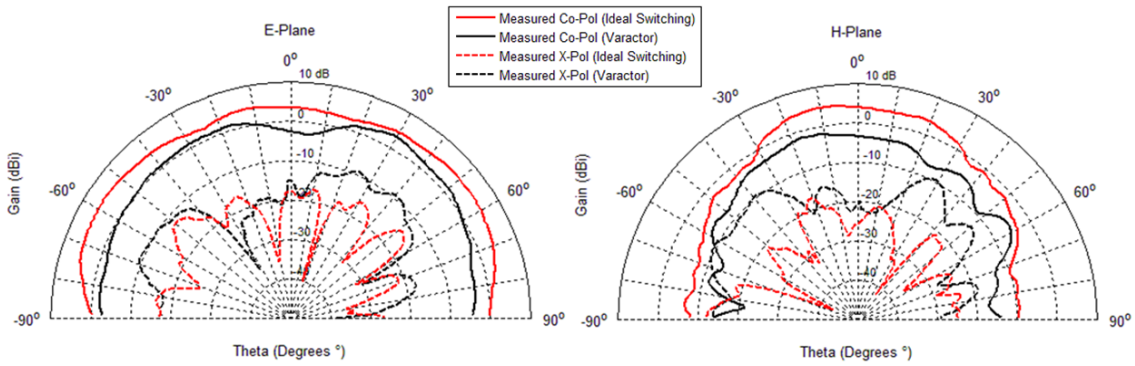

Figure 121: Radiation Pattern Comparison between Varactor Diode and Ideal Switch for OOO Configuration (Varactor Switched - 4.2 GHz Ideal Switched - 4.65 GHz)

Table 26: Measured Gain and Cross Polarization Levels for Varactor Switched and Ideal Switched Dual-wall for OOO Configuration

	Peak Co-Pol Gain (H-Plane)	Peak Co-Pol Gain (E-Plane)	X-Pol – Co-Pol Level (H-Plane)	X-Pol – Co-Pol Level (E-Plane)
Ideal Switch	4.68 dBi	5.72 dBi	-16.92 dB	-18.14 dB
Varactor	-1.73 dBi	3.16 dBi	-7.68 dB	-12.33 dB

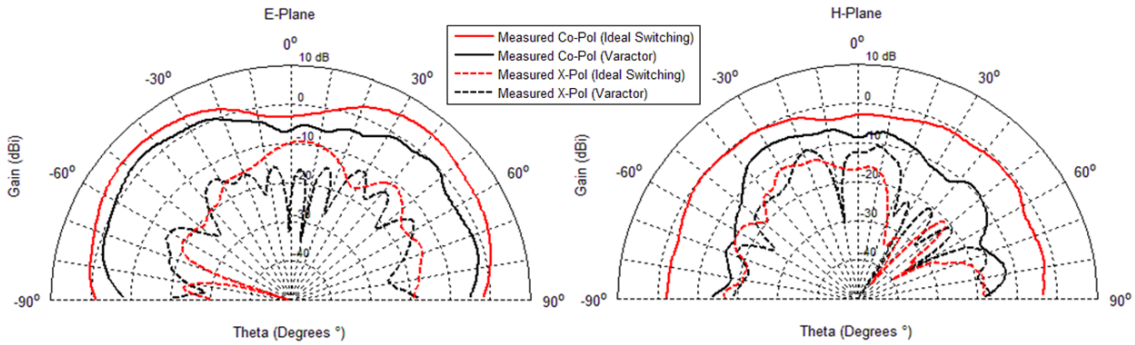

Figure 122: Radiation Pattern Comparison between Varactor and Ideal Switch for SSS Configuration (Varactor Switched - 3.1 GHz Ideal Switched – 3.1 GHz)

Table 27: Measured Gain and Cross Polarization Levels for Varactor Switched and Ideal Switched Dual-wall for SSS Configuration

	Peak Co-Pol Gain (H-Plane)	Peak Co-Pol Gain (E-Plane)	X-Pol – Co-Pol Level (H-Plane)	X-Pol – Co-Pol Level (E-Plane)
Ideal Switch	-0.10 dBi	5.20 dBi	-11.70 dB	-14.59 dB
Varactor	-4.90 dBi	2.26 dBi	-5.08 dB	-14.62 dB

As previously mentioned in Section 4.2, varactor diodes are voltage controlled devices and therefore they consume virtually no DC power. Nonetheless, the bias voltage must be obtained which will lead to some DC power consumption although the exact numbers depend on the biasing method. A photograph of the varactor switched frequency agile dielectric resonator antenna is shown in Figure 123.

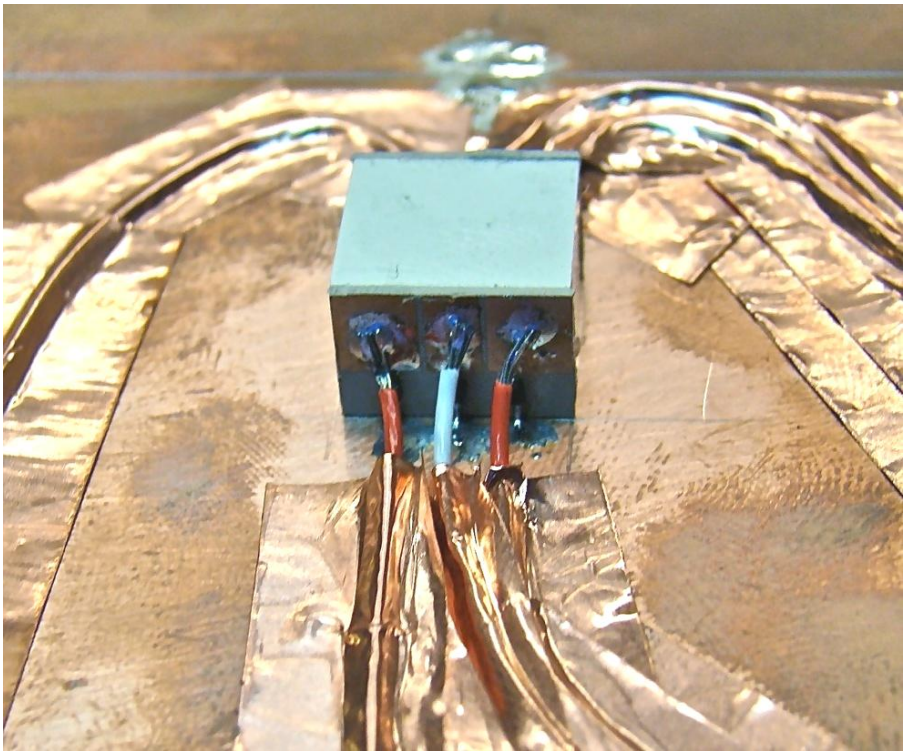

Figure 123: Photograph of Varactor Switched Frequency Reconfigurable DRA

5.5 Conclusion

A novel method for achieving continuous frequency tuning with a dielectric resonator antenna has been presented using varactor diodes. The selection process for obtaining the optimal varactor diode was outlined along with device characterization. The procedure for extracting the varactor diodes characteristics was shown in order to obtain an equivalent circuit model that is amendable to electromagnetic simulation. The fabricated varactor loaded antenna obtained a measured tuning range of 95% and 96% for a return loss specification of 10 dB and 6 dB respectively with board one and of 59% and 64% for a return loss specification of 10 dB and 6 dB respectively with board two. While the continuous tuning range for board one was found to be 45% and 48% for a return loss specification of 10 dB and 6 dB respectively and of 59% and 64% for a return loss specification of 10 dB and 6 dB respectively for board two. The antenna

had sufficient gain and the cross-polarization to co-polarization level was diminished as compared to the ideal switched case since the specification of -10 dB was not maintained under all bias levels. Since the varactors are voltage controlled devices the antenna's DC power consumption was shown to be negligible, which is an important aspect for mobile communications. This is the first frequency agile DRA with continuous tuning achieved using varactor diode switching.

5.6 References for Chapter 5

[1] Datasheet of SMV2019 Varactor Diode, Skyworks, Application Note [Online], Available at (www.skyworksinc.com)

[2] Advanced Design System (ADS), Agilent Technologies, USA (www.agilent.com)

Chapter 6 - General Conclusions

The principal contributions of this thesis are:

- *Development of a new dual-conducting-wall frequency reconfigurable dielectric resonator antenna structure.* The theoretical tuning range performance of the dual-wall reconfigurable DRA was examined for various aspect ratios and the performance of different switching configurations investigations. Using this information an optimum design was obtained in terms of tuning range and cross-polarisation reduction. Electromagnetic simulation and measured data (using ideal switches) showing the antenna input reflection coefficient over frequency, the particular radiating modes, and the radiation patterns, was presented. This confirmed the reasons for the cross-polarisation being reduced by the use of dual rather than single-walls. The antenna also had a wider tuning range than the single-wall structure.

- *The design and fabrication of a full electronic implementation of the dual-wall reconfigurable dielectric resonator antenna using PIN diodes.* This work included alterations to the conducting wall geometry to permit convenient independent switching of the three diodes on each conducting wall, and proper equivalent circuit modeling of the PIN diodes for inclusion in the electromagnetic simulation model. A discrete frequency tuning range of more than 95% was achieved. This is the first time that a frequency reconfigurable DRA has been fully implemented with actual integrated active switches.

- *The design and fabrication of a full electronic implementation of the dual-wall reconfigurable dielectric resonator antenna using varactor diodes.* This work included proper equivalent circuit modeling of the varactor diodes for inclusion in the electromagnetic simulation model. A discrete frequency tuning range of more than 95% was achieved while also providing a continuous tuning range of 59%. It is the first frequency reconfigurable DRA capable of continuous tuning using integrated active electronic devices.

There are two important issues whose investigation in the future would prove useful. Firstly, an integrated bias lead layout design that would lend itself to commercial fabrication would greatly encourage use of the frequency reconfigurable DRA in practice. Secondly, further

investigation of the reasons for the appearance of the unwanted resonances due to the gap in the groundplane (as observed for the second type of board layout described), that were measured but not predicted using the HFSS finite element field analysis, would be helpful. Precisely why do these resonances occur, how can they be overcome, and why does the field model not predict them as distinctly as they appear in the measurements?